UNIVERSITY OF CALIFORNIA
RIVERSIDE

Quantum State Protection and Transfer Using Superconducting Qubits

A Dissertation submitted in partial satisfaction
of the requirements for the degree of

Doctor of Philosophy

in

Physics

by

Kyle Michael Keane

September 2012

Dissertation Committee:

Dr. Alexander Korotkov, Chairperson
Dr. Leonid Pryadko
Dr. Vivek Aji

ProQuest LLC.
789 East Eisenhower Parkway
P.O. Box 1346
Ann Arbor, MI 48106 - 1346

The Dissertation of Kyle Michael Keane is approved:

Committee Chairperson

University of California, Riverside

Acknowledgments

With the utmost sincerity I wish to acknowledge that there have been countless people who have affected the course and direction of my life in a very profound way. It is my belief that each one has made this dissertation possible by shaping who I am and how I relate to the world around me. I would like to specifically acknowledge Dr. Alexander Korotkov and Dr. Murtadha Khakoo for there time and investment in my scientific career. I owe my deepest gratitude to these two men for teaching me that one can strive for perfection while remaining firmly committed to living in humble service.

To my parents, Mavi Keane and George Coffey, for allowing me the freedom to grow of my own accord and always being there when I needed them.

To my brother, Charles Keane, who has fearlessly illuminated my path through the numerous dark nights of my soul's journey.

To my dearest friend, Matt Birskovich, who saw me in a light that transformed how I saw myself.

To every person who believed in me, even when I did not believe in myself.

Finally, I would like to dedicate this accomplishment to all the people who have loved me and shared in life's passions.

ABSTRACT OF THE DISSERTATION

Quantum State Protection and Transfer Using Superconducting Qubits

by

Kyle Michael Keane

Doctor of Philosophy, Graduate Program in Physics
University of California, Riverside, September 2012
Dr. Alexander Korotkov, Chairperson

This dissertation presents a theoretical analysis of protocols relevant for quantum information processing with superconducting qubits. The purpose of these protocols is decoherence suppression and quantum information transfer. Our analysis makes use of the standard density matrix formalism and Kraus operator (operator-sum) representation of quantum operations. We also use the mathematical trick of unravelling continuous evolution into discrete scenarios with corresponding probabilities.

We show that decoherence due to zero-temperature energy relaxation can be almost completely suppressed, probabilistically, by weak measurement reversal (also known as quantum uncollapsing). To protect a qubit, a weak (partial) quantum measurement moves it towards the ground state, where it is kept during the storage period, while the second partial measurement restores the initial state. This procedure preferentially selects the cases without energy decay events. Stronger decoherence suppression requires smaller selection probability; a desired point in this trade-off can be chosen by varying the measurement strength.

We also analyze several simple quantum error correction (QEC) and quantum error detection (QED) protocols, relevant to superconducting qubits. We show that

for energy relaxation the repetitive N-qubit quantum codes cannot be used for QEC, but can be used for QED (also known as probabilistic error correction). Moreover, the repetitive code with only two qubits is sufficient for QED. We also present several other two-qubit algorithms realizable with the current technology of superconducting phase qubits; these algorithms can demonstrate QEC for intentional errors and QED for real decoherence.

We also analyze a procedure designed to transfer the state of a microwave qubit from one superconducting resonator to another resonator via a transmission line; the emission and capture of the microwave energy is achieved using tunable couplers. The procedure is shown to be robust against experimental imperfections of required pulse shapes. Our results also indicate that a successful state transfer requires nearly equal resonator frequencies for the entire duration of the procedure.

Contents

List of Figures

List of Tables

Chapter 1

Introduction

1.1 Overview and motivation

The focus of this dissertation is decoherence suppression and quantum state transfer for superconducting qubits [1] – Appendix A contains a list of my related publications and presentations which form the basis of Ch. 2, 3, 4, and 5 of this dissertation. Chapter 2 describes a novel application of uncollapsing [2] that can be used to probabilistically suppress decoherence due to zero-temperature energy relaxation – one of the two dominant sources of decoherence in superconducting qubits. In Ch. 3 we discuss the use of repetitive N-qubit quantum codes in the presence of energy relaxation. Chapter 4 presents several simple (and experimentally realizable) two-qubit decoherence suppression codes; one of the codes can be used to demonstrate quantum error correction (QEC) [3, 4, 5, 6, 7] for intentional errors and the other codes can be used for the suppression of real decoherence by quantum error detection (QED). In Ch. 5 we investigate the robustness of a recently proposed quantum state transfer procedure [8].

Let us begin by discussing the standard methods for suppressing qubit decoherence. For a generic qubit state, it is well established that decoherence can be

efficiently suppressed via QEC by encoding the state of a single qubit into several physical qubits and performing sufficiently frequent measurement/correction operations [7] (Appendix B contains a brief review of the standard bit-flip code). Another decoherence suppression technique which also requires the use of a larger Hilbert space is the idea of decoherence-free subspaces [9], where a logical qubit is encoded in such a way that it becomes insensitive to decoherence (without the measurement and correction required for QEC). Without increasing the physical Hilbert space, it is possible to suppress decoherence using the technique of dynamical decoupling based on sequences of control pulses, for example, by "bang-bang" control [10]. Unfortunately, dynamical decoupling does not help [10, 11] when the decoherence is due to processes with short correlation timescales, as for example the most standard (Markovian) energy relaxation and dephasing. Energy relaxation and other (Markovian) decoherence can in principle be suppressed by changing some properties of the qubit environment, as is commonly done for the suppression of spontaneous emission in cavities [12]; however, this possibility does not seem very practical for solid-state qubits.

The decoherence suppression procedure presented in Ch. 2 (which we first proposed in Ref. [13]) does not require a larger Hilbert space, it protects against (Markovian) energy relaxation, and it is a simple modification of existing uncollapsing experiments with superconducting phase qubits [14] and photonic polarization qubits [15]. In the existing experiments [14, 15], the effect of a weak measurement (of known strength) is undone using a second weak measurement of the same strength, returning an unknown qubit state to its original superposition and probabilistically reversing the non-unitary evolution due to the first measurement. In Ch. 2 it is shown that a qubit subject to zero-temperature energy relaxation during the time between the first and second (now stronger) measurement can be preserved to an arbitrary degree. Our original proposal

[13] was subsequently demonstrated using a photonic polarization qubit in Ref. [16]. A second experiment, also using photonic polarization qubits, was performed in Ref. [17]; this second experiment demonstrated that when our decoherence suppression procedure is independently applied to two initially-entangled qubits, the original entanglement can be restored even when both qubits are subject to zero-temperature energy relaxation.

Although our decoherence suppression procedure and the subsequent experiments generated some general interest [18], QEC is still the most commonly studied method for protecting a qubit state from decoherence of an arbitrary type. Experimental progress is still being made toward a full implementation of QEC in many physical systems. Measurement-free QEC experiments in nuclear magnetic resonance (NMR) systems [19, 20, 21, 22] have been performed for over a decade, but only with ensembles of quantum systems [23]. Using trapped ions, a three-qubit QEC experiment with actual measurement was realized [24], and recently a measurement-free QEC procedure with several error correction cycles was demonstrated [25]. In linear optics systems, the QEC experiments include two-qubit protection against "accidental" measurement [26], a continuous-variable adaptation of the 9-qubit Shor code [27], a continuous-variable erasure-correcting code [28], and eight-photon topological error correction [29]. A three-qubit measurement-free QEC protocol has been recently demonstrated with superconducting "transmon" qubits [30].

With the rapid progress in experiments with superconducting qubits [1, 31, 32, 33, 34, 35], QEC with actual measurements is becoming feasible in these systems in the reasonably near future. Our goal in Ref. [36] (the results of which have been divided into Chs. 3 and 4 of this dissertation) was to find possible measurement-based protocols for these systems. In Ch. 3 we describe the use of repetitive quantum codes for decoherence suppression by quantum error detection (QED) of energy relaxation – it is shown that

two qubits are sufficient for this purpose. Chapter 4 contains several two-qubit QED and QEC procedures that can be readily realized with the current level of phase qubit technology.

Also becoming feasible in these systems is a quantum information transfer procedure in the form of a so-called "flying microwave qubit". In Ch. 5 we investigate the feasibility of a flying microwave qubit procedure that was recently proposed in Ref. [8]; for this purpose, we analyze the procedure's robustness against typical experimental errors. In the original proposal the state of a qubit is transferred using tunable couplers from one microwave resonator (or phase qubit) through a transmission line to another resonator (or phase qubit). Our results indicate that this procedure is robust, but requires nearly equal resonator frequencies during the entire transfer procedure. The results of Ch. 5 were presented at a conference of the American Physical Society [37].

The remaining sections of Ch. 1 will establish the core concepts and techniques used in this dissertation. The basics of qubit physics are presented in Sec. 1.2, including state representation and quantum operations for two-level systems. Section 1.3 introduces the topic of state-independent characterization for quantum processes. Section 1.4 contains the formal analysis of a single qubit subject to zero-temperature energy relaxation; this section introduces two important techniques that are used throughout this dissertation: the mathematical trick of "unravelling" energy relaxation into discrete scenarios and the method for calculating the various process characterization measures from Sec. 1.3 (for both linear and non-linear quantum operations). Section 1.5 contains a brief introduction to the phase qubit technology. The chapter ends with Sec. 1.6 which describes the current procedure for measuring a phase qubit (in both the projective and weak cases); this section also contains the explicit procedure for reversing a weak measurement of known strength in this system.

1.2 Two-level quantum states (qubit physics)

In quantum mechanics the state of a system is described by either a wavefunction (pure states only) or by a density matrix (general state). The wavefunction of an arbitrary (pure) two-level quantum system (qubit) can be represented as a superposition of two basis states, in the so-called "computational" basis each level corresponds to one basis state. In the language of quantum computing the basis states of a qubit are often labeled "0" and "1" in analogy with a classical bit of information in computer science. In the standard bra-ket notation, the wavefunction (usually denoted as $|\psi\rangle$) can then be written in the computational basis as

$$|\psi\rangle = \alpha|0\rangle + \beta|1\rangle, \tag{1.1}$$

where α and β are complex-valued coefficients subject to the normalization condition $|\alpha|^2 + |\beta|^2 = 1$, and the kets $|0\rangle$ and $|1\rangle$ represent the computational basis states.

The wavefunction of an arbitrary (pure) two-level system can also be represented (in the computational basis) by the column vector

$$\alpha|0\rangle + \beta|1\rangle = \begin{pmatrix} \alpha \\ \\ \beta \end{pmatrix}. \tag{1.2}$$

In this column-vector representation unitary state-transformations are expressed using the standard Pauli matrices [1] as

$$\mathrm{R}_j(2\theta) = e^{-\imath\theta\sigma_j}, \tag{1.3}$$

where σ_j is the jth Pauli matrix. The right-hand side of Eq. (1.3) represents a unitary state-transformation in the column-vector representation with parameter θ and generator σ_j. The left-hand side of Eq. (1.3) can be interpreted as a rotation of the so-called

[1] $\sigma_x = \begin{pmatrix} 0 & 1 \\ 1 & 0 \end{pmatrix}$, $\sigma_y = \begin{pmatrix} 0 & -\imath \\ \imath & 0 \end{pmatrix}$, $\sigma_z = \begin{pmatrix} 1 & 0 \\ 0 & -1 \end{pmatrix}$

Bloch vector in 3-dimensional space with corresponding angle 2θ around the j-axis [7] (see Appendix C for more details on this interpretation). Often in this dissertation pure qubit states will be represented by wavefunctions, while quantum operations will be represented using matrices and described by the corresponding rotations in three-dimensional space.

The density matrix (usually denoted by ρ) of the pure state in Eq. (1.1) is given by the outer product $|\psi\rangle\langle\psi|$. Using the column-vector representation the density matrix (in the computational basis) can be written as

$$\rho = |\alpha|^2 |0\rangle\langle 0| + \alpha\beta^* |0\rangle\langle 1| + \alpha^*\beta |1\rangle\langle 0| + |\beta|^2 |1\rangle\langle 1| = \begin{pmatrix} |\alpha|^2 & \alpha\beta^* \\ \alpha^*\beta & |\beta|^2 \end{pmatrix}, \tag{1.4}$$

where the normalization condition is now expressed as $\mathrm{Tr}[\rho] = 1$. Notice that $\mathrm{Tr}[\rho^2] = 1$, this is because ρ represents a pure state (for a mixed state $\mathrm{Tr}[\rho^2] < \mathrm{Tr}[\rho]$).

Next we discuss the state representation of multiple independent qubits. The wavefunction of a multiple independent-qubit system can be expressed as the tensor product of the individual qubit wavefunctions. In the case of two qubits (labeled a and b) this means $|\psi^{ab}\rangle = |\psi^a\rangle \otimes |\psi^b\rangle$, where $|\psi^{ab}\rangle$, $|\psi^a\rangle$, and $|\psi^b\rangle$ are the wavefunctions of the combined system, qubit a, and qubit b respectively. The individual qubit wavefunctions can be represented in the computational basis as $|\psi^i\rangle = \alpha_i|0\rangle + \beta_i|1\rangle$, where $i = a, b$. The combined-system wavefunction is then

$$|\psi^{ab}\rangle = \alpha_a\alpha_b|00\rangle + \alpha_a\beta_b|01\rangle + \beta_a\alpha_b|10\rangle + \beta_a\beta_b|11\rangle. \tag{1.5}$$

The four new joint states $|00\rangle$, $|01\rangle$, $|10\rangle$, and $|11\rangle$ are called the computational basis of the two qubit Hilbert space. When the joint state $|\psi^{ab}\rangle$ cannot be decomposed into the tensor product of two individual qubit states, the qubits are said to be entangled. The relationship of separability and entanglement extends to systems of more than two

qubits in a similar manner.

1.3 Characterization of quantum processes

In general, a quantum procedure is defined as the transformation of all possible initial states to their corresponding final states after the procedure is finished, this means one must know the evolution of an infinite number of quantum states. We can describe such a transformation using the following mathematical expression

$$\rho_{\text{fin}} = \varepsilon(\rho_{\text{in}}), \tag{1.6}$$

where ρ_{in} and ρ_{fin} represent the initial and corresponding final quantum states of a system subject to the quantum operation described by the superoperator ε. If a quantum operation is linear, then it is sufficient to know the evolution of a smaller set of quantum states. For instance, if we use Eq. (1.4) to define the arbitrary pure initial state of a single qubit as

$$\rho_{\text{in}} = |\alpha|^2 |0\rangle\langle 0| + \alpha\beta^* |0\rangle\langle 1| + \alpha^*\beta |1\rangle\langle 0| + |\beta|^2 |1\rangle\langle 1|, \tag{1.7}$$

then a linear quantum operation can be represented as

$$\varepsilon(\rho_{\text{in}}) = |\alpha|^2 \varepsilon(|0\rangle\langle 0|) + \alpha\beta^* \varepsilon((|0\rangle\langle 1|) + \alpha^*\beta \varepsilon(|1\rangle\langle 0|) + |\beta|^2 \varepsilon(|1\rangle\langle 1|). \tag{1.8}$$

Thus the evolution of only four initial states fully defines a linear single-qubit quantum operation.

To facilitate the comparison of different quantum operations, it is desirable to describe a procedure independent of the initial and final states of the system. For few-qubit systems this is usually done using quantum process tomography (QPT) [7], where a given procedure is defined by a matrix (usually referred to as the χ-matrix) in a

chosen, fixed operator basis. [In principle QPT is applicable to systems with an arbitrary number of qubits, but in practice the resources required to describe a process involving more than a few qubits quickly become unmanageable.] The method of QPT is only applicable to linear quantum operations and cannot be rigorously defined for non-linear operations. Since most quantum operations are linear, this requirement is not usually important; however, many procedures discussed in this dissertation require the selection of only certain special cases (which is a non-linear operation). We will discuss this subtlety after reviewing the technique of QPT. All procedures in this dissertation are designed to preserve an unknown single-qubit state, we therefore only need a description of the actual evolution of our system in order to compare it to the ideal memory operation (identity mapping of an arbitrary density matrix into itself). After introducing the usual definition of the χ-matrix, we introduce the different measures used in this dissertation for comparing the similarity of the two different procedures: ideal memory operation and the actual evolution.

In the usual definition of the χ-matrix for a single-qubit operation, the transformation defined in Eq. (1.6) is equivalently expressed using the so-called "operator-sum representation" as [7]

$$\varepsilon(\rho_{\text{in}}) = \sum_{j=1}^{N} K_j \rho_{\text{in}} K_j^{\dagger}, \tag{1.9}$$

where K_j are often called the "operator elements" of the quantum operation ε; for a trace-preserving operation $\sum_{m=1}^{N} K_m^{\dagger} K_m = \mathbb{1}$, where $\mathbb{1}$ is the identity matrix of appropriate dimension. These operator elements can be expressed in terms of a complete, orthonormal operator basis as $K_j = \sum_{m=1}^{4} c_{j,m} E_m$, where the matrices E_m are the elements of the chosen basis; Eq. (1.9) can then be written as

$$\varepsilon(\rho_{\text{in}}) = \sum_{m,n=1}^{4} \chi_{m,n} E_m \rho_{\text{in}} E_n^{\dagger}, \tag{1.10}$$

where $\chi_{m,n} = \sum_{j=1}^{N} c_{j,m} c_{j,n}^{*}$ are the (complex) elements of the so-called χ-matrix (sometimes referred to as the "process matrix").

To characterize the similarity of two quantum procedures either the quantum process tomography (QPT) fidelity F_{χ} or the average state fidelity $F_{\rm av}$ can be used. The QPT fidelity is usually defined as [7, 38] $F_{\chi} = {\rm Tr}(\chi_{\rm desired}\chi)$, where χ is the actual process matrix and $\chi_{\rm desired}$ in our case corresponds to the ideal quantum memory operation, i.e. no evolution of the qubit. The average state fidelity is [7, 38] $F_{\rm av} = \int {\rm Tr}(\rho_{\rm fin} U_0 |\psi_{\rm in}\rangle\langle\psi_{\rm in}| U_0^{\dagger})\, d|\psi_{\rm in}\rangle$, where $U_0 = \mathbb{1}$ is the desired unitary operator, $\rho_{\rm fin} = \varepsilon(\rho_{\rm in})$ is the actual mapping from the initial state to the final density matrix, and the normalized integral is over all pure initial states $|\psi_{\rm in}\rangle$ using the Haar measure. For a trace-preserving operation $F_{\rm av} = (F_{\chi} d + 1)/(d+1)$, where $d = 2$ is the dimension of a single-qubit Hilbert space [38]. This relation holds for many of the protocols discussed in this dissertation; however, for some procedures (i.e. uncollapsing and QED) there is a problem [13] in defining the QPT fidelity F_{χ} because the procedure is selective; then the quantum operation for normalized states is not linear and the corresponding (trace-preserving) χ-matrix cannot be defined rigorously. In this case we will use the scaled fidelity

$$F_{av}^{s} = (3F_{\rm av} - 1)/2, \tag{1.11}$$

as for a trace-preserving operation.

In the past the QPT fidelity has been used in experiments which involve selection of certain measurement results [14, 15, 16, 39], even though strictly speaking it is inapplicable in this case. Nevertheless, the fidelity F_{χ} can still be defined in the "naive" way by using 4 standard initial qubit states to calculate χ. However, we show in subsequent chapters that this "naive" fidelity practically coincides with the more

rigorous definition of the average state fidelity, when converted to the same scale using Eq. (1.11). The next section presents a simple example of these characterization and comparison methods.

1.4 Single qubit energy relaxation

This section presents the quantitative analysis of a single qubit subject to energy relaxation, one of the two main sources of decoherence in phase qubits. We only consider the zero-temperature limit since the typical phase qubit frequency is $\sim$6 GHz, and therefore the energy $\hbar\omega \simeq 0.3$ K is much larger than the experimental temperature of $\sim$50 mK. Throughout this dissertation, whenever discussing energy relaxation the zero-temperature limit is assumed (usually it will be mentioned explicitly). In this section we introduce notations and fidelity measures used in subsequent chapters, and describe a simple gedanken experiment that can be used for quantum error detection. In Ch. 2, 3, and 4 we will discuss realistic experimental protocols, suitable for phase qubits, to suppress the effect of this undesirable evolution.

Much of our analysis in this dissertation is based on unraveling the continuous decoherence due to energy relaxation into discrete "relaxation" and "no relaxation" scenarios. This unraveling is quite different (and more difficult) than, for example, unraveling pure dephasing into "phase flip" and "no phase flip" scenarios. The main reason for the difference is that the unraveled states for energy relaxation are related to the initial state in a non-unitary way. The fidelity measures from the previous section are calculated in two cases: when the occurrence of relaxation events is unknown and when they are perfectly monitored. The material present in this section is system-independent, the physical mechanism of energy relaxation in phase qubits is described

in Sec. 1.5.

Zero-temperature energy relaxation can be described in the following way. After time t an initial state $|\psi_{\rm in}\rangle = \alpha|0\rangle + \beta|1\rangle$ becomes the density matrix (in the computational basis defined in Sec. 1.2 where the upper row and left column correspond to the ground state $|0\rangle$)

$$\rho_{\rm fin} = \begin{pmatrix} |\alpha|^2 + |\beta|^2(1-e^{t/T_1}) & \alpha\beta^* e^{-t/2T_1} \\ \alpha^*\beta e^{-t/2T_1} & |\beta|^2 e^{-t/T_1} \end{pmatrix} \tag{1.12}$$

This can also be represented using the Kraus operators:

$$\rho_{\rm fin} = A_{\rm r}\rho_{\rm in}A_{\rm r}^\dagger + A_{\rm n}\rho_{\rm in}A_{\rm n}^\dagger, \tag{1.13}$$

$$A_{\rm r} = \begin{pmatrix} 0 & \sqrt{p} \\ 0 & 0 \end{pmatrix}, \quad A_{\rm n} = \begin{pmatrix} 1 & 0 \\ 0 & \sqrt{1-p} \end{pmatrix}, \tag{1.14}$$

where $p = 1 - e^{-t/T_1}$, $\rho_{\rm in} = |\psi_{\rm in}\rangle\langle\psi_{\rm in}|$, and the Kraus operators satisfy the completeness relation $A_{\rm r}^\dagger A_{\rm r} + A_{\rm n}^\dagger A_{\rm n} = \mathbb{1}$. This representation has an obvious interpretation as two scenarios of the evolution. The first term in Eq. (1.13) corresponds to qubit relaxation into the ground state $|0\rangle$ with probability $P_{\rm r} = |\beta|^2 p$. The second term is the no-relaxation scenario, which occurs with the remaining probability $P_{\rm n} = |\alpha|^2 + |\beta|^2(1-p) = 1 - P_{\rm r}$ and transforms the qubit into the state

$$|\psi_{\rm n}\rangle = \frac{A_{\rm n}|\psi_{\rm in}\rangle}{\sqrt{P_{\rm n}}} = \frac{\alpha|0\rangle + \beta\sqrt{1-p}\,|1\rangle}{\sqrt{P_{\rm n}}}. \tag{1.15}$$

The non-unitary evolution $|\psi_{\rm in}\rangle \to |\psi_{\rm n}\rangle$ is essentially the same as for a partial collapse due to a null-result measurement in the experiment of Ref. [40] (discussed in Sec. 1.6).

Now let us find the averaged state fidelity $F_{\rm av} = \overline{{\rm Tr}(\rho_{\rm f}|\psi_{\rm in}\rangle\langle\psi_{\rm in}|)}$ using unraveling into the relaxation and no-relaxation scenarios. With probability $P_{\rm r}$ the state fidelity is $F_{\rm st,r} = |\langle 0|\psi_{\rm in}\rangle|^2 = |\alpha|^2$, and with probability $P_{\rm n}$ the state fidelity is $F_{\rm st,n} =$

$|\langle\psi_{\rm n}|\psi_{\rm in}\rangle|^2 = (|\alpha|^2+\sqrt{1-p}|\beta|^2)^2/P_{\rm n}$. Therefore for an initial state $|\psi_{\rm in}\rangle$ the state fidelity is

$$F_{\rm st} = F_{\rm st,r}P_{\rm r} + F_{\rm st,n}P_{\rm n} \tag{1.16}$$

$$= |\alpha|^2|\beta|^2 p + |\alpha|^4 + (1-p)|\beta|^4 + 2|\alpha|^2|\beta|^2\sqrt{1-p}, \tag{1.17}$$

and the average fidelity $F_{\rm av} = \overline{F_{\rm st}}$ can be calculated by averaging $|\alpha|^4$, $|\beta|^4$, and $|\alpha|^2|\beta|^2$ over the Bloch sphere (see Appendix C for a more detailed discussion).

Applying the averages (C.3) and (C.4) to Eq. (1.17), we obtain the average state fidelity

$$F_{\rm av} = \frac{2}{3} + \frac{\sqrt{1-p}}{3} - \frac{p}{6}. \tag{1.18}$$

Actually, there is an easier way to obtain this result. Instead of averaging $F_{\rm st}$ over the Bloch sphere, it is sufficient [38, 41] (see also Appendix D) to calculate the average only over 6 initial states: $|0\rangle$, $|1\rangle$, $(|0\rangle \pm |1\rangle)/\sqrt{2}$, and $(|0\rangle \pm i|1\rangle)/\sqrt{2}$. However, in subsequent chapters this trick does not always help, so full integration over the Bloch sphere is preferred. Using Eq. (1.11) it is easy to convert Eq. (1.18) into the QPT fidelity: $F_\chi = (1+\sqrt{1-p}-p/2)/2$. Note that for small p

$$F_{\rm av} \approx 1 - \frac{p}{3}, \;\; F_\chi \approx 1 - \frac{p}{2}, \;\; p \approx \frac{t}{T_1} \ll 1. \tag{1.19}$$

The average state fidelity (1.18) is averaged over the two scenarios. Let us now discuss the average state fidelity in each scenario separately, having in mind a gedanken experiment in which an emitted photon or phonon is always captured and recorded, thus allowing us to distinguish the two scenarios. If the relaxation has happened, then $F_{\rm st,r} = |\alpha|^2$ and averaging this over the Bloch sphere we obtain

$$F_{\rm av,r} = \overline{|\alpha|^2} = 1/2. \tag{1.20}$$

Similarly, for the no-relaxation scenario $F_{\rm av,n} = \overline{(|\alpha|^2 + \sqrt{1-p}|\beta|^2)^2/[|\alpha|^2 + (1-p)|\beta|^2]}$, which can be calculated using Eqs. (C.9)–(C.11):

$$F_{\rm av,n} = \frac{1}{2} + \frac{\sqrt{1-p}(2-p) - 2(1-p)}{p^2} + \frac{(1-p)(2\sqrt{1-p} - 2 + p)}{p^3} \ln(1-p) \qquad (1.21)$$

For $p \ll 1$ this gives $F_{\rm av,n} \approx 1 - p^2/24$, showing a slow, quadratic in time decrease of fidelity in the no-relaxation scenario in contrast to the linear decrease (1.19) of the fidelity averaged over both scenarios. Therefore our gedanken experiment could be used for quantum error detection: if no relaxation is recorded, we know that the initial state is well-preserved at short times.

Note that we have averaged the state fidelities $F_{\rm st,r}$ and $F_{\rm st,n}$ over the Bloch sphere with uniform weight, as in the standard definition [7, 38] of the averaged state fidelity. Another meaningful averaging is using weights proportional to the probabilities of the corresponding scenarios. [This would correspond to an equal number of experimental runs for each point of a uniform mesh on the Bloch sphere, as opposed to an equal number of "successful" (i.e. selected) runs for the previous definition.] Thus defined average fidelities are

$$\widetilde{F}_{\rm av,r} = \overline{|\alpha|^2 P_{\rm r}}/\overline{P_{\rm r}} = 1/3, \qquad (1.22)$$

$$\widetilde{F}_{\rm av,n} = \overline{(|\alpha|^2 + \sqrt{1-p}|\beta|^2)^2}/\overline{P_{\rm n}} = \frac{2 - p + \sqrt{1-p}}{3 - 3p/2}, \qquad (1.23)$$

where $\overline{P_{\rm r}} = p/2$ and $\overline{P_{\rm n}} = 1 - p/2$ are the averaged probabilities of the two scenarios. The advantage of this definition is a natural formula for the non-selected average fidelity:

$$F_{\rm av} = \widetilde{F}_{\rm av,r}\overline{P_{\rm r}} + \widetilde{F}_{\rm av,n}\overline{P_{\rm n}} \qquad (1.24)$$

[see Eq. (1.16)]. In this dissertation when discussing selected scenarios (as for QED) we will use both ways to average over the Bloch sphere. Note that $\widetilde{F}_{\rm av,n} \approx 1 - p^2/24$ for $p \ll 1$, which is the same as for $F_{\rm av,n}$ ($\widetilde{F}_{\rm av,n}$ and $F_{\rm av,n}$ are practically indistinguishable

for $p \lesssim 1/2$), indicating that the difference between the two definitions is not very significant in the cases that are of most interest for this dissertation.

1.5 Superconducting flux-biased phase qubits

This section is a very brief and cursory introduction to superconducting phase qubits. For a more extensive description of phase qubit technology the reader is referred to the large body of existing literature [1, 14, 40, 42, 43, 44, 45, 46]. For our purposes it is sufficient to know the structure of the quantized states that will serve as the two-level system (qubit), available control, and measurement technique. First, the potential energy landscape is obtained from the circuit diagram of the flux-biased phase qubit. Then, we describe the basic idea of how the qubit state is controlled. Discussion of phase qubit measurement is reserved for the next section.

A circuit diagram illustrating the physical device used to create a flux-biased phase qubit is shown in Fig. 1.1. The potential energy of the system can be written, using Kirchoff's law and Josephson's equations, as

$$U(\delta) = E_J \left[\frac{(\delta - \phi)^2}{2\lambda} - \cos\delta \right], \tag{1.25}$$

where $E_J = \Phi_0 I_0 / 2\pi$ is the Josephson energy, $\lambda = 2\pi I_0 L / \Phi_0$ is the dimensionless inductance, $\phi = 2\pi\Phi/\Phi_0$ is the dimensionless external magnetic flux, I_0 is the critical current, and L is the inductance. This potential energy landscape is shown in Fig. 1.2. When operated near the critical current, the system can be modeled effectively as a two-well system with various numbers of quantized states in each well. When operated as a qubit, one well is kept "shallow" (3-5 levels), while the other is "deep" (100-500 levels). Within the "shallow" well, the lowest two energy eigenstates are used as the qubit basis states. These two states are referred to as the ground and first excited states

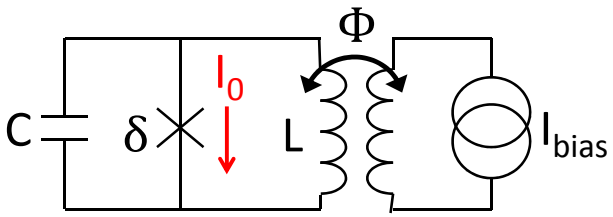

Figure 1.1: Circuit diagram for flux-biased phase qubit, where δ is the phase difference across the Josephson junction, Φ is the external flux applied through the inductor-junction loop, I^{bias} is the bias current used to apply the flux, L is the inductance of the loop, and I_0 is the critical current. The potential energy of this circuit is shown in Fig. 1.2(a) and the states which are used to create the phase qubit are shown in Fig. 1.2(b)

and are represented by wavefunctions $|0\rangle$ and $|1\rangle$ respectively.

Control of the qubit state is achieved by sending high-frequency pulses through the bias line in Fig. 1.1. The "shallow" well is approximated as a "cubic" potential (a parabola with a cubic anharmonicity), which means that the energy eigenstates are not equidistant as would be the case for a parabolic potential (i.e. the standard quantum harmonic oscillator). Therefore, pulses that are resonant with the energy difference between the two qubit basis states create coherent oscillations without populating higher levels (this is simply the usual Rabi oscillation of a driven two-level quantum system). By varying the amplitude and relative phase of the applied pulses any unitary operation can be performed on the qubit state. Only the existence, not the detailed mechanism, of this control is needed for the material presented in this dissertation. Subsequent chapters discuss only unitary operations on general qubit states (as was presented in Sec. 1.2 and is standard in the language of quantum computation). The validity and characterization of these single qubit controls has been well studied [42, 43].

For the phase qubit, zero-temperature energy relaxation is when an excited (or partially excited) qubit loses energy to its environment and eventually settles into the ground state. In a finite-temperature system, energy relaxation also includes the

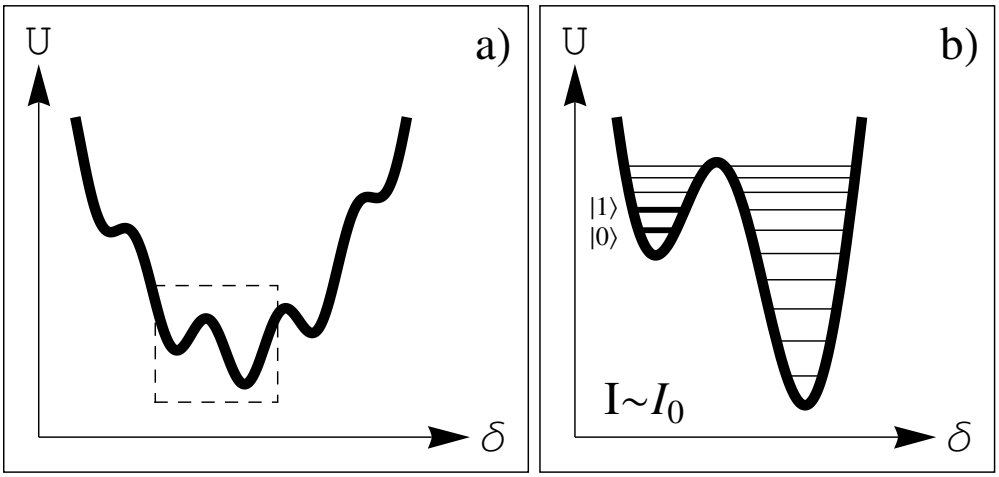

Figure 1.2: Representative plot of the potential energy as a function of the phase difference across the Josephson junction $U(\delta)$ of the flux-biased phase qubit circuit (shown in Fig. 1.1). a) The potential energy of the phase qubit circuit is essentially a parabola modulated by a cosine curve [see Eq. (1.25)]. b) When operated near the critical current of the Josephson junction ($I \sim I_0$) the lowest two energy levels of the "shallow" well form the basis states (labeled $|0\rangle$ and $|1\rangle$) of the phase qubit.

possibility of stray energy leaking into the qubit system and exciting its state; however, as was mentioned in the previous section, the typical phase qubit frequency is ∼6 GHz, and therefore the energy $\hbar\omega \simeq 0.3$ K is much larger than the experimental temperature of ∼50 mK. For this reason we only consider zero-temperature energy relaxation. Recall from Sec. 1.4 that after time t the evolution of a density matrix subject to energy relaxation is given by

$$\begin{pmatrix} \rho_{00} & \rho_{01} \\ \rho_{10} & \rho_{11} \end{pmatrix} \to \begin{pmatrix} \rho_{00} + \rho_{11}(1 - e^{t/T_1}) & \rho_{01}\, e^{-t/2T_1} \\ \rho_{10}\, e^{-t/2T_1} & \rho_{11}\, e^{-t/T_1} \end{pmatrix}. \tag{1.26}$$

where T_1 is the characteristic relaxation time. Current relaxation times in experiments with phase qubits are $T_1 \sim 500$ ns [14, 43].

As can be seen from Eq. (1.26) energy relaxation includes a certain amount of dephasing (exponential decay of the off-diagonal density matrix elements), there are two other sources of pure dephasing in the phase qubit. [The adjective "pure" signifies

that there is decay of only the off-diagonal density matrix elements.] In the language of density matrices this can be represented as

$$\begin{pmatrix} \rho_{00} & \rho_{01} \\ \rho_{10} & \rho_{11} \end{pmatrix} \rightarrow \begin{pmatrix} \rho_{00} & \rho_{01}\, e^{-t/T_\phi} \\ \rho_{10}\, e^{-t/T_\phi} & \rho_{11} \end{pmatrix}, \tag{1.27}$$

where T_ϕ is the characteristic dephasing time of the decoherence process. This type of pure dephasing arises from the fast "jitter" of the energy level of state $|1\rangle$ during a single experimental run. [Another type of dephasing with a gaussian decay is caused by the slow variation of the energy level during the many repeated experiments which are necessary for quantum state (or process) tomography [7].] Current dephasing times for phase qubits are $T_\phi \sim 400$ ns [14, 43]. [In the RezQu architecture [44, 45] , the qubit information is often stored in microwave resonators where pure dephasing is practically absent $T_\phi^{\text{res}} = \infty$, and therefore $T_2^{\text{res}} = 2T_1^{\text{res}}$.] We mainly focus on suppression techniques for the energy relaxation (although we briefly mention a quantum error detection procedure for pure dephasing in Ch. 4). Pure dephasing is included in all numerical simulations of proposed phase qubit experiments in Ch. 2 and 4.

In order to couple two phase qubits, their respective circuits are usually connected by a capacitive or inductive element. In Ch. 3 and 4 the usual capacitive coupling is assumed (as in previous experiments [42, 43, 46] and in the current RezQu architecture [44, 45]). For these chapters it is sufficient to know that the ZZ-type interaction of capacitive coupling gives rise to a natural entangling operation [43, 44, 45, 46] called a controlled-phase gate in the language of quantum computing [7]. A more sophisticated tunable inductive coupling is discussed in Ch. 5, where it is needed for the analyzed flying qubit protocol.

1.6 Measurement of phase qubits

In this section we discuss the three topics relating to the measurement of phase qubits: the technique used to perform a standard projective measurement, the procedure for performing a weak measurement, and the uncollapsing procedure for reversing a weak measurement of known strength. In general, low frequency pulses applied via the flux bias in Fig. 1.1 will lower the potential barrier between the two wells and allow a previously trapped excitation in one well to tunnel into the other well; this process is currently how measurement is performed. A schematic for the measurement of a phase qubit appears in Fig. 1.3. When an excitation in an energy eigenstate of the shallow well tunnels into the deeper well, it will quickly relax into a state with energy below that which is needed to return to the shallow well. This tunneling corresponds to a change in the superconducting phase across the Josephson junction (horizontal axis in Fig. 1.3), this change in phase causes a change in the flux through the qubit circuit. The new flux is detected using a standard SQUID (superconducting interference device) [47].

The tunneling process is described by the probability of jumping from eigenstate $|i\rangle$ after time t, which is given by

$$P_T^{(i)}(t) = 1 - e^{-\Gamma_i t}, \tag{1.28}$$

where Γ_i is the tunneling rate for state $|i\rangle$. [The tunneling process for state $|1\rangle$ is illustrated in Fig. 1.3.] Since the barrier is smaller for higher energy levels, the tunneling rate is larger for these states. During normal operation (no measurement), the well must be kept deep so the states used for qubit operations will not tunnel. This increase in depth comes at the cost of decreased anharmonicity (which is necessary to isolate the qubit basis states for coherent control – see the previous section).

In order to projectively measure the qubit state, a low frequency pulse decreases

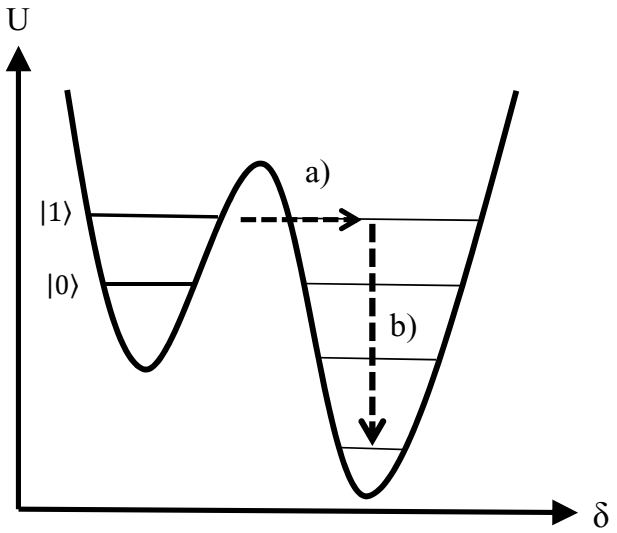

Figure 1.3: In order to measure the phase qubit, the well containing the basis states is "tilted", which allows state $|1\rangle$ to tunnel with rate Γ_1. a) The probability of state $|1\rangle$ tunneling after time t is $P_T^{(1)}(t) = 1 - e^{-\Gamma_1 t}$. b) After state $|1\rangle$ tunnels through the potential barrier it quickly relaxes into the deeper well.

the shallow well depth for a time t such that state $|1\rangle$ tunnels with certainty ($\Gamma_1 t \gg 1$), while state $|0\rangle$ still cannot tunnel ($\Gamma_0 t = 0$). If both conditions are met and a tunneling event is detected, then it is known that the excitation must have spent its last moment in state $|1\rangle$ before tunneling (and thus leaving the qubit Hilbert space). If tunneling is not detected, then the qubit is projected onto state $|0\rangle$. In reality the tunneling rate of state $|0\rangle$ is not exactly zero, $\Gamma_0 t \ll 1$, but this is negligible when compared to other errors in the protocols discussed in this dissertation.

A partial (weak) measurement is possible using this setup when $\Gamma_1 t \approx 1$ and no tunneling event is detected (null-result). After such a measurement, of duration t, a qubit initially in the state $\alpha|0\rangle + \beta|1\rangle$ will evolve as [15, 40, 48]

$$\alpha|0\rangle + \beta|1\rangle \rightarrow \frac{\alpha|0\rangle + \beta\sqrt{1-p}\,|1\rangle}{\sqrt{|\alpha|^2 + |\beta|^2(1-p)}}, \tag{1.29}$$

where $p = P_T^{(1)} = 1 - e^{-\Gamma_1 t}$ is the probability of tunneling from state $|1\rangle$. The parameter p is referred to as the "measurement strength" since the two limits $p \rightarrow 0$ and $p \rightarrow 1$ rep-

resent no-measurement and full projective measurement respectively. Renormalization is required since only null-result measurements are considered. It is natural to discard cases when tunneling is detected since this corresponds to a destructive projective measurement of state $|1\rangle$ (the system is no longer in the qubit Hilbert space).

After a weak measurement of known strength p has been performed, the non-unitary evolution of Eq. (1.29) can (surprisingly) be reversed, unlike the irreversible "textbook" collapse after a projective measurement. This reversal is accomplished by applying the following operations: swapping the states $|0\rangle$ and $|1\rangle$, applying another weak measurement of the same strength as the first (in this case p), and finally swapping the states once more. Swapping the two qubit basis states can be accomplished by applying the specific unitary rotation $\mathrm{R}_x(\pi)$ from Sec. 1.2; this operation is referred to as a π-pulse in the language of phase qubits or X-gate [2] in the language of quantum computing. The state after the first weak measurement and π-pulse is

$$\frac{\beta\sqrt{1-p}\,|0\rangle + \alpha|1\rangle}{\sqrt{|\alpha|^2 + |\beta|^2(1-p)}}. \tag{1.30}$$

If tunneling does not occur during the second measurement (which happens with probability $P_{nt} = |\alpha|^2 + |\beta|^2(1-p)$) then the qubit state after this step is

$$\frac{\beta\sqrt{1-p}\,|0\rangle + \alpha\sqrt{1-p}\,|1\rangle}{\sqrt{|\alpha|^2(1-p) + |\beta|^2(1-p)}}. \tag{1.31}$$

After canceling the factor of $\sqrt{1-p}$ and using the normalization condition of the initial state ($|\alpha|^2 + |\beta|^2 = 1$), Eq. (1.31) becomes $\beta|0\rangle + \alpha|1\rangle$. Clearly, the second π-pulse will return the qubit to its original superposition.

[2] Actually there is a (usually) insignificant phase difference between the usual definition of a π-pulse and the Pauli X-gate, $\mathrm{R}_x(\pi) = -iX$

Chapter 2

Decoherence Suppression via Weak Measurement Reversal

2.1 Introduction

In this chapter we present a procedure (similar to the usual quantum uncollapsing) which probabilistically suppresses qubit decoherence due to zero-temperature energy relaxation. As was introduced in Sec. 1.6, uncollapsing is a probabilistic reversal [2] of a partial quantum measurement by another measurement with an "exactly contradicting" result, so that the total classical information is zeroed, thus making it possible to restore any initial quantum state. If the second measurement gives this desired result, the initial state is recovered, while if the measurement result is different, the uncollapsing attempt is unsuccessful. The probability of success (selection) decreases with increasing strength of the first measurement, so that uncollapsing has zero probability for the traditional projective measurement. Perfect uncollapsing requires an ideal (quantum-efficient) detector.

From Sec. 1.5 recall that the logic states of the phase qubit are represented by

the two lowest energy levels in a quantum well, separated by ~ 25 μeV, and energy relaxation presents the major decoherence process, often nearly dominating in comparison with pure dephasing [43]. The experimental temperature of ~ 50 mK in this system essentially corresponds to the zero-temperature limit. This is exactly the regime in which uncollapsing can be used to suppress qubit decoherence (a similar zero-temperature regime with negligible pure dephasing is realized in transmon qubits [49]).

2.2 Ideal procedure

In order to protect the qubit from zero-temperature energy relaxation, we first apply a partial quantum measurement (Fig. 2.1), which moves the qubit state towards the ground state in a coherent but non-unitary way (Sec. 1.6). Then after the storage period we apply the uncollapsing procedure (for the phase qubit consisting of a π-pulse, second partial measurement, and one more π-pulse), which restores the initial qubit state. The procedure is probabilistic, since it selects only specific results of both measurements. (In this respect it is similar to linear optics quantum computing [50], which also relies on specific measurement results.) If an energy relaxation event happens during the storage period, then such a case will be preferentially rejected at the selection of the second measurement result. However, there is a trade-off: by increasing the strength of measurements we obtain stronger decoherence suppression, but decrease the selection probability.

To analyze the procedure quantitatively we will use the techniques introduced in Ch. 1. Let us assume that the initial state of the qubit in the rotating frame is $|\psi_{in}\rangle = \alpha|0\rangle + \beta|1\rangle$. The partial measurement is performed in the standard for the phase qubit way (see Sec. 1.6), by allowing state $|1\rangle$ to tunnel out of the quantum well

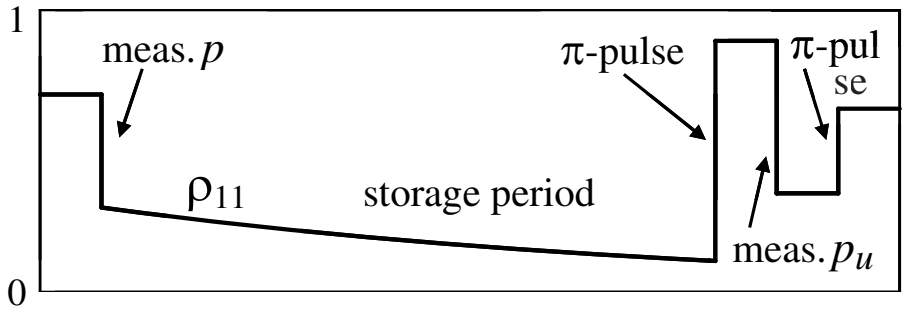

Figure 2.1: Illustration of the uncollapsing sequence used to suppress energy relaxation in a superconducting phase qubit: partial measurement with strength p, relatively long "storage" period, π-pulse, second measurement with strength p_u, and π-pulse. The line illustrates evolution of the element ρ_{11} of the qubit density matrix, other density matrix elements are similarly restored. We select only null-result cases for both measurements.

with the probability p, while state $|0\rangle$ cannot tunnel out [1]. In the null-result case of no tunneling the qubit state becomes [2]

$$|\psi_1\rangle = \alpha_1|0\rangle + \beta_1|1\rangle = \frac{\alpha|0\rangle + \beta\sqrt{1-p}\,|1\rangle}{\sqrt{|\alpha|^2 + |\beta|^2(1-p)}}, \tag{2.1}$$

and the probability of no tunneling is $P_1 = |\alpha|^2 + |\beta|^2(1-p)$.

After the storage period τ the qubit state is no longer pure because of (zero-temperature) energy relaxation with the rate $\Gamma = 1/T_1$. However, it is technically easier for us to "unravel" this process into "jump" and "no jump" scenarios, and work with pure states (this is a purely mathematical trick, which does not assume any jumps in reality – see Sec. 1.4). So, we can think that after the storage time τ the qubit jumps into the state $|0\rangle$ with the total probability $P_2^{|0\rangle} = P_1|\beta_1|^2(1 - e^{-\Gamma\tau})$, while it ends up in the state

$$|\psi_2\rangle = \alpha_2|0\rangle + \beta_2|1\rangle = \frac{\alpha|0\rangle + \beta\sqrt{1-p}\,e^{-\Gamma\tau/2}|1\rangle}{\sqrt{|\alpha|^2 + |\beta|^2(1-p)\,e^{-\Gamma\tau}}} \tag{2.2}$$

[1] In phase qubits, there is a chance that state $|0\rangle$ will tunnel during the measurement procedure, but this is a small effect and does not significantly change the efficiency of the procedure presented in this chapter.

[2] In real experiments with phase qubits [40] the partial measurement leads to an additional phase shift between states $|0\rangle$ and $|1\rangle$. We neglect it in Eq. (2.1) because it can be easily compensated and sometimes cancels out automatically [14, 17].

with "no jump" probability

$$P_2^{\rm nj} = |\alpha|^2 + |\beta|^2(1-p)\,e^{-\Gamma\tau}. \tag{2.3}$$

Notice that we made the Bayesian-like update [48] of the qubit state $|\psi_2\rangle$ in the "no energy jump" scenario (see Sec. 1.4); such update must be done even when the jump is not monitored, as can be easily checked by comparing the resulting density matrices. Also notice that the denominator in Eq. (2.2) is $(P_2^{\rm nj})^{1/2}$, as expected from the general theory of quantum measurement [7].

After applying the π-pulse the qubit state becomes either $|1\rangle$ or $\alpha_3|0\rangle+\beta_3|1\rangle = \alpha_2|1\rangle + \beta_2|0\rangle$ with the same probabilities $P_2^{|0\rangle}$ and $P_2^{\rm nj}$. Then after the second (uncollapsing) measurement with strength p_u, in the no-tunneling case the qubit remains in the state $|1\rangle$ with the total probability $P_4^{|1\rangle} = P_2^{|0\rangle}(1-p_u)$, while its state becomes

$$\alpha_4|0\rangle + \beta_4|1\rangle = \frac{\beta\sqrt{1-p}\,e^{-\Gamma\tau/2}|0\rangle + \alpha\sqrt{1-p_u}\,|1\rangle}{\sqrt{|\alpha|^2(1-p_u) + |\beta|^2(1-p)\,e^{-\Gamma\tau}}} \tag{2.4}$$

with probability $P_4^{\rm nj} = |\alpha|^2(1-p_u) + |\beta|^2(1-p)\,e^{-\Gamma\tau}$. Finally, the second π-pulse produces either the state $|0\rangle$ with probability $P_f^{|0\rangle} = P_4^{|1\rangle}$ or the final state

$$|\psi_f\rangle = \beta_4|0\rangle + \alpha_4|1\rangle \tag{2.5}$$

with probability $P_f^{\rm nj} = P_4^{\rm nj}$.

It is easy to see that in the "no jump" scenario the best (exact) restoration of the initial state is when

$$p_u = 1 - e^{-\Gamma\tau}(1-p), \tag{2.6}$$

and in this case the final state is

$$|\psi_f\rangle = |\psi_{in}\rangle \ \text{ with probability } \ P_f^{\rm nj} = (1-p)\,e^{-\Gamma\tau}, \tag{2.7}$$

$$|\psi_f\rangle = |0\rangle \ \text{ with } \ P_f^{|0\rangle} = |\beta|^2(1-p)^2 e^{-\Gamma\tau}(1-e^{-\Gamma\tau}). \tag{2.8}$$

In the language of density matrices this means that both measurements produce null results (no tunneling) with the selection probability $P_f = P_f^{\rm nj} + P_f^{|0\rangle}$, and in such a case the final qubit state is

$$\rho_f = \left(P_f^{\rm nj} |\psi_{in}\rangle\langle\psi_{in}| + P_f^{|0\rangle} |0\rangle\langle 0| \right) / (P_f^{\rm nj} + P_f^{|0\rangle}). \tag{2.9}$$

An important observation is that the "good" probability $P_f^{\rm nj}$ scales as $1-p$ with the measurement strength p, while the "bad" probability $P_f^{|0\rangle}$ scales as $(1-p)^2$. Therefore, choosing p close to 1, we can make the final qubit state *arbitrarily close to the initial state*, even in the presence of a significant decoherence due to energy relaxation ($\Gamma\tau \gtrsim 1$). This is the main result of this chapter.

It is tempting to say that the decoherence is suppressed because the storage state is close to the ground state, where the energy relaxation is naturally suppressed. However, a better explanation of the effect is that for the basis state $|0\rangle$ the energy relaxation is absent by itself, while for the basis state $|1\rangle$ the mechanism is the following: the first measurement keeps it as $|1\rangle$, but if the state jumps down to $|0\rangle$ during the storage period, then most likely there will be tunneling during the second measurement, and therefore such events will be eliminated by the selection of only null-result cases.

2.3 Results for the ideal procedure

The state fidelity $F_{st} = {\rm Tr}(\rho_f |\psi_{in}\rangle\langle\psi_{in}|)$ between the desired unevolved state $|\psi_{in}\rangle$ and the actual state ρ_f given by Eq. (2.9) is $F_{st} = 1 - |\beta|^2 P_f^{|0\rangle}/P_f$. In order to average F_{st} over the initial state we use the integration result

$$\overline{\frac{|\beta|^4}{A + B|\beta|^2}} = \frac{1}{2B} - \frac{A}{B^2} + \frac{A^2}{B^3} \ln(1 + \frac{B}{A}), \tag{2.10}$$

where the overline denotes averaging over the Bloch sphere (see Appendix C). Using $A = 1$ and $B = (1-p)(1-e^{-\Gamma\tau})$ [see Eqs. (2.7)–(2.9), the common factor $(1-p)e^{-\Gamma\tau}$ is canceled], we thus find

$$F_{av} = \frac{1}{2} + \frac{1}{C} - \frac{\ln(1+C)}{C^2}, \;\; C = (1-p)(1-e^{-\Gamma\tau}), \tag{2.11}$$

and the corresponding scaled fidelity $F^s_{av} = (3F_{av}-1)/2$ – see Eq. (1.11). It is important to notice that while the fidelity F^s_{av} increases with the measurement strength p, this happens for the price of decreasing the average selection probability $\overline{P_f} = (1-p)e^{-\Gamma\tau}(1+C/2)$. In particular, for $p \to 1$ we have $F^s_{av} \to 1$, but $\overline{P_f} \to 0$.

Recall from Sec. 1.3 that in experiments the one-qubit process fidelity F_χ is usually defined by starting with four specific initial states: $|0\rangle$, $|1\rangle$, $(|0\rangle + |1\rangle)/\sqrt{2}$, and $(|0\rangle + i|1\rangle)/\sqrt{2}$, measuring the corresponding final states ρ_f, then calculating the χ-matrix, and finally obtaining F_χ. Even for a non-linear quantum operation this is a well-defined procedure (just the result may depend on the choice of the four initial states), so it is meaningful to calculate F_χ defined in this (naive) way. It is obvious that such defined F_χ coincides with the usual F_χ for a linear trace-preserving operation, which gives the same final states for the four chosen initial states. Next, we use the fact [38](see also Appendix D) that the average fidelity F_{av} for this "substitute" operation is equal to F_{st} averaged over only 6 initial states: $|0\rangle$, $|1\rangle$, $(|0\rangle \pm |1\rangle)/\sqrt{2}$, and $(|0\rangle \pm i|1\rangle)/\sqrt{2}$. Since in our case F_{st} given by Eq. (1.17) is phase-insensitive, we get $F_{av} = [F_{st}(|0\rangle) + F_{st}(|1\rangle) + 4F_{st}(\frac{|0\rangle+|1\rangle}{\sqrt{2}})]/6$, which gives

$$F_{av} = \frac{1}{6} + \frac{1}{6(1+C)} + \frac{4+C}{3(2+C)}. \tag{2.12}$$

Then the "naive" fidelity is simply $F_\chi = (3F_{av}-1)/2$.

The efficiency of the energy relaxation suppression by uncollapsing is illustrated

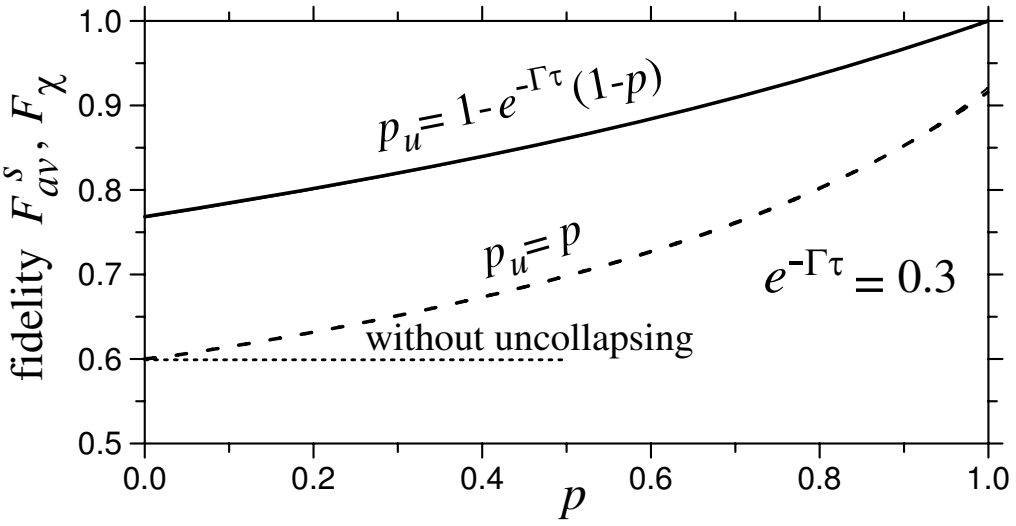

Figure 2.2: Fidelity of the quantum state storage using uncollapsing, as a function of the first measurement strength p for $e^{-\Gamma\tau} = 0.3$. Thick lines show F^s_{av}, while thin lines (practically indistinguishable from thick lines) show F_χ. Solid and dashed lines are for two choices of the second measurement strength p_u. The horizontal dotted line indicates fidelity without uncollapsing.

in Fig. 2.2 by plotting (solid lines) the scaled average fidelity F^s_{av} and the "naive" fidelity F_χ as functions of the measurement strength p for a quite significant energy relaxation: $e^{-\Gamma t} = 0.3$. Notice that F^s_{av} and F_χ are practically indistinguishable (within thickness of the lines), despite different functional dependencies in Eqs. (2.11) and (2.12). Also notice that even for $p = 0$ the fidelities differ from the fidelity without uncollapsing ($F_\chi = 1/2 + e^{-\Gamma\tau}/4 + e^{-\Gamma\tau/2}/2 \approx 0.6$), shown by the dotted line in Fig. 2.2. This is because we assumed $p_u = 1 - e^{-\Gamma\tau}(1-p)$, so $p_u \neq 0$ even for $p = 0$, and the second measurement improves the fidelity. If we choose $p_u = p$ (dashed lines) as in the standard uncollapsing [14, 2], then the case $p = 0$ is equivalent to the absence of any suppression procedure. [The dashed lines are calculated in a similar way, assuming $p_u = p$ in Eq. (2.4).] It is interesting to notice that if we numerically maximize the fidelity F^s_{av} by optimizing over p_u, then we can get larger F^s_{av} (for the same p) than in the case $p_u = 1 - e^{-\Gamma\tau}(1-p)$; however, this will decrease the selection probability $\overline{P_f}$, and for the same $\overline{P_f}$ such optimization slightly decreases F^s_{av}.

2.4 Non-ideal procedure

So far we assumed that the energy relaxation happens only during the storage period, while there is no decoherence during the uncollapsing procedure (measurements and π-pulses). Even though this assumption is justified since the storage period for a quantum memory is supposed to be relatively long, let us take a step closer to reality and take into account energy relaxation during all durations illustrated by horizontal lines in Fig. 1 (except the last one, which is after the procedure is finished). The energy relaxation (still zero-temperature) will be characterized by parameters $\kappa_i = \exp(-\Gamma\tau_i)$, $i = 1$–4, where τ_1 is the duration before the first measurement, $\tau_2 = \tau$ is the storage period, τ_3 is the duration between the first π-pulse and second measurement, and τ_4 is between the second measurement and second π-pulse (the measurements and π-pulses are still assumed ideal). Using the same derivation as above and selecting only the null-result cases for both measurements, we can show that for the initial state $|\psi_{in}\rangle = \alpha|0\rangle + \beta|1\rangle$ the final state can be unraveled (into three scenarios) as

$$|\psi_f^{\rm nj}\rangle = \frac{\alpha\sqrt{\kappa_3\kappa_4(1-p_u)}|0\rangle + \beta\sqrt{\kappa_1\kappa_2(1-p)}|1\rangle}{(P_f^{\rm nj})^{1/2}} \tag{2.13}$$

with the "no jump" probability

$$P_f^{\rm nj} = |\alpha|^2\kappa_3\kappa_4(1-p_u) + |\beta|^2\kappa_1\kappa_2(1-p), \tag{2.14}$$

the state

$$|\psi_f\rangle = |0\rangle \tag{2.15}$$

with probability

$$\begin{aligned} P_f^{|0\rangle} &= |\alpha|^2[1-\kappa_3+\kappa_3(1-p_u)(1-\kappa_4)] \\ &+ |\beta|^2[1-\kappa_1+\kappa_1(1-p)(1-\kappa_2)][1-\kappa_3+\kappa_3(1-p_u)(1-\kappa_4)], \end{aligned} \tag{2.16}$$

and also

$$|\psi_f\rangle = |1\rangle \tag{2.17}$$

with probability

$$P_f^{|1\rangle} = |\beta|^2[1-\kappa_1+\kappa_1(1-p)(1-\kappa_2)]\kappa_3(1-p_u)\kappa_4] \tag{2.18}$$

(all terms in these formulas have rather obvious physical meaning). The actual density matrix is then

$$\rho_f = (P_f^{\rm nj}|\psi_f^{\rm nj}\rangle\langle\psi_f^{\rm nj}| + P_f^{|0\rangle}|0\rangle\langle 0| + P_f^{|1\rangle}|1\rangle\langle 1|)/(P_f^{\rm nj} + P_f^{|0\rangle} + P_f^{|1\rangle}) \tag{2.19}$$

and the selection probability is

$$P_f = P_f^{\rm nj} + P_f^{|0\rangle} + P_f^{|1\rangle}. \tag{2.20}$$

It is also rather simple to take into account the additional decoherence due to the pure dephasing with rate Γ_φ. It can be shown that the only change will be the pure dephasing of the state (2.13) with the factor $\kappa_\varphi = \exp(-\Gamma_\varphi \sum_{i=1}^4 \tau_i)$.

The state fidelity can then be calculated in a straightforward way, and the averaging over the initial state can be performed as above using the integration result (2.10) and similar result

$$\overline{|\alpha|^4/(A+B|\beta|^2)} = -(3/2B) - (A/B^2) + (1/B)(1+B/A)^2\ln(1+B/A) \tag{2.21}$$

(see Appendix C). The final result for the scaled average fidelity F_{av}^s is analytical, but rather lengthy (as well as for F_χ and $\overline{P_f}$).

Solid lines in Fig. 2.3 show the p-dependence of the fidelities F_{av}^s and F_χ (they are still indistinguishable, being within the thickness of the line), for which we choose p_u from the equation

$$\kappa_3\kappa_4(1-p_u) = \kappa_1\kappa_2(1-p) \tag{2.22}$$

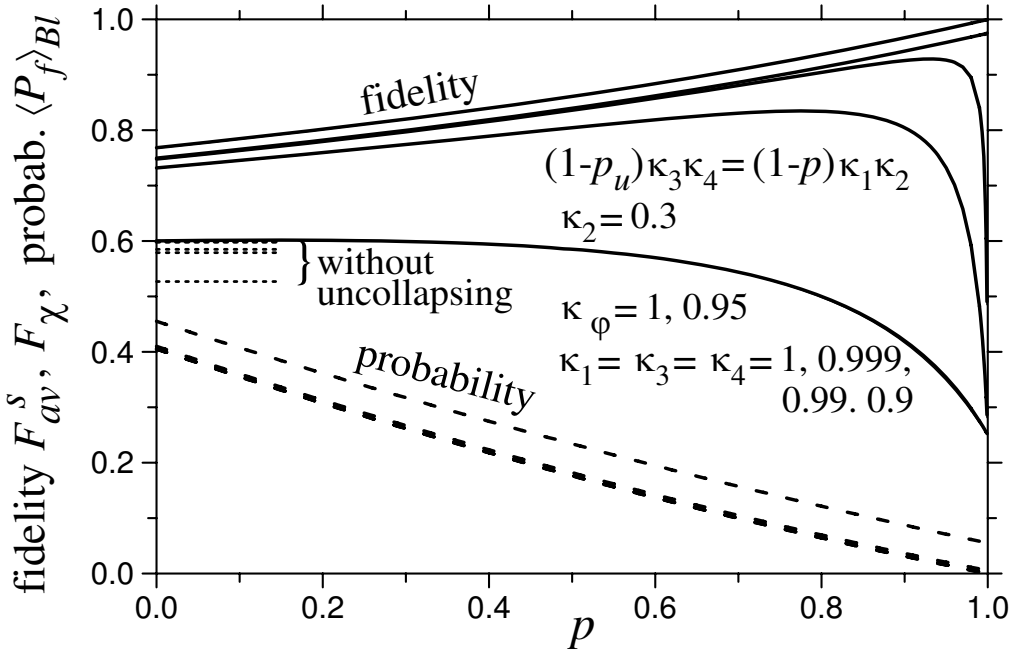

Figure 2.3: Solid lines: fidelities F^s_{av} and F_χ of the state storage (still practically indistinguishable from each other), taking into account the energy relaxation and pure dephasing during all parts of the uncollapsing procedure, for several sets of parameters (see text). Dashed lines: corresponding selection probabilities $\overline{P_f}$ (reverse order of curves). Dotted lines: corresponding fidelities without uncollapsing ($p = p_u = 0$).

which comes from Eq. (2.13) and generalizes the equation $1 - p_u = e^{-\Gamma\tau}(1 - p)$ from the previous section. For all solid lines we assume $k_2 = 0.3$. The upper line is for the ideal case $\kappa_1 = \kappa_3 = \kappa_4 = \kappa_\varphi = 1$ (so it is the same as in Fig. 2.2). For all other lines $\kappa_\varphi = 0.95$, while $\kappa_1 = \kappa_3 = \kappa_4 = 1$, 0.999, 0.99, 0.9 (from top to bottom). Dotted lines show corresponding fidelities in the absence of uncollapsing ($p = p_u = 0$; then

$$F^s_{av} = F_\chi = 1/4 + \kappa_E/4 + \kappa_\varphi\sqrt{\kappa_E}/2, \tag{2.23}$$

where $\kappa_E = \kappa_1\kappa_2\kappa_3\kappa_4$). The dashed lines show the average selection probability $\overline{P_f}$ of the procedure; these lines go in the opposite sequence (from bottom to top) compared to the solid and dotted lines.

As we see from Fig. 2.3, the uncollapsing essentially does not affect decoherence due to pure dephasing (κ_φ). Energy relaxation during the elements of the procedure

$(\kappa_1, \kappa_3, \kappa_4)$ has a less trivial effect: for small p it just reduces the fidelity, while for $p \to 1$ it causes the fidelity to drop down to 0.25 (this value corresponds to complete decoherence). The fidelity decrease is mainly affected by κ_3). Notice that the lowest solid line does not show a noticeable increase of the fidelity (with increasing p) before it starts to decrease. This behavior is similar to the results of the uncollapsing experiment [14], in which the "storage" time between the first measurement and π-pulse was not longer than other durations. Changing the experimental protocol of [14] by relative increase of the storage time, we would expect to observe an initial increase of the fidelity (with increasing p), thus confirming that uncollapsing can suppress decoherence. Notice that all solid lines in Fig. 2.3 are significantly above the standard fidelity (dotted lines, $p = p_u = 0$) for moderate measurement strength p. Significant increase of the fidelity is especially remarkable in view of the fact [11] that arbitrary Hamiltonian evolution cannot even slightly improve the fidelity in our case. So, the uncollapsing (which involves selection of certain measurement results) is *the only* known to us way of improving the qubit storage fidelity against energy relaxation, which does not rely on encoding a logical qubit in a larger Hilbert space.

Our idea also works for entangled qubits. Suppose now that the qubit is entangled with other qubits, which do not decohere. Parameterizing initial state as $\alpha|0\rangle|\psi_0\rangle + \beta|1\rangle|\psi_1\rangle$, it is easy to show that Eq. (2.13) changes only trivially, and the contribution to the state fidelity from the "no jump" scenario does not change at all, while several terms in the contribution from $|0\rangle$ and $|1\rangle$ will be multiplied by $|\langle\psi_0|\psi_1\rangle|^2$. Therefore, the results of this procedure do not change qualitatively for entangled qubits, though they change quantitatively.

Chapter 3

Repetitive quantum codes in the presence of energy relaxation

3.1 Introduction

In this chapter repetitive coding is analyzed in the presence of energy relaxation. Normally the three-qubit repetitive code is used to protect against a bit-flip (π-pulse) of any one of the three qubits (see Appendix B for a description of this usual implementation). If multiple errors happen much less frequently than single errors, then this code will indefinitely protect an arbitrary qubit state from bit-flip errors (by quick repetition relative to the rate of multiple errors). The purpose of the work in this chapter is to determine if repetitive coding can efficiently be used to protect a qubit from energy relaxation. It is shown that repetitive codes can be used for quantum error detection (QED), but cannot be used for the usual quantum error correction (QEC). QED is a selective process ideologically similar to the probabilistic decoherence suppression of Ch. 2, but requiring a larger Hilbert space.

Again we focus on decoherence suppression for superconducting phase qubits.

In the past, pure dephasing was by far the dominant source of decoherence in this system, and QEC protecting against pure dephasing would be most important. An example of such a procedure was considered theoretically in Ref. [51]. The idea was to use the standard 3-qubit repetitive code, which protects from bit flips (i.e. X-rotations). By using additional Hadamard gates for each physical qubit, the X-rotations are converted into Z-rotations, and therefore the same code can be used to protect against pure dephasing. In the language of quantum computing this is simply the standard phase-flip code [7].

In recent years, pure dephasing in superconducting qubits was significantly reduced by various technological advances [43, 31, 32, 33], and now energy relaxation is becoming most important. In particular, when quantum information is stored in a superconducting resonator [52, 44], pure dephasing is negligible in comparison with energy relaxation. This is why we focus on the operation of repetitive N-qubit quantum codes in the presence of energy relaxation. Repetitive codes are chosen because of their relative simplicity in the encoding and decoding (unfortunately, the standard 5-qubit or 7-qubit stabilizer codes [3, 5, 4, 6, 7, 53] are not feasible for superconducting qubits in the near future). To reduce the number of qubits in a procedure we use the standard compact scheme [19, 51], in which the ancilla qubits used for encoding are also used for the error syndrome measurement. As a reminder, we assume that the energy relaxation happens at zero temperature, which is essentially the case for superconducting phase qubits, since the typical qubit frequency is $\sim$6 GHz, and therefore the energy $\hbar\omega \simeq 0.3$ K is much larger than the experimental temperature of $\sim$50 mK.

Even though energy relaxation may look similar to a bit-flip, it actually can be thought of as a combination of two quantum errors: bit-flip and bit-phase-flip (which correspond to X-rotation and Y-rotation). This is the reason why, as we show later

explicitly, repetitive codes do not work for QEC against energy relaxation. However, these codes can be efficiently used for quantum error detection (QED). In QED we detect that an error happened but cannot restore the undamaged quantum state (in particular, the QED idea was implemented in Ref. [54] for phase errors in liquid-state NMR and has been recently investigated in Ref. [28] for detecting photon erasures). Even though QED is of much more limited use than QEC, it is still an interesting procedure, and experimentally can be considered as a first step towards full QEC. We show that for QED against energy relaxation it is sufficient to use 2-qubit encoding and that there is not much benefit to use more qubits, unless a somewhat more sophisticated procedure is used.

3.2 General procedure

The procedure for repetitive N-qubit encoding in the presence of (Markovian) zero-temperature energy relaxation is shown in Fig. 3.1. The goal is to preserve an arbitrary initial state

$$|\psi_{\rm in}\rangle = \alpha|0\rangle + \beta|1\rangle \tag{3.1}$$

of the main (upper) qubit, where $|0\rangle$ is the ground state and $|1\rangle$ is the excited state. In this chapter we consider only preservation of the initial state ("memory" operation), so in discussing the fidelity of a procedure we always imply comparison with the ideal memory operation.

The encoding in Fig. 3.1 is performed with $N-1$ controlled-NOT (CNOT) gates, acting on $N-1$ ancilla qubits, which all start in the state $|0\rangle$. This produces the N-qubit wavefunction $\alpha|0^N\rangle + \beta|1^N\rangle$, where the notation $|x^N\rangle$ represents the product-state of N qubits, all being in the state x (see Sec. 1.2). After the encoding, all qubits

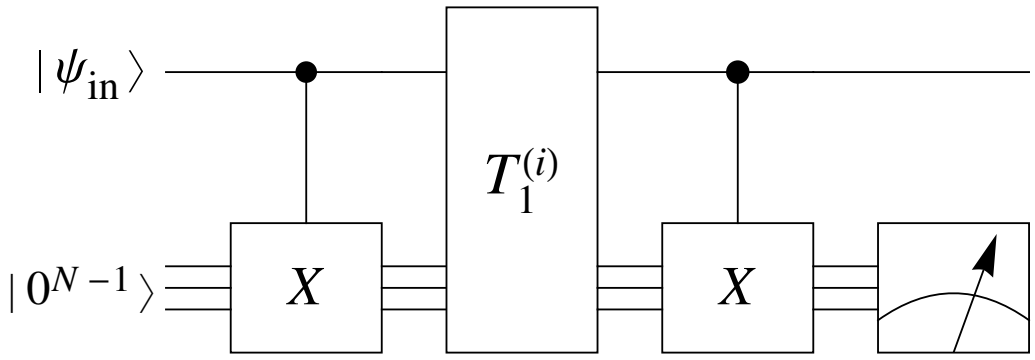

Figure 3.1: N-qubit repetitive coding algorithm with one control qubit initially containing the quantum information. The controlled-X block represents CNOT gates from the main qubit to each ancilla qubit individually. $T_1^{(i)}$ represents energy relaxation of the ith qubit ($i = 1$ for the main qubit, $i \geq 2$ for ancilla qubits).

are subjected to decoherence due to zero-temperature energy relaxation with relaxation time $T_1^{(i)}$ for the ith qubit, $i = 1, 2, \ldots N$. We will mostly consider the case when the decoherence is the same for all qubits, $T_1^{(i)} = T_1$. After the decoherence during time t, the logic state is decoded by using $N-1$ CNOT gates in the same way as was done for the encoding, and all $N-1$ ancilla qubits are measured in the computational basis. In the absence of decoherence ($t = 0$) the state after decoding is $(\alpha|0\rangle + \beta|1\rangle)\,|0^{N-1}\rangle$, so that the initial state of the main qubit is restored and the measurement results for all ancillas are 0. The decoherence disturbs the final state, which probabilistically changes the measurement results and corresponding final state of the main qubit.

Even when the measurement result is all $N-1$ zeros (for which we will use the bold-font notation $\mathbf{0}$), the state of the main qubit is not exactly $|\psi_{\rm in}\rangle$; however, we will see that it is close to $|\psi_{\rm in}\rangle$. A measurement result different from $\mathbf{0}$ indicates an error. There are three ways to handle this situation. First, the measurement result can be simply ignored; in this case there is obviously no benefit from using the encoding/decoding procedure. Second, we can reject such cases and keep only realizations with the mea-

surement result **0**; we will refer to this selective procedure as quantum error detection. Third, we can apply a quantum operation to the main qubit to make its state closer to $|\psi_{\rm in}\rangle$. This operation will depend on the measurement result, and the procedure is then quantum error correction.

For simplicity in this section we neglect decoherence (and other imperfections) during encoding, decoding, and measurement; it will be taken into account in the next chapter when we will discuss realistic experiments with phase qubits. As was discussed in Sec. 1.3, to characterize the efficiency of a procedure either the quantum process tomography (QPT) fidelity F_χ or the average state fidelity $F_{\rm av}$ can be used – we mainly consider the latter.

3.3 Two-qubit encoding

Let us use the procedure of Fig. 3.1 with only one ancilla qubit. The encoded state is then $\alpha|00\rangle+\beta|11\rangle$. The state evolution due to energy relaxation can be unraveled into four scenarios: no relaxation, relaxation in either the first (main) or second (ancilla) qubit, and relaxation in both qubits. The corresponding wavefunctions and probabilities after time t of energy relaxation are

$$\begin{cases} \dfrac{\alpha|00\rangle + \beta\sqrt{1-p_1}\sqrt{1-p_2}|11\rangle}{\sqrt{P_{\rm nn}}}, \\ \qquad \text{prob. } P_{\rm nn} = |\alpha|^2 + |\beta|^2 (1-p_1)(1-p_2), \\ |01\rangle, \ \text{ prob. } P_{\rm rn} = |\beta|^2 p_1(1-p_2), \\ |10\rangle, \ \text{ prob. } P_{\rm nr} = |\beta|^2 (1-p_1)p_2, \\ |00\rangle, \ \text{ prob. } P_{\rm rr} = |\beta|^2 p_1 p_2, \end{cases} \tag{3.2}$$

where

$$p_1 = 1 - e^{-t/T_1^{(1)}}, \ \ p_2 = 1 - e^{-t/T_1^{(2)}} \tag{3.3}$$

are the single-qubit probabilities of relaxation from the excited state $|1\rangle$. This simple unraveling is possible because the energy relaxation occurs only in component $|11\rangle$ of the superposition, and in this component the qubits are unentangled. This is why the probabilities of the scenarios are the simple products of individual probabilities. The validity of Eq. (3.2) can also be checked by considering particular time moments at which the relaxation events happen and integrating over these moments; this is a more direct but more cumbersome way.

After the decoding procedure consisting of one CNOT operation, the two-qubit state is a product-state in all four scenarios:

$$\begin{cases} \dfrac{\alpha|0\rangle + \beta\sqrt{1-p_1}\sqrt{1-p_2}|1\rangle}{\sqrt{P_{\rm nn}}} \otimes |0\rangle, \text{ prob. } P_{\rm nn}, \\ |01\rangle, \text{ prob. } P_{\rm rn}, \\ |11\rangle, \text{ prob. } P_{\rm nr}, \\ |00\rangle, \text{ prob. } P_{\rm rr}, \end{cases} \tag{3.4}$$

with a definite result of the ancilla qubit measurement in each scenario. The state of the main qubit is different from the initial state $|\psi_{\rm in}\rangle$ in all four scenarios, and the corresponding state fidelities are $[|\alpha|^2 + |\beta|^2\sqrt{1-p_1}\sqrt{1-p_2}]^2/P_{\rm nn}$, $|\alpha|^2$, $|\beta|^2$, and $|\alpha|^2$.

As discussed in the previous section, we consider three ways to proceed: ignore the measurement result, select only result 0, or try to correct the main qubit state. If the measurement result is ignored, then all four scenarios are added up and the average fidelity is

$$\begin{aligned} F_{\rm av}^{\rm ign} = &\overline{[|\alpha|^2 + |\beta|^2\sqrt{1-p_1}\sqrt{1-p_2}]^2} \\ &+\overline{|\alpha|^2 P_{\rm rn} + |\beta|^2 P_{\rm nr} + |\alpha|^2 P_{\rm rr}}, \end{aligned} \tag{3.5}$$

where the averaging is over the Bloch sphere (see Sec. 1.3 or Appendices C and B for more information). Using the formulas for the probabilities from Eq. (3.2) and the

averages $\overline{|\alpha|^2}$, $\overline{|\beta|^2}$, $\overline{|\alpha|^4}$, $\overline{|\beta|^4}$, and $\overline{|\alpha|^2|\beta|^2}$ from Eqs. (C.3)–(C.5), we obtain

$$F_{\rm av}^{\rm ign} = \frac{2}{3} + \frac{\sqrt{(1-p_1)(1-p_2)}}{3} - \frac{p_1}{6} \tag{3.6}$$

For small $p_{1,2}$ (at short time t) it is $F_{\rm av}^{\rm ign} \approx 1 - p_1/3 - p_2/6$, and it is obviously worse than the case without encoding/decoding of the main qubit – see Eqs. (1.18) and (1.19). Note that Eq. (3.6) can also be obtained by averaging the state fidelity only over the 6 initial states (see Appendix D).

In quantum error detection we consider ancilla measurement result 1 as an error and select only the cases when the measurement gives 0. This selects scenarios with either no relaxation or two relaxation events [see the first and last lines of Eq. (3.4)]. The averaged (with uniform weight) state fidelity in this case is

$$F_{\rm av}^{\rm qed} = \frac{\overline{[|\alpha|^2 + |\beta|^2\sqrt{1-p_1}\sqrt{1-p_2}]^2 + |\alpha|^2 P_{\rm rr}}}{P_{\rm nn} + P_{\rm rr}} \tag{3.7}$$

(the fraction is averaged over the Bloch sphere), which can be calculated using Eqs. (C.9)–(C.11):

$$\begin{aligned} F_{\rm av}^{\rm qed} = \frac{1}{2} + \frac{s-1}{B} + \frac{p_1+p_2-2+2s}{B^2} \\ + \frac{(1+B)^2 + s^2 - (1+B)(2s+p_1p_2)}{B^3} \ln(1+B), \end{aligned} \tag{3.8}$$

where $B = 2p_1p_2 - p_1 - p_2$ and $s = \sqrt{1-p_1}\sqrt{1-p_2}$. For the small-error case (at short time t) this gives

$$F_{\rm av}^{\rm qed} \approx 1 - (p_1^2 + p_2^2)/24 - 5p_1p_2/12, \;\; p_{1,2} \ll 1. \tag{3.9}$$

If we average over the Bloch sphere with weight proportional to the probability $P_{\rm nn} + P_{\rm rr}$ of the measurement result 0 (this alternative averaging is discussed in Sec. 1.4 in the context of a single qubit), then

$$\widetilde{F}_{\rm av}^{\rm qed} = \frac{\overline{[|\alpha|^2 + |\beta|^2\sqrt{1-p_1}\sqrt{1-p_2}]^2 + |\alpha|^2 P_{\rm rr}}}{\overline{P_{\rm nn} + P_{\rm rr}}}, \tag{3.10}$$

(the numerator and denominator are averaged separately), which gives

$$\widetilde{F}_{\rm av}^{\rm qed} = \frac{2 - p_1 - p_2 + \frac{3}{2}p_1 p_2 + \sqrt{1-p_1}\sqrt{1-p_2}}{3[1 + p_1 p_2 - (p_1 + p_2)/2]}. \tag{3.11}$$

[Note that instead of using Eqs. (C.3)–(C.5), the 6-point averaging trick can be used separately for the numerator and denominator of Eq. (3.10) – see Appendix D.] At short times this gives $\widetilde{F}_{\rm av}^{\rm qed} \approx 1 - (p_1^2 + p_2^2)/24 - 5p_1 p_2/12$, same as for $F_{\rm av}^{\rm qed}$ [see Eq. (3.9)].

Figure 3.2 shows the QED fidelity defined in both ways, $F_{\rm av}^{\rm qed}$ and $\widetilde{F}_{\rm av}^{\rm qed}$, as functions of the one-qubit relaxation probability, assuming similar qubits, $p_1 = p_2 = p$. For $p \lesssim 0.3$ both fidelities are significantly higher than the fidelity $F_{\rm av}^{\rm 1q}$ for an unencoded single qubit [given by Eq. (1.18)], which itself is higher than the fidelity $F_{\rm av}^{\rm ign}$ when the ancilla measurement result is ignored [Eq. (3.6)].

Now let us discuss whether or not the state of the main qubit can be made closer to $|\psi_{\rm in}\rangle$ using the measurement result information, as in quantum error correction. If the measurement result is 0, then the qubit state is described by the first and last lines of Eq. (3.4). It is rather obvious that in this case no unitary operation can improve further the average fidelity [for QEC we are interested in averaging with the weight proportional to probability – see Eq. (1.24)]. This statement is rigorously proven in Appendix D. So, no correction should be applied for measurement result 0. (Actually, a non-unitary operation due to partial collapse can increase the fidelity in this case [14, 15, 17, 13, 55, 56], but we consider only unitary operations, as it should be in the usual QEC.) When the measurement result is 1, the main qubit is in the state $|0\rangle$ with probability $P_{\rm rn}/(P_{\rm rn} + P_{\rm nr})$ or in the state $|1\rangle$ with remaining probability $P_{\rm nr}/(P_{\rm rn} + P_{\rm nr})$ – see Eq. (3.4). In the case $p_1 = p_2$ this is the fully mixed state, and any unitary operation does not change it. Thus a meaningful error correction is impossible, and therefore $F_{\rm av}^{\rm qec} = F_{\rm av}^{\rm ign}$ (see Fig. 3.2).

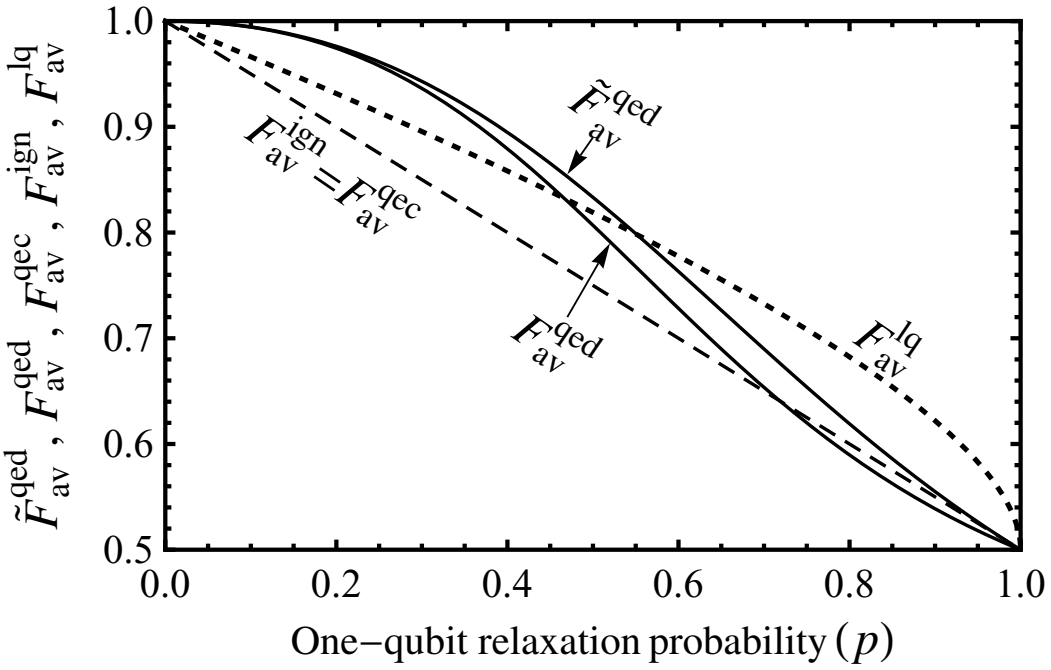

Figure 3.2: Average state-preservation fidelities for the two-qubit encoding (compared with no encoding), as functions of the one-qubit energy relaxation probability $p = 1 - e^{-t/T_1}$ (same for both qubits, $p_1 = p_2 = p$). The solid lines show the QED fidelities $F_{\rm av}^{\rm qed}$ and $\widetilde{F}_{\rm av}^{\rm qed}$ given by Eqs. (3.8) and (3.11). ($F_{\rm av}^{\rm qed}$ assumes averaging over the Bloch sphere with uniform weight, while for $\widetilde{F}_{\rm av}^{\rm qed}$ the weight is proportional to the probability of the "no error" measurement result 0.) The dashed line shows the QEC fidelity $F_{\rm av}^{\rm qec}$, which coincides with $F_{\rm av}^{\rm ign}$, for which the measurement result is ignored, Eqs. (3.6) and (3.12). The dotted line shows the one-qubit fidelity $F_{\rm av}^{\rm 1q}$ without encoding, Eq. (1.18). QEC performs worse than no encoding, while QED provides a significant improvement for $p \lesssim 0.3$.

Actually, if $p_2 > p_1$, then a slight improvement of fidelity is possible by applying the π-pulse (exchanging states $|0\rangle$ and $|1\rangle$) when the measurement result is 1. This makes the resulting state closer to $|1\rangle$ than to $|0\rangle$, and correspondingly on average closer to $|\psi_{\rm in}\rangle$, because the probability of measuring 1 increases with $|\psi_{\rm in}\rangle$ being closer to $|1\rangle$. The optimality of this procedure for measurement result 1 is proven in Appendix D. It is easy to calculate the fidelity change due to the π-pulse (the easiest way is to average over the 6 initial states and to work with unnormalized states – see Appendix D). The resulting optimal QEC fidelity for the 2-qubit encoding of Fig. 3.1 is

$$F_{\rm av}^{\rm qec} = \frac{2}{3} + \frac{\sqrt{(1-p_1)(1-p_2)}}{3} - \frac{\min(p_1,p_2)}{6}. \tag{3.12}$$

3.4 N-qubit encoding

We now extend our discussion of the protocol of Fig. 3.1, now including $N-1$ ancilla qubits. The encoded state is then $\alpha|0^N\rangle + \beta|1^N\rangle$. The state evolution can be unraveled into 2^N scenarios depending on which qubits relax. However, there are 2^{N-1} measurement results, and each of them corresponds to two scenarios. If the main qubit does not relax, then the measurement result directly shows which ancilla qubits relax (i.e. result 1 indicates the relaxation event – see Appendix E), while if the main qubit relaxes, then the relaxation scenario is shown by the complement of the measurement result (i.e. result 0 indicates relaxation).

The measurement result **0** (all zeros) indicates that the main qubit is either in the state

$$|\psi_{\rm none}\rangle = \frac{1}{\sqrt{P_{\rm none}}}\left(\alpha|0\rangle + \beta|1\rangle \prod\nolimits_{j=1}^{N} \sqrt{1-p_j}\right), \tag{3.13}$$

where $P_{\rm none} = |\alpha|^2 + |\beta|^2 \prod_{j=1}^{N}(1-p_j)$ is the probability that no qubits relax, or in the state $|0\rangle$ if all qubits relax, with the corresponding probability $P_{\rm all} = |\beta|^2 \prod_{j=1}^{N} p_j$. For any other measurement result the main qubit is either in state $|0\rangle$ or $|1\rangle$, with easily calculable probabilities of the scenarios. For simplicity we assume $p_j = p$ below.

As in the previous discussions, we consider three possible ways to proceed: ignore the measurement result, select only cases with measurement result **0** (QED), or try to improve the fidelity when an error is detected (QEC). If the measurement result is ignored, the average fidelity (calculated in a similar way as above) is

$$F_{\rm av}^{\rm ign} = \frac{2}{3} + \frac{(1-p)^{N/2}}{3} - \frac{p}{6}; \tag{3.14}$$

it obviously decreases with increasing number of ancilla qubits.

In quantum error detection we select only cases with measurement result **0**. Then the state fidelity is

$$F_{\rm st}^{\rm qed} = \frac{(|\alpha|^2 + |\beta|^2(1-p)^{N/2})^2 + |\alpha|^2 P_{\rm all}}{P_{\rm none} + P_{\rm all}}, \tag{3.15}$$

and averaging it over the Bloch sphere with uniform weight we obtain

$$\begin{aligned} F_{\rm av}^{\rm qed} = {} & \frac{-3 + S + (1-p)^N}{2B} + \frac{-1 + S - (1-p)^N}{B^2} \\ & + \frac{(1+B)^2 + (1-p)^N - S(1+B)}{B^3} \ln(1+B), \end{aligned} \tag{3.16}$$

where $B = -1 + (1-p)^N + p^N$ and $S = 2(1-p)^{N/2} + p^N$. For $N = 2$ this equation corresponds to Eq. (3.8). The small-error approximation for $N \geq 3$ is

$$F_{\rm av}^{\rm qed} \approx 1 - N^2 p^2/24, \;\; p \ll 1. \tag{3.17}$$

It is interesting to note that this approximation does not work for $N = 2$, for which $F_{\rm av}^{\rm qed} \approx 1 - p^2/2$, as follows from Eq. (3.9). The reason is that $P_{\rm all}$ scales as p^N, and therefore for $N \geq 3$ Eq. (3.17) does not have a quadratic contribution from the scenario

when all qubits relax; the infidelity comes only from the difference between $|\psi_{\rm none}\rangle$ and $|\psi_{\rm in}\rangle$. In contrast, for $N = 2$ the fidelity $F_{\rm av}^{\rm qed}$ is further decreased by $p^2/3$ due to relaxation of both qubits.

From Eqs. (3.17) and (3.9) we see that the best QED fidelity in the small-error case ($p \ll 1$) is achieved by the 3-qubit encoding, $N = 3$; then $1 - F_{\rm av}^{\rm qed} \approx (3/8)\, p^2$. However, this is only the factor 4/3 better (smaller) than for $N = 2$. Therefore, from the experimental point of view the 2-qubit encoding (which is easier to realize than the 3-qubit encoding) seems to be most natural.

If we use the averaging of the QED state fidelity (3.15) with weights proportional to the probability $P_{\rm none} + P_{\rm all}$ of the measurement result $\mathbf{0}$, then we essentially need to average the numerator and denominator of Eq. (3.15) separately, thus obtaining

$$\widetilde{F}_{\rm av}^{\rm qed} = \frac{2}{3}\,\frac{1 + (1-p)^N + (1-p)^{N/2} + \frac{1}{2}p^N}{1 + (1-p)^N + p^N}. \tag{3.18}$$

In the small-error case ($p \ll 1$) for $N \geq 3$ this gives $\widetilde{F}_N^{\rm qed} \approx 1 - N^2 p^2/24$, same as Eq. (3.17) for $F_N^{\rm qed}$.

Figure 3.4(a) shows the QED fidelities $F_{\rm av}^{\rm qed}$ and $\widetilde{F}_{\rm av}^{\rm qed}$ for $N = 2$, 3, and 4. We see that the difference between $F_{\rm av}^{\rm qed}$ and $\widetilde{F}_{\rm av}^{\rm qed}$ becomes larger with increasing N, but the difference is small at small p. Note that the QED fidelity for the 2-qubit encoding becomes better than for the 3-qubit encoding for $p \gtrsim 0.3$.

Now let us discuss the possibility of QEC protocols, which use unitary correcting operations depending on the measurement result. If the result is $\mathbf{0}$, then the unnormalized density matrix of the main qubit is $P_{\rm none}|\psi_{\rm none}\rangle\langle\psi_{\rm none}| + P_{\rm all}|0\rangle\langle 0|$. As is proven in Appendix D, no unitary operation can increase the fidelity in this case (in contrast to non-unitary partial-collapse operations [14, 15, 17, 13, 55, 56]). For all other measurement results, the main qubit is in the incoherent mixture of the states $|0\rangle$ and

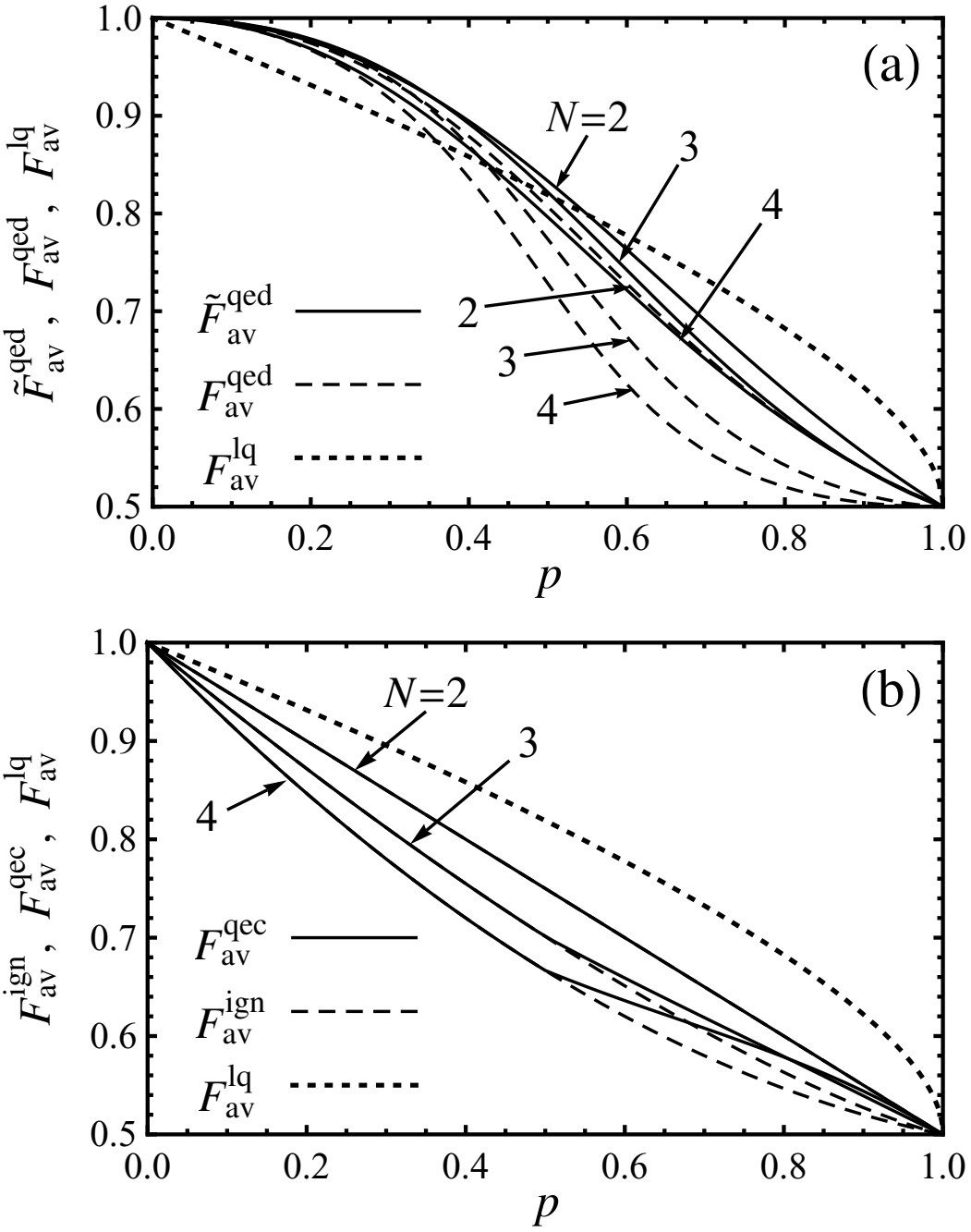

Figure 3.3: (a) The QED fidelities $\widetilde{F}_{\rm av}^{\rm qed}$ (solid lines) and $F_{\rm av}^{\rm qed}$ (dashed lines) for the encoding using $N = 2$, 3, and 4 physical qubits, as functions of the single-qubit energy relaxation probability p. The dotted line shows the fidelity $F_{\rm av}^{\rm 1q}$ for an unencoded qubit. (b) The optimal QEC fidelity $F_{\rm av}^{\rm qec}$ (solid lines) and the fidelity $F_{\rm av}^{\rm ign}$ when the measurement result is ignored (dashed lines) for $N = 2$, 3, and 4.

$|1\rangle$; the unnormalized density matrix is $P_{0,\mathrm{m}}|0\rangle\langle 0| + P_{1,\mathrm{m}}|1\rangle\langle 1|$, where the corresponding probabilities are $P_{1,\mathrm{m}} = |\beta|^2(1-p)\prod_{i=2,N} f(m_i)$ and $P_{0,\mathrm{m}} = |\beta|^2 p \prod_{i=2,N} f(1-m_i)$, where $f(1) = p$, $f(0) = 1-p$, and m_i is the measurement result for the ith ancilla qubit. As is shown in Appendix D, the maximum fidelity is then achieved by applying the π-pulse (exchanging $|0\rangle$ and $|1\rangle$) if $P_{1,\mathrm{m}} < P_{0,\mathrm{m}}$ and doing nothing if $P_{1,\mathrm{m}} \geq P_{0,\mathrm{m}}$. Calculating the corresponding qubit state fidelity (compared with the initial state), summing over the 2^{N-1} measurement results, and averaging over the Bloch sphere, we obtain the QEC fidelity

$$F_{\mathrm{av}}^{\mathrm{qec}} = \frac{1}{2} + \frac{1}{3}(1-p)^{N/2} + \frac{1}{6}(1-p)^N + \frac{1}{6}\max[p - p^N,\, (1-p) - (1-p)^N]. \tag{3.19}$$

The QEC fidelity as well as the fidelity $F_{\mathrm{av}}^{\mathrm{ign}}$ for ignoring the measurement result are shown in Fig. 3.4(b) for $N = 2$, 3, and 4. The curves for $F_{\mathrm{av}}^{\mathrm{qec}}$ and $F_{\mathrm{av}}^{\mathrm{ign}}$ coincide at $p \leq 1/2$, because in this case the optimal correction is no correction. We see that for any N the QEC fidelity is smaller than the no-encoding fidelity $F_{\mathrm{av}}^{\mathrm{1q}}$, so the error correction by a repetitive code does not protect against energy relaxation.

3.5 Discussion

Our results show that repetitive codes do not work for QEC protection against energy relaxation. This is because energy relaxation is very different from a bit flip (or phase flip or bit-phase flip), for which repetitive codes work well. In the language of quantum stabilizer codes [7] the event of energy relaxation corresponds to the "sum" of two errors: bit flip (X-operation) and bit-phase flip (Y-operation) – see the Kraus operator A_{r} in Eq. (1.14). So, a stabilizer code should be able to protect against both of these errors to protect against energy relaxation events. [Actually, a weaker error due

to the "no relaxation" Kraus operator $A_{\rm r}$ in Eq. (1.14) also requires protection against phase flip (Z-operation) errors.] For example, the standard 5-qubit and 7-qubit QEC codes [3, 4, 5, 6, 7, 53] protect against all 3 types of errors (X, Y, Z), and therefore can protect against energy relaxation.

Using the approach of stabilizer codes and the quantum Hamming bound [7], let us calculate the minimum number of qubits N to protect against X and Y errors. The Hilbert space of the dimension 2^N can be divided into 2^{N-1} orthogonal two-dimensional subspaces ("copies" of the qubit space); these subspaces should be able to distinguish the cases with various errors and no error. Since the number of possible errors is $2N$, we have an inequality $2^{N-1} \geq 1 + 2N$. From this inequality we find $N \geq 5$ (the same minimum as for all 3 types of quantum errors). Notice, however, that an approximate QEC for energy relaxation is possible for $N = 4$ [57] (see also [58, 59]). This code breaks the above limitation because the relaxation event is treated as one error, not as a "sum" of X and Y (the drawback though is a slightly probabilistic operation). In any case, the QEC codes protecting against energy relaxation are much more complicated than the repetitive codes.

Even though the repetitive codes are not good for QEC protection against energy relaxation, we have shown that they can be well used for QED. Moreover, only 2-qubit encoding is sufficient for that. An interesting question is whether or not it is beneficial to do many cycles of QED, correspondingly decreasing the time of each cycle and therefore the error probability p in each cycle (such division into shorter cycles is beneficial for QEC [3, 4, 5, 6, 7]). The simple answer is that such division into shorter cycles does not help much for the protocol of Fig. 3.1. The reason is that even when no relaxation events happen, the qubit state changes – see Eq. (3.13), because the absence of relaxation preferentially indicates state $|0\rangle$ and plays the same role as

the partial collapse [14]. Rewriting Eq. (3.13) in a non-normalized way as $|\tilde{\psi}_{\rm none}\rangle = \alpha|0\rangle + \beta|1\rangle \prod_{j=1}^{N} \exp(-t/2T_{1,j})$, we see that division into several QED cycles does not change the final wavefunction $|\tilde{\psi}_{\rm none}\rangle$ as long as the total time t is the same. Therefore, since for $N \geq 3$ this evolution is the main reason for imperfect QED fidelity at $p \ll 1$ (see discussion in the previous section), there is not much benefit of using the QED cycles. Nevertheless, some improvement of the QED fidelity will be due to a decrease of the probability $P_{\rm all}$ that all qubits relax. Since this probability scales as $p^N \approx (t/T_1)^N$, the division into M cycles is expected to decrease the corresponding contribution to the procedure infidelity by the factor M^{N-1}. This improvement will be most significant for $N = 2$: it will essentially change the approximation $F_{\rm av}^{\rm qed} \approx 1 - p^2/2$ given by Eq. (3.9) into $F_{\rm av}^{\rm qed} \approx 1 - p^2/6$ given by Eq. (3.17) for $N = 2$.

A more important improvement of the QED fidelity can be achieved if the no-relaxation evolution (3.13) of $|\psi_{\rm none}\rangle$ is compensated. One way is to apply a partial measurement [13, 14, 55, 56] to the main qubit after the procedure, essentially eliminating the evolution (3.13) for the price of a further decrease of the selection probability (probability of success). Another, easier way is to apply π-pulses, exchanging states $|0\rangle$ and $|1\rangle$, between (after) the QED cycles (these π-rotations can be around any axis in the equatorial plane of the Bloch sphere). Then for an even number of equal-duration QED cycles, the no-relaxation evolution (3.13) will be compensated exactly (as in the uncollapsing procedure [2, 14, 13, 55, 56, 15, 17]), and the QED infidelity $1 - F^{\rm qed}$ will be only due to the contribution from $P_{\rm all}$. (The use of π-pulses resembles dynamical decoupling of the "bang-bang" type [60]; however, the resemblance is accidental, since dynamical decoupling cannot protect against the energy relaxation [11].)

For an estimate of the corresponding QED fidelity, let us consider the procedure with total duration $t \lesssim T_1$, divided into M cycles of duration t/M each (M is even).

In each cycle $p \approx t/MT_1 \ll 1$, and if we assume $Nt/MT_1 \ll 1$, then $|\psi_{\rm none}\rangle \approx |\psi_{\rm in}\rangle$ in Eq. (3.13). The probability that the N-qubit relaxation (which remains undetected) happened in the first cycle is $P_{\rm all} = |\beta|^2 p^N$, and similar probability for the second cycle (after π-pulse) is $|\alpha|^2 p^N$. Therefore, in a selected QED realization (with all measurement results **0**) the probability to have an undetected relaxation event is $(M/2)p^N$, independent of the initial state (we assume this probability to be small, then we can neglect the double-events). If such an undetected relaxation event happens, then the average fidelity is $\widetilde{F}_{\rm av} = \overline{|\alpha|^2|\beta|^2}/\overline{|\alpha|^2} = 1/3$. The QED fidelity then can be calculated as $1 - (1 - 1/3) \times (M/2)p^N$, which gives

$$F_{\rm av}^{\rm qed} \approx \widetilde{F}_{\rm av}^{\rm qed} \approx 1 - M(t/MT_1)^N/3. \tag{3.20}$$

[If the above assumption $Nt/MT_1 \ll 1$ is violated, then the factor 1/3 changes, but the scaling remains the same.] We see that for this procedure the division into a larger number of cycles M is beneficial, as well as using more qubits (N) for the encoding. Note that our QED procedure does not prevent the relaxation events from happening, so the average probability of observing the "no error" result **0** in all M cycles is approximately $\exp(-tN/2T_1)$.

3.6 Summary

In this chapter we have analyzed the performance of N-qubit repetitive quantum codes in the presence of energy relaxation. As expected, these codes are not usable for quantum error correction. However, they can be used for quantum error detection. The best QED performance for weak energy relaxation is provided by the 3-qubit repetitive encoding [see Eq. (3.17) and Fig. 3.4(a)], while the 2-qubit encoding is sufficient and gives only slightly lower fidelity [see Eq. (3.9)]. We have found that the main con-

tribution to the QED infidelity for $N \geq 3$ comes from the non-unitary change of the quantum state in the case when no relaxation happens. Therefore, the QED infidelity can be strongly decreased if the QED algorithm is complemented with partial quantum measurement or, alternatively, if the protocol is divided into the even number of cycles and complemented with π-pulses in between (this resembles dynamical decoupling, though only superficially). In this case the fidelity improves with dividing the total duration into a larger number of cycles and using more qubits for the encoding [see Eq. (3.20)].

Note that the QED fidelity cannot be introduced in the usual way [as $F_\chi = \mathrm{Tr}(\chi_{\mathrm{desired}}\chi)$] via the process χ-matrix. In the analysis we have used the state fidelity, averaged over the Bloch sphere, with the usual conversion into F_χ via Eq. (1.11). For the state fidelity averaged with the weight proportional to the selection probability (denoted $\widetilde{F}_{\mathrm{av}}^{\mathrm{qed}}$) the usual trick of averaging over the 6 initial states can be used (see Appendix D), while for the state fidelity averaged with uniform weight (denoted $F_{\mathrm{av}}^{\mathrm{qed}}$) we had to average over the Bloch sphere explicitly, using Eqs. (C.3)–(C.11). In the analysis we used unraveling of the decoherence evolution into the "error scenarios", which is in general similar to the standard approach used in the quantum error correction, but is different in the way that each scenario describes a non-unitary process.

Chapter 4

Two-qubit error detection and correction for phase qubits

4.1 Introduction

In this chapter we propose and analyze two-qubit error detection/correction protocols designed for experimental implementation with the current technology of superconducting phase qubits (see Sec. 1.5). We will discuss several similar protocols (including a QED protocol for energy relaxation); for all of them the goal is to preserve an arbitrary initial state $|\psi_{\rm in}\rangle = \alpha|0\rangle + \beta|1\rangle$ of a qubit.

We focus on simple two-qubit QEC/QED protocols, somewhat similar to those in Ref. [54], which can be readily implemented using the present-day technology of phase qubits [44]. After a description of the ideal operation, realistic experimental parameters are used in the numerical simulation of these protocols. In the first protocol and its variations, we assume that as in most of the previous experiments [19, 20, 21, 22, 24, 25, 26, 27, 28, 29, 30] the errors are intentionally induced by particular operations pretended to be unknown. The algorithms can mainly be used for QED; however, when the type of

particular error is known (which is the case for intentional errors in an experiment), the algorithms can also be used for QEC. We also analyze numerically the operation of a protocol, in which the errors during a storage period are due to actual energy relaxation of two qubits (assuming storage in resonators of a RezQu-architecture device [44, 45] with phase qubits). This protocol can only be used in the QED mode. The main result of the simulations is that the analyzed protocols can be realized at the present-day level of phase qubit technology.

4.2 Two-qubit error detection and correction protocol

The first procedure (which we will mostly consider) is shown in Fig. 4.1; it is designed to preserve the state $|\psi_{\rm in}\rangle$ of the upper (main) qubit. Encoding is performed by preparing the lower (ancilla) qubit in the state $(|0\rangle + |1\rangle)/\sqrt{2}$ by starting with the ground state $|0\rangle$ and using the Y-rotation over the angle $\pi/2$ (denoted as $Y/2$), and then applying the controlled-Z (CZ) gate between the two qubits. [Note that the CZ gate is the natural entangling operation for the phase qubits [43, 44, 46].] This produces the entangled two-qubit wavefunction

$$[\alpha|0\rangle \otimes (|0\rangle + |1\rangle) + \beta|1\rangle \otimes (|0\rangle - |1\rangle)]/\sqrt{2}, \tag{4.1}$$

where the leftmost entry represents the main qubit. After encoding, the decoherence process is simulated by applying a unitary rotation to one of the qubits. For this encoding we consider a set of four possible rotations: $R_1^X(2\theta)$, $R_1^Y(2\theta)$, $R_2^Y(2\theta)$, and $R_2^Z(2\theta)$, where the subscript indicates the qubit number (1 for the main qubit), the superscript is the rotation axis on the Bloch sphere (see Sec. 1.5), and the argument 2θ is the rotation angle on the Bloch sphere (the corresponding rotation angle in the

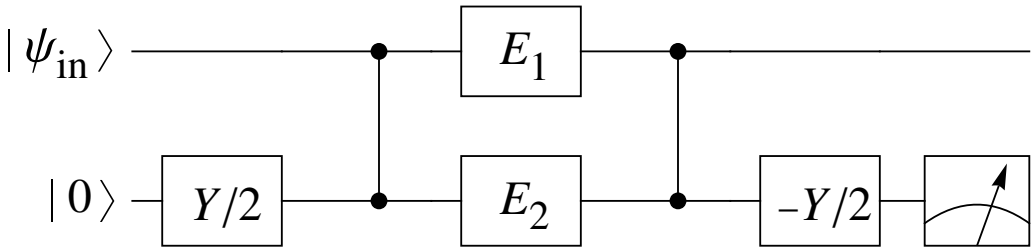

Figure 4.1: Two-qubit experimental protocol for realizing quantum error detection/correction. Notations E_1 and E_2 represent the four detectable error rotations: $R_1^X(2\theta)$, $R_1^Y(2\theta)$, $R_2^Y(2\theta)$, and $R_2^Z(2\theta)$. Notations $Y/2$ and $-Y/2$ represent $R^Y(\pi/2)$ and $R^Y(-\pi/2)$, respectively.

wavefunction language is θ).

After the error rotation has been applied, the resultant state is decoded by inverting the encoding operation and the ancilla qubit is measured in the computational basis. In the absence of error rotation, the state after decoding is $(\alpha|0\rangle + \beta|1\rangle) \otimes |0\rangle$, so that the initial state of the main qubit is restored and the measurement result for the ancilla qubit is 0. The error rotation disturbs the final state, which probabilistically changes the measurement result to 1 and also changes the final state of the main qubit.

4.3 Analysis of the ideal case

Let us start by analyzing the effect of the error rotation $R_1^X(2\theta)$ (X-rotation of the main qubit). It transforms the encoded state (4.1) into the state

$$\begin{aligned}&[\alpha(\cos\theta|0\rangle - i\sin\theta|1\rangle) \otimes (|0\rangle + |1\rangle)\\ &+\beta(-i\sin\theta|0\rangle + \cos\theta|1\rangle) \otimes (|0\rangle - |1\rangle)]/\sqrt{2},\end{aligned} \tag{4.2}$$

which after decoding (but before measurement) becomes

$$\cos\theta\,|\psi_{\text{in}}\rangle|0\rangle + i\sin\theta\,X|\psi_{\text{in}}\rangle|1\rangle, \tag{4.3}$$

where X is the Pauli-X-matrix transformation [7]. It is clear that we obtain ancilla measurement result 0 with probability $\cos^2\theta$, and then the state of the main qubit is restored to $|\psi_{\rm in}\rangle$, or obtain result 1 with probability $\sin^2\theta$, which leaves the main qubit in the state $X|\psi_{\rm in}\rangle$. [In this section we use the standard quantum computing notations [7](see also Sec. 1.2), in which the Pauli matrices act on column vectors with the upper element corresponding to the state $|0\rangle$. Note that for one-qubit wavefunctions $R^X(\pi) = -iX$.]

In quantum error detection we select only result 0, and this gives the perfect state preservation fidelity, $F_{\rm st}^{\rm qed} = 1$, for any initial state. We can also use the approach of quantum error correction and apply the X gate [i.e. $R^X(\pi)$] to the main qubit when the error result 1 is measured. This produces the initial state $|\psi_{\rm in}\rangle$ for both measurement results with perfect fidelity, $F_{\rm st}^{\rm qec} = 1$. Therefore, the QED and QEC fidelities averaged over the Bloch sphere are also perfect,

$$F_{\rm av}^{\rm qed} = F_{\rm av}^{\rm qec} = 1. \tag{4.4}$$

Notice, however, that for QEC we had to know that an error is due to the X-rotation applied to the first qubit. This is different from "real" error correction, in which we do not know the type of error, but is acceptable for a demonstration experiment.

Let us also calculate the storage fidelity if the measurement result is ignored (or, equivalently, the ancilla qubit is not measured). From Eq. (4.3) we obtain the state fidelity for the main qubit $F_{\rm st}^{\rm ign} = \cos^2\theta + \sin^2\theta\,\langle\psi_{\rm in}|X|\psi_{\rm in}\rangle^2$, which after averaging over the Bloch sphere becomes

$$F_{\rm av}^{\rm ign} = \cos^2\theta + (\sin^2\theta)/3. \tag{4.5}$$

Note that if the rotation $R^X(2\theta)$ is applied to a qubit without encoding, then the average fidelity is still given by Eq. (4.5), so the encoding with ignored measurement result (or

no measurement) does not affect the average preservation fidelity (moreover, it does not affect the state fidelity for any initial state).

Now let us analyze in a similar way the case when the error is introduced by the Y-rotation of the main qubit, $R_1^Y(2\theta)$. Then the two-qubit state before the measurement is

$$\cos\theta\,|\psi_{\rm in}\rangle|0\rangle + i\sin\theta\,Y|\psi_{\rm in}\rangle|1\rangle, \tag{4.6}$$

so that the measurement result 0 still restores the initial state $|\psi_{\rm in}\rangle$ of the main qubit, while for the measurement result 1 the state of the main qubit is $Y|\psi_{\rm in}\rangle$, thus requiring the Y-gate correction [i.e. $R^Y(\pi) = -iY$]. The QED and QEC fidelities are still perfect, Eq. (4.4), while the fidelity with ignored result is still given by Eq. (4.5). Note that the correcting Y-gate is different from the correcting X-gate in the previous case, so we need to know the type of the error to apply the proper correction (in a demonstration experiment the error rotation is applied intentionally, so its type is obviously known).

Now let us consider the error due to the Y-rotation of the ancilla qubit, $R_2^Y(2\theta)$. Then the state before the measurement is

$$\cos\theta|\psi_{\rm in}\rangle|0\rangle + \sin\theta Z|\psi_{\rm in}\rangle|1\rangle, \tag{4.7}$$

and therefore in the case of measurement result 1 the Z-gate correction is needed to restore $|\psi_{\rm in}\rangle$, while for the measurement result 0 no correction is needed. Equations (4.4) and (4.5) are still valid.

Finally, for the Z-rotation of the ancilla qubit, $R_2^Z(2\theta)$, the state before the measurement is

$$|\psi_{\rm in}\rangle(\cos\theta\,|0\rangle + i\sin\theta\,|1\rangle). \tag{4.8}$$

The final state of the main qubit is insensitive to this rotation, and therefore no correction is needed for both measurement results. In this case Eq. (4.4) is still valid, while

Eq. (4.5) is replaced by $F_{\rm av}^{\rm ign} = 1$.

We have discussed the effect of four error rotations: $R_1^X(2\theta)$, $R_1^Y(2\theta)$, $R_2^Y(2\theta)$, and $R_2^Z(2\theta)$. The two remaining rotations, $R_1^Z(2\theta)$ and $R_2^X(2\theta)$, gradually change the final state of the main qubit (both produce its Z-rotations) but always produce final state $|0\rangle$ of the ancilla qubit. Therefore, these errors are undetectable and are excluded from our set of error rotations.

As discussed above, for QEC we need to know which one out of four error types has been applied. In contrast, for QED we do not need to know the error type; for all of them the measurement result 0 indicates the perfect state of the main qubit. Moreover, for QED these types of error rotations can be applied simultaneously, as long as the rotation angles are relatively small, to make negligible the second-order terms (which in the QEC/QED language correspond to double-errors).

It is most natural to view the analyzed procedure as a QED protocol. However, we would like to emphasize that its interpretation as a QEC protocol is also possible: the proper correction is possible when we know which error process is applied. (In the existing QEC experiments the types of allowed errors are almost always limited; in our protocol the number of allowed types is further reduced to one out of four.) Most importantly, our simple two-qubit protocol demonstrates the main "miracle" of QEC, that continuous quantum errors can be transformed into discrete errors, and then corrected.

4.4 Realization using phase qubits

So far we considered the ideal case when there is no physical decoherence of qubits, and the loss of fidelity is only due to intentional rotations of the qubit states. In

this section we discuss a more realistic experimental situation, with added decoherence during the protocol. We will have in mind the present-day technology of superconducting phase qubits [43, 44, 46].

Note that the phase qubit technology provides a high-fidelity measurement (about 95% [43], so we consider it perfect in the simulations); however, it takes a significant time to read out the measurement result (longer than the qubit decoherence time). While this is not a problem for the QED, the QEC at present cannot be done in real time. Nevertheless, there is a simple way to go around this difficulty in an experiment. The resulting state of the main qubit is measured by using the quantum state tomography (QST), so the experiment is necessarily repeated many times. It is easy to separate the QST data for ancilla measurement results 0 and 1. In this way two different density matrices of the main qubit are obtained for ancilla measurement 0 and 1. For the result 1 it is then easy to calculate the density matrix after the correcting operation (if it were applied in real time). Finally adding the two density matrices (with weights equal to the probabilities of ancilla measurement results), the qubit density matrix for the QEC procedure is obtained.

Recall from Sec. 1.5 that in phase qubits [43, 44, 46] the main sources of decoherence are single-qubit energy relaxation (with T_1 on the order of 0.5 μs) and pure dephasing (with a comparable or a little shorter dephasing time T_φ). The decoherence is somewhat reduced in the RezQu architecture [44, 45], in which the quantum information is often transferred between the phase qubits and resonators (resonators have much longer T_1 and practically no pure dephasing). We have simulated the procedure of Fig. 4 in a simplified way, which does not explicitly reproduce the RezQu implementation of the protocol, but still uses a reasonable account of realistic decoherence.

For simplicity for each qubit we assume $T_1 = T_2$ (so that the pure dephasing

time is $T_\varphi = 2T_1$). We assume that single-qubit rotations [including $R^Y(\pm\pi/2)$ of ancilla qubit, preparation of the main qubit, and error rotations] take 10 ns each, CZ gates take 40 ns each, and there are 5 ns spacings between the operations. Then the whole protocol of Fig. 4 (ending before measurement of ancilla qubit and tomography of the main qubit) takes 135 ns. We calculate the evolution of the two-qubit density matrix by breaking the procedure into small time steps and applying energy relaxation and pure dephasing to each qubit (for simplicity the CZ gate is simulated as a gradual accumulation of the phase, as would be for the dispersive gate). We start with 6 initial states of the main qubit [$|0\rangle$, $|1\rangle$, $(|0\rangle \pm |1\rangle)/\sqrt{2}$, $(|0\rangle \pm i|1\rangle)/\sqrt{2}$, labeled by index $j = 1, \ldots 6$ below], and from the final two-qubit density matrices we calculate reduced unnormalized one-qubit density matrices $\rho_{0,j}$ and $\rho_{1,j}$, corresponding to ancilla measurement results 0 and 1 (the probabilities of these results are then $\mathrm{Tr}\rho_{0,j}$ and $\mathrm{Tr}\rho_{1,j}$). The averaged preservation fidelity with ignored measurement results is then (see Appendix D) $F_{\mathrm{av}}^{\mathrm{ign}} = (1/6)\sum_j \mathrm{Tr}[(\rho_{0,j} + \rho_{1,j})\rho_j^{\mathrm{in}}]$, where $\rho_j^{\mathrm{in}} = |\psi_j\rangle\langle\psi_j|$ is the unchanged initial state. The averaged (weighted) QED fidelity is then $\widetilde{F}_{\mathrm{av}}^{\mathrm{qed}} = \sum_j \mathrm{Tr}(\rho_{0,j}\rho_j^{\mathrm{ideal}})/\sum_j \mathrm{Tr}\rho_{0,j}$, and the QEC fidelity is $F_{\mathrm{av}}^{\mathrm{qec}} = (1/6)\sum_j \mathrm{Tr}[(\rho_{0,j} + \rho_{1,j}^{\mathrm{corr}})\rho_j^{\mathrm{in}}]$, where the corrected density matrix $\rho_{1,j}^{\mathrm{corr}}$ is obtained from $\rho_{1,j}$ by applying the ideal correcting operations (X, Y, Z, I) discussed in the previous section.

Figure 4.2 shows the average fidelities $\widetilde{F}_{\mathrm{av}}^{\mathrm{qed}}$ (solid lines), $F_{\mathrm{av}}^{\mathrm{qec}}$ (dotted lines), and $F_{\mathrm{av}}^{\mathrm{ign}}$ (dashed lines), as functions of the rotation angle 2θ (in units of π) for the intentional X-rotation of the main qubit, $R_1^X(2\theta)$. The three sets of lines are for three values of $T_1 = T_2$: 300 ns, 500 ns, and 700 ns. Note that we present the average fidelities F_{av}, but they can be easily converted into the process matrix fidelities F_χ via Eq. (1.11). Also note that the range from 1/3 to 1 for F_{av} (used for the vertical axis in Fig. 4.2)

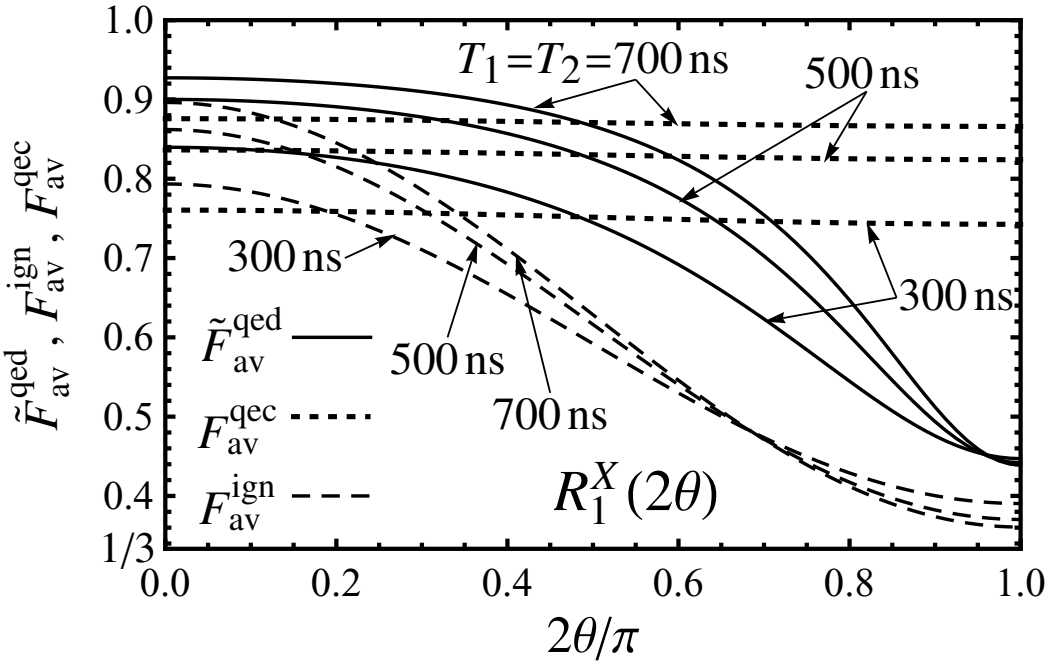

Figure 4.2: Numerical results for the average QED fidelity $\widetilde{F}_{\rm av}^{\rm qed}$ (solid lines), the QEC fidelity $F_{\rm av}^{\rm qec}$ (dotted lines), and the fidelity $F_{\rm av}^{\rm ign}$ with ignored ancilla measurement results (dashed lines), as functions of the angle 2θ of intentional X-rotation of the main qubit, $R_1^X(2\theta)$. The simulated protocol of Fig. 4.1 has a duration of 135 ns. We assume qubits with $T_1 = T_2 = 300$ ns, 500 ns, and 700 ns.

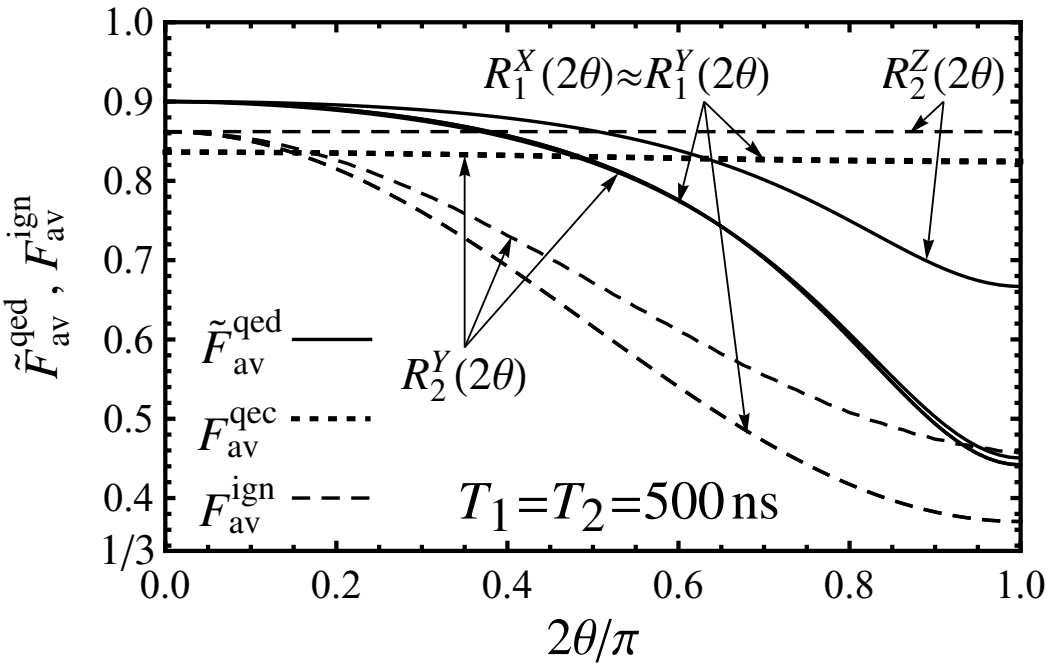

Figure 4.3: Same as in Fig. 4.2, but for four types of intentional qubit state rotations: $R_1^X(2\theta)$, $R_1^Y(2\theta)$, $R_2^Y(2\theta)$, and $R_2^Z(2\theta)$. Qubits with $T_1 = T_2 = 500$ ns are assumed. Results for rotations $R_1^X(2\theta)$ and $R_1^Y(2\theta)$ practically coincide.

corresponds to the range from 0 to 1 for F_χ.

From Fig. 4.2 we see that even for $T_1 = T_2 = 300$ ns the QED fidelity is significantly higher than the fidelity with ignored measurement result (recall that the procedure duration is 135 ns). The difference between $\widetilde{F}_{\rm av}^{\rm qed}$ and $F_{\rm av}^{\rm ign}$ becomes larger for longer decoherence time (500 ns and 700 ns). The QEC fidelity is below the QED fidelity (and even below $F_{\rm av}^{\rm ign}$) for small θ, but becomes above $\widetilde{F}_{\rm av}^{\rm qed}$ and $F_{\rm av}^{\rm ign}$ at large θ.

It is interesting to notice that $F_{\rm av}^{\rm ign}$ at $2\theta \approx \pi$ is much closer to the ideal value 1/3 [see Eq. (4.5)] than to the ideal value 1 at $2\theta \approx 0$. This property can be understood using the equivalent language of the process fidelity $F_\chi = {\rm Tr}(\chi_{\rm desired}\chi)$ – see Eq. (1.11). Since the desired operation is the absence of evolution, $F_\chi = \chi_{II}$ in the standard notations for the one-qubit 4×4 matrix χ [7, 25, 46, 44]; note that $\chi_{II} + \chi_{XX} + \chi_{YY} + \chi_{ZZ} = 1$. Ideally $\chi_{II} = 1$ for $2\theta = 0$ and $\chi_{XX} = 1$ for $2\theta = \pi$.

Since decoherence spreads these ideal unity values to the three other diagonal elements of χ, we would expect that $F_\chi^{\rm ign}$ at $2\theta = \pi$ should be (very crudely) three times less than $1 - F_\chi^{\rm ign}$ at $2\theta = 0$. This roughly corresponds to what we see in Fig. 4.2.

Figure 4.2 shows the results only for the X-rotation of the main qubit, $R_1^X(2\theta)$. The results for all four considered rotations, $R_1^X(2\theta)$, $R_1^Y(2\theta)$, $R_2^Y(2\theta)$ and $R_2^Z(2\theta)$, are shown in Fig. 4.3 for $T_1 = T_2 = 500$ ns. The results for X and Y-rotation of the main qubit are practically indistinguishable from each other. The QED and QEC fidelities for Y-rotation of the ancilla qubit are very close to the corresponding fidelities for the rotation of the main qubit. For Z-rotation of the ancilla qubit the operation with ignored measurement coincides with the QEC operation (because no correction is applied for measurement result 1), and the QED fidelity $\widetilde{F}_{\rm av}^{\rm qed}$ is higher than $F_{\rm av}^{\rm ign} = F_{\rm av}^{\rm qec}$ only at $2\theta \lesssim \pi/2$, and only by a small amount. Obviously, the rotation $R_2^Z(2\theta)$ is not good for demonstrating an advantage of this encoding, in contrast to other rotations.

Overall, from Figs. 4.2 and 4.3 we see that the current technology of phase qubits is good enough for demonstrating the operation of the considered two-qubit QED/QEC protocol. In an experiment, the larger value of the QED fidelity in comparison with the case of ignored measurement result is the demonstration that the QED procedure is beneficial. Similarly, the QEC operation can also be demonstrated (though with the caveat discussed in the previous sections).

4.5 Related protocols

The protocol of Fig. 4.1 can be easily modified to change the set of four detectable/correctable error operations. For example, if we desire protection from Y and Z rotations of both qubits [i.e. $R_1^Y(2\theta)$, $R_1^Z(2\theta)$, $R_2^Y(2\theta)$, and $R_2^Z(2\theta)$], we can add $\pm\pi/2$

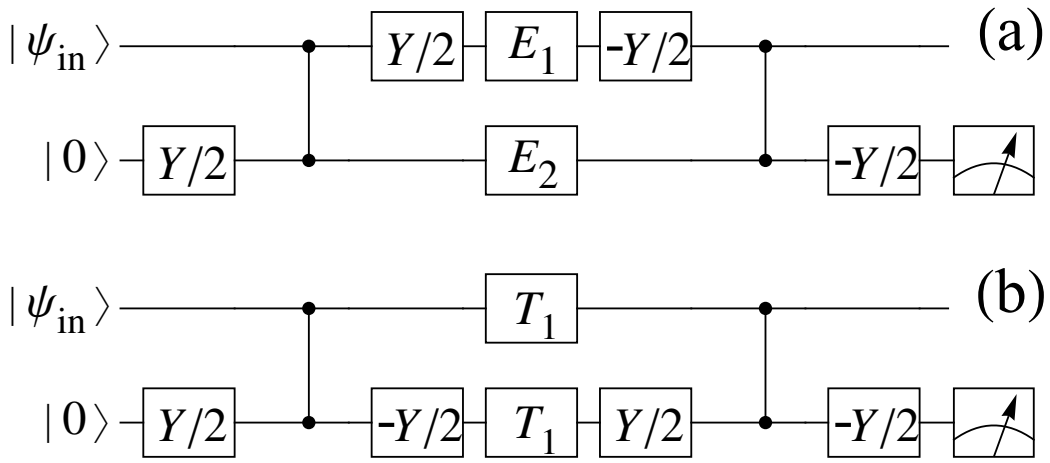

Figure 4.4: Modified two-qubit QED/QEC algorithms. The protocol shown in (a) detects/corrects errors due to rotations R_1^Y, R_1^Z, R_2^Y, and R_2^Z; it can be used to protect from natural pure dephasing of the qubits. The protocol in (b) is designed for error rotations R_1^X, R_1^Y, R_2^X, and R_2^Y. Therefore, it can be used as a QED procedure for errors due to energy relaxation of both qubits (stored in resonators).

Y-rotations of the main qubit before and after the error rotations – see Fig. 4.4(a). Such encoding also protects from natural pure dephasing of both qubits.

For protection from X and Y rotations of both qubits [i.e. $R_1^X(2\theta)$, $R_1^Y(2\theta)$, $R_2^X(2\theta)$, and $R_2^Y(2\theta)$], we can add $\mp\pi/2$ Y-rotations of the ancilla qubit before and after the errors – see Fig. 4.4(b). Such encoding can be used in the QED mode for the energy relaxation of both qubits. (This procedure essentially realizes the idea of Fig. 3.1 for two qubits; the only difference is the encoding $\alpha|00\rangle - \beta|11\rangle$ instead of encoding $\alpha|00\rangle + \beta|11\rangle$ considered in Sec. 4.3.)

In the RezQu architecture based on phase qubits [44, 45], the protocol of Fig. 4.4(b) can be efficiently used for storing the information in the resonators. We have simulated the operation of this protocol, assuming that the encoding/decoding is done with the phase qubits having relaxation times $T_1 = T_2$, while in between encoding and decoding the information is moved to resonators for a relatively long storage. The

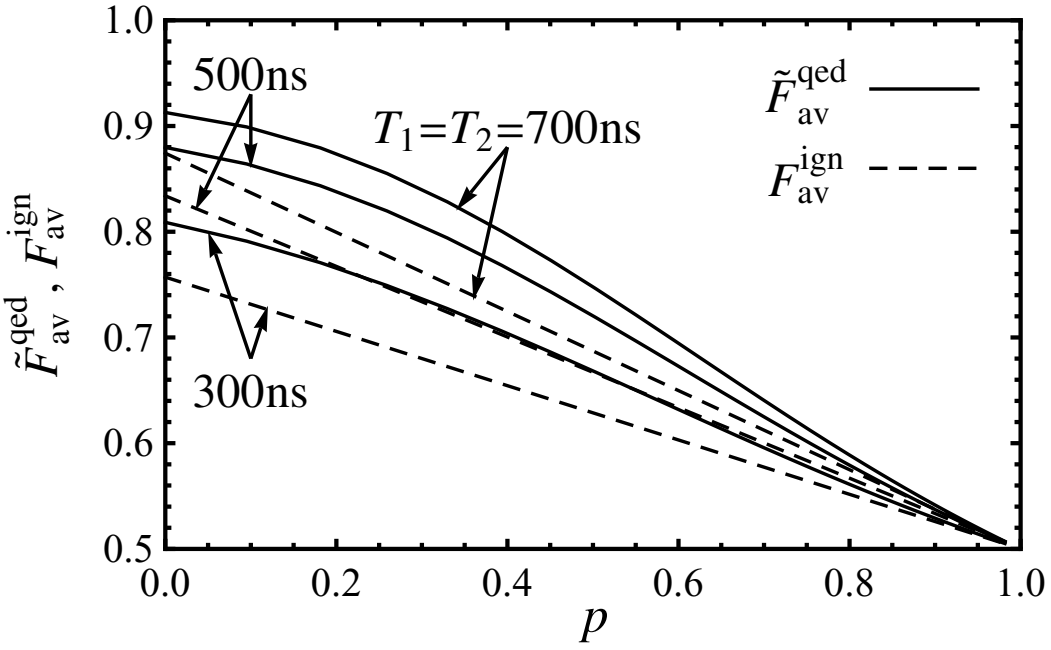

Figure 4.5: Average QED fidelity $\widetilde{F}_{\rm av}^{\rm qed}$ (solid lines) for the two-qubit protocol of Fig. 4.4(b), as a function of the single-qubit energy relaxation probability $p = 1 - \exp(-t_{\rm storage}/T_1^{\rm resonator})$ during information storage in resonators. Dashed lines show average fidelity $F_{\rm av}^{\rm ign}$ when the measurement result is ignored. The encoding/decoding is done with phase qubits having significantly shorter relaxation times $T_1 = T_2$ (300 ns, 500 ns, and 700 ns); the assumed duration of the procedure (excluding storage time) is 155 ns.

procedure (without the storage time) is slightly longer than what was considered in the previous subsection: 155 ns instead of 135 ns (we still do not simulate explicitly the move operations between the qubits and resonators). Solid lines in Fig. 4.5 show the corresponding QED fidelities $\widetilde{F}_{\rm av}^{\rm qed}$ as functions of the single-qubit energy relaxation probability $p = 1 - \exp(-t_{\rm storage}/T_1^{\rm resonator})$ during the storage (in experiment [44] $T_1^{\rm resonator} \gg T_1$, though our results do not need this assumption). The QEC operation is impossible in this case (for real energy relaxation in resonators); however, as seen from Fig. 4.5, the QED operation can be reliably demonstrated experimentally.

4.6 Summary

In this chapter we have considered simple two-qubit protocols of quantum error detecton/correction, suitable for present-day experiments with superconducting phase qubits [44]. In the protocol of Fig. 4.1 the errors are simulated by intentional unitary rotations of the qubit states (two types of rotations for each qubit). In this case not only the QED, but also the QEC operation is possible if we know the applied type of error rotation. Most importantly, this experiment would demonstrate the QEC "miracle" of converting continuous quantum errors into discrete errors, which are then correctable. The numerical simulations (Figs. 4.2 and 4.3) with account of decoherence during the protocol show that the experimental QED and QEC fidelities are expected to be significantly higher than the fidelity with ignored result of the ancilla qubit measurement. Therefore, the QED and QEC benefits can be demonstrated experimentally.

A slightly different protocol, shown in Fig. 4.4(b), can be used as a QED procedure for errors due to natural energy relaxation of qubits stored in resonators of a RezQu-architecture device [44, 45] based on phase qubits. The numerical simulations

(Fig. 4.5) show that such experiment can also be realized with the present-day technology, demonstrating the benefits of encoding a logical qubit in several (two in this case) physical qubits. While the measurement-free QEC experiment has been recently realized with superconducting transmon qubits [30], the experiments proposed and analyzed in this chapter would be the first measurement-based QED/QEC protocols realized with superconducting qubits.

Chapter 5

Quantum Information Transfer

5.1 Introduction

In this chapter we investigate a recently proposed procedure [8] for transferring the state of a microwave qubit from one resonator to another resonator via a superconducting transmission line with nearly perfect efficiency using tunable couplers. The original proposal shows that in principle the use of two tunable couplers, instead of just one [61], should make an experimental demonstration possible with current superconducting technology. The details of the ideal procedure will be introduced in Sec. 5.2. In Sec. 5.3 we consider procedural errors due to deviations from the ideal transfer protocol, including timing errors, maximum coupling strength, and imperfect control. In Sec. 5.4 we study the effect of a mismatch of the emitting and receiving resonator frequencies. The procedure is shown to be robust against all considered errors except the resonator frequency mismatch, which will require active compensation during experimental implementation.

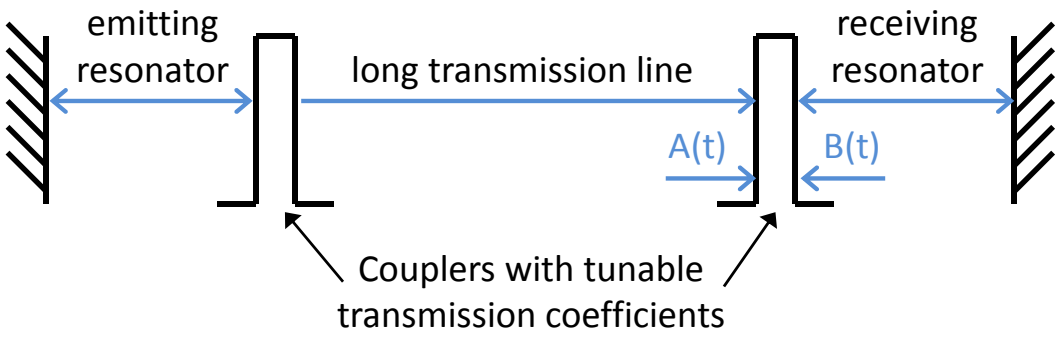

Figure 5.1: The physical system used for the microwave qubit transfer protocol. Two resonators are connected to the ends of a transmission line by tunable couplers. We consider the transfer of a classical field, initially in the emitting resonator, which is sent to the receiving resonator. [In our case the state of the microwave qubit can be treated as a classical field.] The fields in the transmission line $[A(t)]$ and in the receiving resonator $[B(t)]$ are shown along with their respective directions.

5.2 Ideal procedure

The physical system used for the qubit transfer is shown in Fig. 5.1. Two resonators are connected to the ends of a transmission line by the previously demonstrated tunable inductive couplers of Ref. [62]. The microwave qubit can be treated as a classical field [61], we therefore consider transfer of the field amplitudes labeled $A(t)$ and $B(t)$ in the figure.

Notice that the use of the scattering matrix is the same for quantum mechanics and microwave physics. In general the scattering matrix can be written as

$$S = \begin{pmatrix} r_1 & tR_1/R_2 \\ t & r_2 \end{pmatrix}, \quad |t_1|^2 R_1/R_2 + |r_1|^2 = 1, \tag{5.1}$$

where r_1 and t are the reflection and transmission coefficients for a wave incident from the left, R_1 and R_2 are the wave impedances of the material on the left side (subscript 1) and right side (subscript 2) of the coupler, $r_2 = -r_1^* t/t^*$ is the reflection coefficient for a wave incident from the right, and the energy conservation can be written as $|t|^2 R_1/R_2 + |r|^2 = 1$. The time dependence of the field $B(t)$ in Fig. 5.1 can be written as a differential

equation in terms of the reflection (from the left) and transmission coefficients of the receiving resonator as

$$\dot{B} = -\frac{r_{\mathrm{rec}}\,\mathrm{e}^{\mathrm{i}\phi} - 1}{\tau_{rt}} B + \frac{t_{\mathrm{rec}}\,\mathrm{e}^{\mathrm{i}\phi}}{\tau_{rt}} A, \tag{5.2}$$

where τ_{rt} is the round-trip time of the resonator and ϕ describes the deviation of the effective resonator length from the perfect value. For the lowest frequency mode, $\tau_{rt} = 2\pi/\omega$ for a $\lambda/2$ (half-wavelength) resonator or $\tau_{rt} = \pi/\omega$ for a $\lambda/4$ (quarter-wavelength) resonator.

The transfer protocol is illustrated in Fig. 5.2. In order to transfer the state of a microwave qubit between two resonators the transmission coefficients of the tunable couplers are varied in time such that back-reflection into the transmission line is nulled at the receiving resonator. In the first half of the procedure the emitting coupler is slowly opened to its maximum value while the receiving coupler is kept maximally transparent. In the second half of the procedure the emitting coupler is kept maximum and the receiving coupler is slowly closed. There is some energy lost since the perfect cancelation of back-reflection cannot be accomplished until a sufficient amplitude is present in the receiving resonator. This has been treated analytically in the original paper. Also previously treated is the energy lost from the incomplete transfer due to the necessarily finite duration of any experimental procedure. The effect of these errors will be seen in the next section as the inefficiency of the procedure without any deviation from the ideal parameters.

The transfer efficiency η is defined as the ratio of the energy in the receiving resonator to the initial energy stored in the emitting resonator $\eta = E_{\mathrm{rec}}/E_{\mathrm{em}}$ (as was done in the original paper [8]). In simulations the final energy of the receiving resonator is calculated as the square of the field amplitude given by the solution of Eq. (5.2). In the

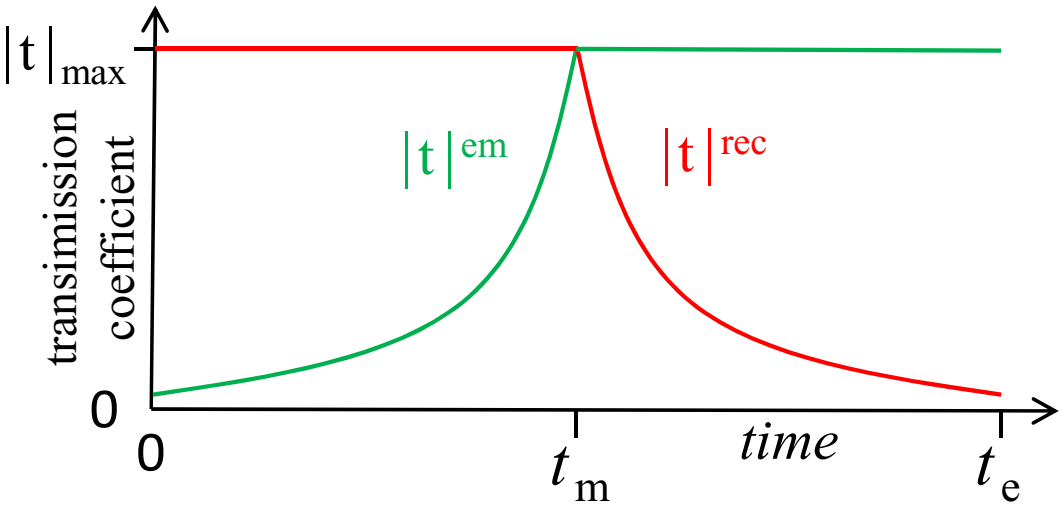

Figure 5.2: In order to transfer the state of a microwave qubit between two resonators the transmission coefficients of the tunable couplers are varied in time such that back-reflection into the transmission line is nulled at the receiving resonator. In the first half of the procedure the emitting coupler is slowly opened to its maximum value while the receiving coupler is kept maximally transparent. In the second half of the procedure the emitting coupler is kept maximum and the receiving coupler is slowly closed.

ideal procedure, a desired efficiency is achieved by using specific procedural parameters. In our simulations we choose (design) the parameters of the transfer protocol for various desired efficiencies ($\eta_{\text{design}} = 0.9,\ 0.99,$ and 0.999) and investigate the efficiency loss caused by deviations from these ideal parameters.

The ideal time dependence of the transmission coefficients is shown in Fig. 5.2. During the first half of the procedure, the transmission coefficient of the emitting coupler should be

$$t^{\text{em}} = \frac{t^{\text{em}}_{\text{max}}\sqrt{\tau^{\text{em}}_{\text{bu}}/\tau^{\text{rec}}_{\text{bu}}}}{\sqrt{\left(1+\frac{\tau^{\text{em}}_{\text{bu}}}{\tau^{\text{rec}}_{\text{bu}}}\right)\mathrm{e}^{(t_{\text{m}}-t)/\tau^{\text{em}}_{\text{bu}}}-1}},\quad 0<t<t_{\text{m}} \tag{5.3}$$

where $t^{\text{em}}_{\text{max}}$ is the maximum value of the transmission coefficient for the emitting coupler, $\tau^{\text{em}}_{\text{bu}}$ and $\tau^{\text{rec}}_{\text{bu}}$ are the buildup times for the emitting and receiving resonators, and t_m is the time that the emitting coupler reaches its maximum value. After t_{m} the emitting coupler is kept at its maximum value for the remainder of the procedure

$$t^{\text{em}} = t^{\text{em}}_{\text{max}},\quad t_{\text{m}}<t<t_{\text{e}}. \tag{5.4}$$

The transmission coefficient of the receiving coupler should be controlled in a similar (but reversed) way. During the first half of the procedure ($t < t_{\mathrm{m}}$) it should be kept maximum $t^{\mathrm{em}} = t^{\mathrm{em}}_{\mathrm{max}}$, and then closed as

$$t^{\mathrm{rec}} = \frac{t^{\mathrm{rec}}_{\mathrm{max}} \sqrt{\tau^{\mathrm{rec}}_{\mathrm{bu}} / \tau^{\mathrm{em}}_{\mathrm{bu}}}}{\sqrt{\left(1 + \frac{\tau^{\mathrm{rec}}_{\mathrm{bu}}}{\tau^{\mathrm{em}}_{\mathrm{bu}}}\right) \mathrm{e}^{(t-t_{\mathrm{m}})/\tau^{\mathrm{rec}}_{\mathrm{bu}}} - 1}}, \quad t_{\mathrm{m}} < t < t_{\mathrm{e}}. \tag{5.5}$$

As was mentioned above, the parameters of the procedure are chosen to achieve a desired transfer efficiency. In this chapter we simulate the protocol and calculate the transfer efficiency when the parameters are non-ideal. To separate the effect of each possible error, we vary just one parameter from its ideal value at a time. For simulations we assume both resonators are quarter-wavelength ($\lambda/4$) with a frequency of $f = 6$ GHz and the tunable couplers have a maximum possible transmission coefficient of $t_{\mathrm{max}} = 0.05$. Other necessary parameters are calculated using the following relations [8]:

$$\tau_{\mathrm{rt}} = \frac{1}{2f}, \quad \tau_{\mathrm{bu}} = \frac{\tau_{\mathrm{rt}}}{|t_{\mathrm{max}}|^2}, \quad t_{\mathrm{m}} = \tau_{\mathrm{bu}} \ln\left(\frac{1}{1 - \eta_{\mathrm{design}}}\right), \quad t_{\mathrm{e}} = 2t_{\mathrm{m}}. \tag{5.6}$$

Notice that the procedure duration ($2t_{\mathrm{m}}$ or t_{e}) is determined by the desired efficiency η_{design}.

5.3 Procedural errors

In this section we investigate the effect of deviations from the ideal time dependencies for the emitting and receiving couplers. These procedural errors will necessarily be present in any experiment due to hardware limitations. We show that the procedure is robust to these errors (even relatively large deviations from the ideal procedure will not drastically decrease the efficiency). In this section we assume that the resonators

are identical, and we replace Eqs. (5.3)-(5.5) with imperfect shapes

$$t^{\mathrm{em}} = \frac{T_1\sqrt{\tau_1/\tau_2}}{\sqrt{\left(1+\frac{\tau_1}{\tau_2}\right)\mathrm{e}^{(t_1-t)/\tau_1}-1}}, \;\; 0<t<t_1, \tag{5.7}$$

$$t^{\mathrm{rec}} = \frac{T_2\sqrt{\tau_2/\tau_1}}{\sqrt{\left(1+\frac{\tau_2}{\tau_1}\right)\mathrm{e}^{(t-t_2)/\tau_2}-1}}, \;\; t_2<t<t_{\mathrm{e}}, \tag{5.8}$$

where t_i is the switching time, T_i is the maximum value of the transmission coefficient, and τ_i is the shaping parameter for the emitting ($i = 1$) and receiving ($i = 2$) resonators.

For the ideal procedure $t_1 = t_2 = t_{\mathrm{m}}$, $\tau_1 = \tau_{\mathrm{bu}}^{\mathrm{rec}}$, and $\tau_2 = \tau_{\mathrm{bu}}^{\mathrm{em}}$, but in this section we simulate a procedural error by allowing these parameters to independently deviate from their ideal values. To simulate a procedure, we solve Eq. (5.2) (with $\phi = 0$) in the high-Q limit $\mathrm{Re}(1-r_2) \approx 1-|r_2| \approx |t|^2/2$, and a similar equation for the field in the transmission line A

$$\dot{A} = -\frac{|t^{\mathrm{em}}|^2}{2\tau_{rt}}A. \tag{5.9}$$

The differential equations in Eqs. (5.2) and (5.9) are in general not analytically solvable – we used the standard fourth-order Runge-Kutta method to find numerical solutions for a given set of parameters.

First we look at the effect of an imperfect switching time for the emitting coupler, t_1 in Eq. (5.8). The transfer efficiency η is shown as a function of switching time in Fig. 5.3. The two sets of lines correspond to two desired efficiencies $\eta_{\mathrm{design}} = 0.99$ and 0.999, which correspond to the ideal switching times $t_{\mathrm{m}}^{\mathrm{ideal}} \approx 154$ ns and 230 ns. The relative switching error on the horizontal axes is used because the different desired efficiencies require different durations (i.e. different t_{m}). Solid lines show the efficiency when the switching time of the receiving resonator is kept constant ($t_2 = t_{\mathrm{m}}$) and the other is varied ($t_1 = t_{\mathrm{m}} + \delta t$). Dashed lines show the efficiency when both switching times differ from the ideal value by the same factor $t_1 = t_2 = t_{\mathrm{m}} + \delta t$. In both cases the

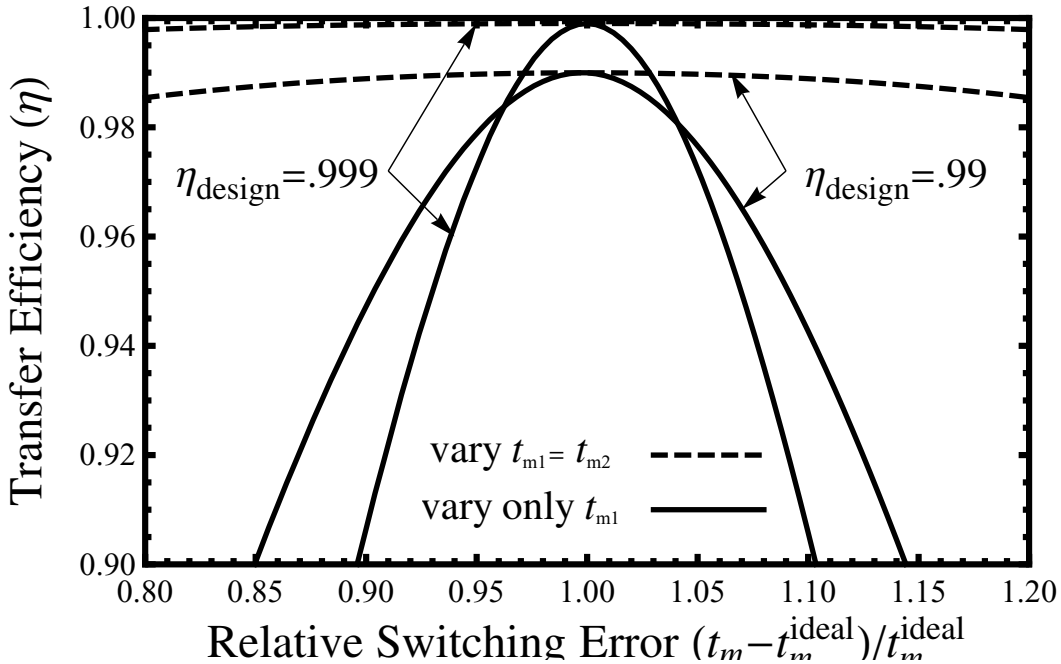

Figure 5.3: Efficiency of the transfer procedure with an error in the switching time. The two sets of lines correspond to the desired efficiencies $\eta_{\text{design}} = 0.999$ and 0.99, which correspond to the ideal switching times $t_{\text{m}}^{\text{ideal}} \approx 154$ ns and 230 ns. Solid lines show the efficiency when the switching time of the receiving resonator is kept constant ($t_2 = t_{\text{m}}$) and the other is varied ($t_1 = t_{\text{m}} + \delta t$). Dashed lines show the efficiency when both switching times differ from the ideal value by the same factor $t_1 = t_2 = t_{\text{m}} + \delta t$. In both cases the horizontal axis corresponds to $\delta t/t_{\text{m}}$.

horizontal axis corresponds to $(\delta t - t_{\text{m}})/t_{\text{m}}$. Clearly the absolute timing error illustrated by the dashed lines is not a hindrance for experimental implementation (this is equivalent to changing the duration, which by design will change the maximum efficiency possible). Even for the relative error (solid lines) a large deviation $\delta t = \pm 0.05\, t_{\text{m}}$ corresponds to an efficiency loss of only $(\eta_{\text{ideal}} - \eta)/\eta_{\text{ideal}} \sim 2\%$. A $\pm 5\%$ error in timing should be easy to achieve and will not be a limiting factor in realizing the flying microwave qubit using this procedure.

The next error we consider is the shaping of the transmission coefficients' time dependence (ideally $\tau_{\text{bu}}^{em} = \tau_{\text{bu}}^{rec} = 33\frac{1}{3}$ ns). This is simulated by varying the value of τ_1 and τ_2 in Eqs. (5.7) and (5.8). This method of varying the shaping was chosen for

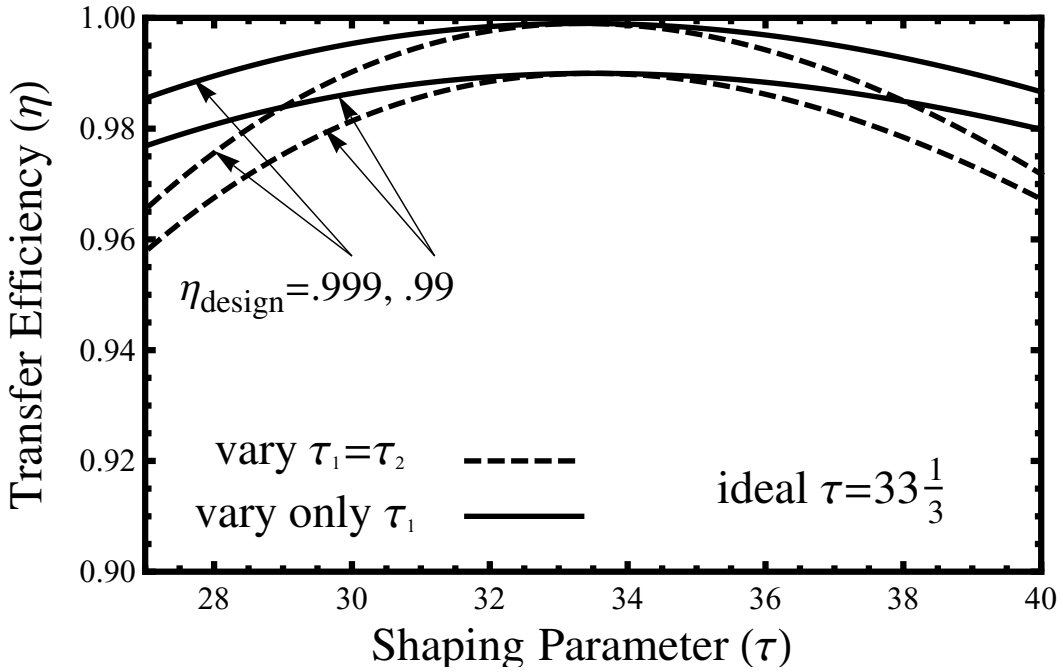

Figure 5.4: Efficiency of the transfer procedure with an error in the shaping parameter (ideally $\tau_{\rm bu}^{em} = \tau_{\rm bu}^{rec} = 33\frac{1}{3}$ ns). The two sets of lines correspond to the desired efficiencies $\eta_{\rm design} = 0.999$ and 0.99. Solid lines are when τ_1 is fixed to its ideal value $\tau_1 = \tau_{\rm bu}^{\rm em}$ and $\tau_2 = \tau_{\rm bu}^{\rm rec} + \delta\tau = \tau$ is varied. Dashed lines show the transfer efficiency when the shaping parameters are equal and both deviate from the ideal value $\tau_1 = \tau_2 = \tau_{\rm bu}^{\rm rec} + \delta\tau = \tau$. In both cases the horizontal axis is given by τ.

its relative simplicity (the single parameter τ can move the shape between a sharp step function and triangular ramp). The transfer efficiency as a function of switching time is shown in Fig. 5.4. Solid lines show the efficiency when τ_1 is fixed to its ideal value $\tau_1 = \tau_{\rm bu}^{\rm em}$ and $\tau_2 = \tau_{\rm bu}^{\rm rec} + \delta\tau = \tau$ is varied. Dashed lines show the efficiency when the shaping parameters are equal and both deviate from the ideal value $\tau_1 = \tau_2 = \tau_{\rm bu}^{\rm rec} + \delta\tau = \tau$. In both cases the horizontal axis is given by τ. For both errors the decrease of efficiency is small ($< 2\%$) for a reasonably large deviation of $(\tau - \tau_{\rm bu}^{\rm rec})/\tau_{\rm bu}^{\rm rec} \sim \pm 8\%$.

Next we consider errors in the maximum value of the transmission coefficient. This is simulated by varying the value of T_1 and T_2 in Eqs. (5.7) and (5.8). The transfer efficiency as a function of the maximum transmission coefficient is shown in Fig. 5.5. Solid lines show the efficiency when T_1 is fixed to its ideal value $T_1 = t_{\rm max}^{\rm rec}$

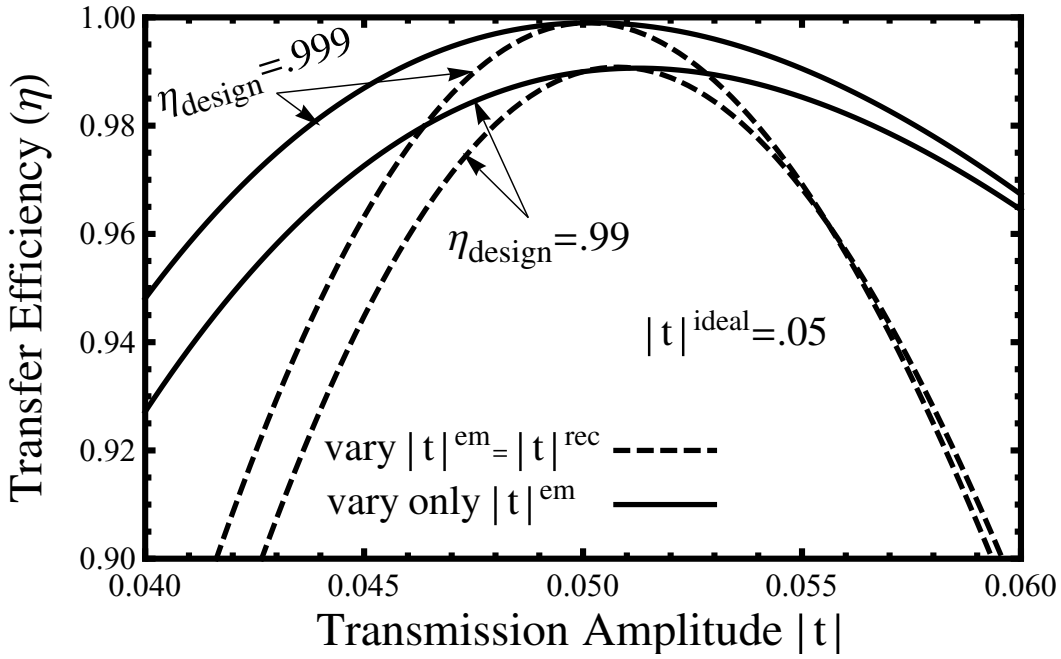

Figure 5.5: Efficiency of the transfer procedure with an error in the maximum value of the transmission coefficient. The two sets of lines correspond to the desired efficiencies $\eta_{\text{design}} = 0.999$ and 0.99. Solid lines are when T_1 is fixed to its ideal value $T_1 = t_{\text{max}}^{\text{rec}}$ and $T_2 = t_{\text{max}}^{\text{rec}} + \delta T = T$ is varied. Dashed lines show the transfer efficiency when the shaping parameters are equal and both deviate from the ideal value $T_1 = T_2 = t_{\text{max}}^{\text{rec}} + \delta T = T$. In both cases the horizontal axis is given by T.

and $T_2 = t_{\text{max}}^{\text{rec}} + \delta T = T$ is varied. Dashed lines show the efficiency when the shaping parameters are equal and both deviate from the ideal value $T_1 = T_2 = t_{\text{max}}^{\text{rec}} + \delta T = T$. In both cases the horizontal axis is given by T. For both errors the decrease of efficiency is small ($< 2\%$) for a reasonably large deviation of $(T - t_{\text{max}}^{\text{rec}})/t_{\text{max}}^{\text{rec}} \sim \pm 5\%$.

5.4 Frequency difference

In both the analytical treatment of the original proposal and our analysis so far, we have assumed that the emitting and receiving resonators have equal and constant frequencies during the transfer. In this chapter we relax this assumption and investigate the effect of unequal, but still constant, frequencies. In general, varying the transmission

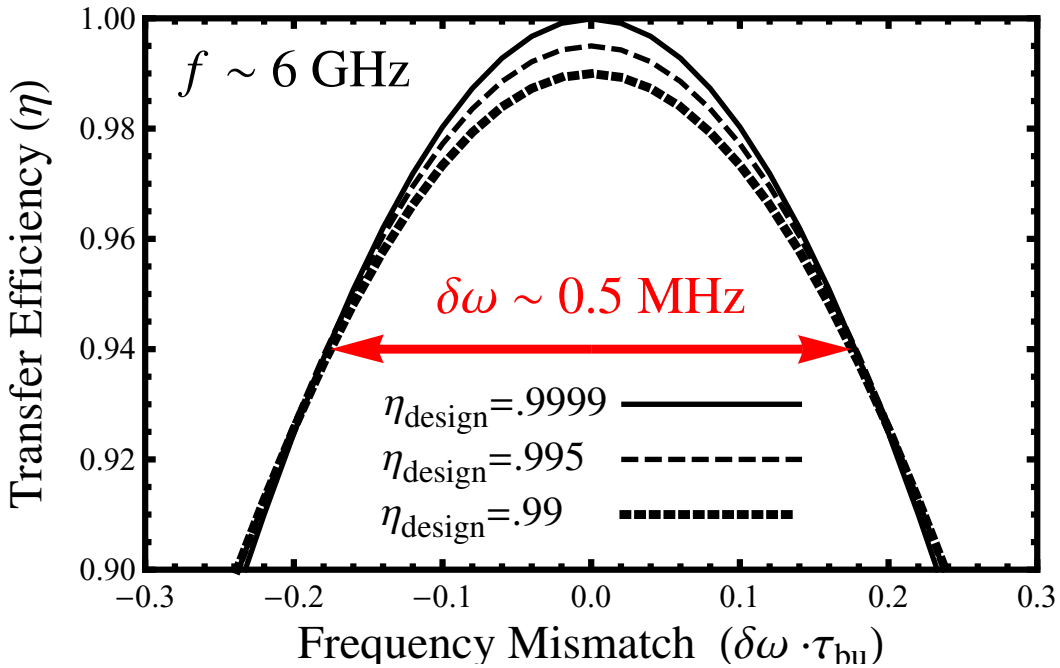

Figure 5.6: Efficiency of the transfer procedure between two resonators with different frequencies. The graph shows the results for a procedure designed to achieve $\eta = 0.9999$ (Solid line), 0.995 (Dashed line), and 0.99 (Dotted line). Notice the horizontal axis is in units of $\delta\omega \cdot \tau_{\text{bu}}$, where $\delta\omega$ is the frequency difference between the two resonators and $\tau_{\text{bu}} = 33\frac{1}{3}$ ns. The horizontal width of ~ 0.4 at $\eta = 0.94$ corresponds to a frequency mismatch of 0.5 MHz. Since we have assumed 6 GHz resonators this is only a $\sim 0.02\%$ tolerance for resonator frequency mismatch.

coefficients of the inductive couplers changes the effective frequency of the resonators, creating a much more complicated situation. However, for the purposes of this investigation we only need the upper-bound estimate given by simulation with constant (fixed) frequency mismatch.

In general, in order to simulate this procedure with different frequencies we would need to modify both Eqs. (5.2) and (5.9). However, this can be done in a simple way by keeping the resonator frequencies equal and modifying Eq. (5.2) to include a phase shift for the incoming field as seen by the receiving resonator. The evolution of the field in the receiving resonator can then be written (again assuming the high-Q limit

and $\phi = 0$) as

$$\dot{B} = -\frac{|t_{\rm rec}|^2}{2\tau_{rt}} B + \frac{t_{\rm rec}}{\tau_{rt}} A \, \mathrm{e}^{\mathrm{i}\,\delta\omega\, t}, \tag{5.10}$$

where $\delta\omega = 2\pi(f_{\rm rec} - f_{\rm em})$ is the frequency difference of the two resonators. For our simulation we have used the same ideal values as the previous section.

The transfer efficiency as a function of the fixed frequency mismatch is shown in Fig. 5.6 for three desired efficiencies $\eta_{design} = 0.9999$, 0.995, and 0.99. Notice that for all procedures a small mismatch $\delta\omega \sim 0.5$ MHz corresponds to a 2-4% decrease in the efficiency. This procedure has a very low tolerance for the frequency mismatch $(\delta\omega/2\pi f) \ll 1\%$. Although this is a very crude estimate, it illustrates that the effective frequency change during transmission coefficient modulation will likely require active compensation.

5.5 Summary

In this chapter we numerically studied deviations from the ideal qubit transfer protocol originally proposed in Ref. [8]. We considered procedural errors arising from experimental implementation and the effect of a resonator frequency mismatch. In Sec. 5.3 we simulated the procedure with three deviations from the ideal time-dependence of the transmission coefficients given in Eqs. (5.3)-(5.5). The slow decrease of solid lines in Fig. 5.3 shows that an error in only one of the switching times is not a limiting factor for the procedure. Figure 5.4 shows that neither an error in just one (solid lines) nor both (dashed lines) of the shaping parameters for the transmission coefficients' time-dependence causes a drastic decrease in the transfer efficiency. Similarly, Fig. 5.5 shows that neither an error of just one (solid lines) nor both (dashed lines) of the maximum transmission coefficients are cause for concern. In Sec. 5.4 we present the efficiency of

the transfer protocol when performed with resonators that have unequal frequencies. The rapid decrease of the efficiency in Fig. 5.6 illustrates the necessity of maintaining nearly equal resonator frequencies throughout the duration of the transfer protocol.

Chapter 6

Conclusion

In this dissertation we examined several protocols relevant for experiments with superconducting qubits. In Ch. 2 a novel application of quantum uncollapsing that protects a qubit state from decoherence due to zero-temperature energy relaxation was proposed and analyzed. This procedure preferentially selects the cases without energy decay events. Stronger decoherence suppression requires smaller selection probability; a desired point in this trade-off can be chosen by varying the measurement strength. Following our original proposal, the procedure was successfully demonstrated in another group using a photonic polarization qubit, and was later extended to protect an entangled qubit pair. Currently, the uncollapsing (which involves selection of certain measurement results) is *the only* known to us way of improving the qubit storage fidelity against energy relaxation, which does not rely on encoding a logical qubit in a larger Hilbert space.

In Ch. 3 we have analyzed the performance of N-qubit repetitive quantum codes in the presence of energy relaxation. As expected, these codes are not usable for quantum error correction; however, they can be used for quantum error detection. The

best QED performance for weak energy relaxation is provided by the 3-qubit repetitive encoding, while the 2-qubit encoding is sufficient and has only a slight decrease in performance. We have found that the main contribution to the QED infidelity for $N \geq 3$ comes from the non-unitary change of the quantum state in the case when no relaxation happens. We have discussed how this effect can be compensated for by dividing the QED procedure into an even number of cycles with π-pulses between each cycle.

In Ch. 4 we have considered simple two-qubit quantum error detecton/correction protocols, suitable for present-day experiments with superconducting qubits. In the first protocol the errors are simulated by applying intentional unitary rotations to the qubit states (two types of rotations for each qubit). In this case not only QED, but also QEC operation is possible when we know the type and location of the applied error rotation. Most importantly, this experiment would demonstrate the QEC "miracle" of converting continuous quantum errors into discrete errors, which are then correctable. In the other protocols, which can only be used for QED, the detectable errors are due to energy relaxation during an extended storage period. Our numerical simulations, which account for realistic decoherence during the entire duration of each procedure, show that the QEC/QED protocols can be presently realized with superconducting phase qubits.

In Ch. 5 we investigated the robustness of a procedure for transferring the state of a microwave qubit from one resonator to another resonator via a long transmission line, the emission and capture of microwave energy is achieved using tunable couplers. The ideal procedure assumes perfect control of the tunable couplers. We studied deviations from the ideal procedure by simulating experimental imperfections of required pulse shaping, and our results show that the procedure is robust to these errors. Additionally, we have found that it is necessary to maintain nearly equal resonator frequencies during the transfer procedure.

Bibliography

[1] Quant. Inf. Proc. **8**, no. 2 (2009): Special issue on quantum computing with superconducting qubits.

[2] A. N. Korotkov and A. N. Jordan, Phys. Rev. Lett. **97**, 166805 (2006).

[3] P. W. Shor, Phys. Rev. A **52**, R2493 (1995).

[4] A. R. Calderbank and P. W. Shor, Phys. Rev. A **54**, 1098 (1996).

[5] A. M. Steane, Phys. Rev. Lett. **77**, 793 (1996)

[6] D. Gottesman, Phys. Rev. A **54**, 1862 (1996).

[7] M. A. Nielsen and I. L. Chuang, *Quantum computation and quantum information* (Cambridge University Press, Cambridge, 2000).

[8] A. N. Korotkov, Phys. Rev. B **84**, 014510 (2011).

[9] D. A. Lidar, I. L. Chuang, and K. B. Whaley, Phys. Rev. Lett. **81**, 2594 (1998).

[10] L. Viola, E. Knill, and S. Lloyd, Phys. Rev. Lett. **82**, 2417 (1999).

[11] L. P. Pryadko and G. Quiroz, Phys. Rev. A **80**, 042317 (2009).

[12] S. Haroche and D. Kleppner, Phys. Today **42**, No. 1, 24 (1989).

[13] A. N. Korotkov and K. Keane, Phys. Rev. A **81**, 040103(R) (2010).

[14] N. Katz et al., Phys. Rev. Lett. **101**, 200401 (2008).

[15] Y. Kim, Y. Cho, Y. Ra, and Y. Kim, Nat. Phys. **17**, 11978 (2009).

[16] J. Lee, Y. Jeong, Y. Kim, and Y. Kim, Opt. Express **19**, 16309 (2011).

[17] Y. Kim, J. Lee, O. Kwon, and Y. Kim, Nat. Phys. **8**, 117 (2012)

[18] A. N. Korotkov, Nat. Phys. **8**, 107 (2012)

[19] D. G. Cory, M. D. Price, W. Maas, E. Knill, R. Laflamme, W. H. Zurek, T. F. Havel, and S. S. Somaroo, Phys. Rev. Lett. **81**, 2152 (1998).

[20] E. Knill, R. Laflamme, R. Martinez, and C. Negrevergne, Phys. Rev. Lett. **86**, 5811 (2001).

[21] N. Boulant, L. Viola, E. M. Fortunato, and D. G. Cory, Phys. Rev. Lett. **94**, 130501 (2005).

[22] O. Moussa, J. Baugh, C. A. Ryan, and R. Laflamme, Phys. Rev. Lett. **107**, 160501 (2011).

[23] N. C. Menicucci and C. M. Caves, Phys. Rev. Lett. **88**, 167901 (2002).

[24] J. Chiaverini, D. Leibfried, T. Schaetz, M. D. Barrett, R. B. Blakestad, J. Britton, W. M. Itano, J. D. Jost, E. Knill, C. Langer, R. Ozeri, and D. J. Wineland, Nature **432**, 602 (2004).

[25] P. Schindler, J. T. Barreiro, T. Monz, V. Nebendahl, D. Nigg, M. Chwalla, M. Hennrich, and R. Blatt, Science **332**, 1059 (2011).

[26] T. B. Pittman, B. C. Jacobs, and J. D. Franson, Phys. Rev. A **71**, 052332 (2005).

[27] T. Aoki, G. Takahashi, T. Kajiya, J. Yoshikawa, S. L. Braunstein, P. van Loock, and A. Furusawa, Nature Phys. **5**, 541 (2009).

[28] M. Lassen, M. Sabuncu, A. Huck, J. Niset, G. Leuchs, N. J. Cerf, and U. L. Andersen, Nature Photonics **4**, 700 (2010).

[29] X. C. Yao, T. X. Wang, H. Z. Chen, W. B. Gao, A. G. Fowler, R. Raussendorf, Z. B. Chen, N. L. Liu, C. Y. Lu, Y. J. Deng, Y. A. Chen, and J. W. Pan, Nature **482**, 489 (2012).

[30] M. D. Reed, L. DiCarlo, S. E. Nigg, L. Sun, L. Frunzio, S. M. Girvin, and R. J. Schoelkopf, Nature **482**, 382 (2012).

[31] J. Clarke and F. K. Wilhelm, Nature **453**, 1031 (2008).

[32] B. G. Levi, Phys. Today **62**, no. 7, 14 (2009).

[33] I. Siddiqi, Supercond. Sci. Technol. **24**, 091002 (2011).

[34] S. M. Girvin, M. H. Devoret, and R. J. Schoelkopf, Phys. Scr. **T137**, 014012 (2009).

[35] L. DiCarlo et al., Nature **460**, 240 (2009).

[36] K. Keane and A. N. Korotkov, Phys. Rev. A **86**, 012333 (2012).

[37] K. Keane and A. N. Korotkov, "Modeling of a Flying Microwave Qubit," *APS March Meeting* (Boston, MA, February 27 - March 2, 2012), Bulletin of APS **57**, No. 1, Y29.00010.

[38] M. A. Nielsen, Phys. Lett. A **303**, 249 (2002).

[39] J. L. O'Brien et al., Phys. Rev. Lett. **93**, 080502 (2004).

[40] N. Katz et al., Science **312**, 1498 (2006).

[41] M. D. Bowdrey, D. K. L. Oi, A. J. Short, K. Banaszek, and J. A. Jones, Phys. Lett. A **294**, 258 (2002).

[42] J. Martinis, S. Nam, J. Aumentado, and C. Urbina, Phys. Rev. Lett. **89**, 117901 (2002).

[43] J. M. Martinis, Quant. Inf. Proc. **8**, 81 (2009).

[44] M. Mariantoni et al., Science **334**, 61 (2011).

[45] A. Galiautdinov, A. N. Korotkov, and J. Martinis, Phys. Rev. A **85**, 042321 (2012).

[46] T. Yamamoto et al., Phys. Rev. B **82**, 184515 (2010).

[47] J. Clarke and A.I. Braginski, *The SQUID Handbook: Fundamentals and Technology of SQUIDs and SQUID Systems* (Wiley-VCH, Weinheim, 2004).

[48] A. N. Korotkov, Phys. Rev. B **60**, 5737 (1999).

[49] A. A. Houck, J. Koch, M. H. Devoret, S. M. Girvin, and R. J. Schoelkoph, Quantum Inf. Process. **8**, 105 (2009).

[50] E. Knill, R. Laflamme, and G. J. Milburn, Nature **409**, 46 (2001).

[51] L. Tornberg, M. Wallquist, G. Johansson, V. S. Shumeiko, and G. Wendin, Phys. Rev. B **77**, 214528 (2008).

[52] B. R. Johnson et al., Nature Phys. **6**, 663 (2010).

[53] R. Laflamme, C. Miquel, J. P. Paz, W. H. Zurek, Phys. Rev. Lett. **77**, 198 (1996)

[54] D. Leung, L. Vandersypen, X. Zhou, M. Sherwood, C. Yannoni, M. Kubinec, and I. Chuang, Phys. Rev. A **60**, 1924 (1999).

[55] Q. Sun, M. Al-Amri, L. Davidovich, and M. Zubairy, Phys. Rev. A **82**, 052323 (2010)

[56] M. Al-Amri, M. Scully, and M. Zubairy, J. Phys. B **44**, 165509 (2011)

[57] D. Leung, M. Nielsen, I. Chuang, and Y. Yamamoto, Phys. Rev. A **56**, 2567 (1997).

[58] A. Fletcher, P. Shor, and M. Win, IEEE Trans. Inf. Theory **54**, 5705 (2008).

[59] P. Shor, G. Smith, J. Smolin, and B. Zeng, IEEE Trans. Inf. Theory **57**, 7180 (2011).

[60] L. Viola, E. Knill, and S. Lloyd, Phys. Rev. Lett. **82**, 2417 (1999).

[61] K. Jahne, B. Yurke, and U. Gavish, Phys. Rev. A **75**, 010301 (2007).

[62] R. Bialsak et al., Phys. Rev. Lett. **106**, 060501 (2011).

[63] Z. Merali, Nature News **454**, 8 (2008).

[64] K. Keane and A. N. Korotkov, "Currently Realizable Quantum Error Detection/Correction Algorithms for Superconducting Qubits," *APS March Meeting* (Dallas, TX, March 21-25, 2011), Bulletin of APS **56**, No. 1, D27.00010.

[65] K. Keane and A. N. Korotkov, "Decoherence Suppression of a Solid State Qubit by Uncollapsing," *APS March Meeting* (Portland, OR, March 15-19, 2010), Bulletin of APS **55**, No. 2, Z33.00011.

[66] M. Horodecki, P. Horodecki, and R. Horodecki, Phys. Rev. A **60**, 1888 (1999).

[67] J. Preskill, Proc. R. Soc. A **454**, 385 (1998).

[68] E. Dennis, A. Kitaev, A. Landahl, and J. Preskill, J. Math. Phys. **43**, 4452 (2002).

[69] S. B. Bravyi and A. Y. Kitaev, quant-ph/9811052

[70] A. Fowler, A. Stephens, and P. Groszkowski, Phys. Rev. A **80**, 052312 (2009).

Appendix A

List of publications and presentations by Kyle Keane

Articles

1. A. N. Korotkov and K. Keane, "Decoherence suppression by quantum measurement reversal," *Phys. Rev. A*, vol. **81**, 040103, Apr 2010.
2. K. Keane and A. N. Korotkov, "Simplified quantum error detection and correction for superconducting qubits," *Phys. Rev. A*, vol. **86**, 012333, Jul 2012.

Presentations

1. K. Keane and A. N. Korotkov, "Decoherence Suppression of a Solid State Qubit by Uncollapsing," *APS March Meeting* (Portland, OR, March 15-19, 2010), Bulletin of APS, vol. **55**, no. 2, Z33.00011.
2. K. Keane and A. N. Korotkov, "Currently Realizable Quantum Error Detection/Correction Algorithms for Superconducting Qubits," *APS March Meeting*

(Dallas, TX, March 21-25, 2011), Bulletin of APS, vol. **56**, no. 1, D27.00010.

3. K. Keane and A. N. Korotkov, "Modeling of a Flying Microwave Qubit," *APS March Meeting* (Boston, MA, February 27 - March 2, 2012), Bulletin of APS, vol. **57**, no. 1, Y29.00010.

Posters

1. A. N. Korotkov, R. Pinto, and K. Keane, "Theoretical Analysis of Phase Qubits," *Quantum Computing Program Review* (Minneapolis, MN, August 17-21, 2009).

2. K. Keane and A. N. Korotkov, "Suppression of T_1-type Decoherence of Phase Qubits using Uncollapsing and Quantum Error Detection/Correction," *Coherence in Superconducting Qubits* (San Diego, CA, April 25-28, 2010).

Appendix B

Three-qubit repetitive coding

As was mentioned in section 1.1, one of the main techniques for decoherence suppression [7] is quantum error correction, where one logical qubit is stored in some number of entangled physical qubits in such a way that errors can be identified and corrected. In this section repetitive coding (the simplest example of quantum error correction) is introduced. It is well known that the three-qubit repetitive code allows a bit-flip of an unknown qubit to be uniquely detected and corrected. [see Ref. [7] for the standard analysis of this code – usually referred to as the bit-flip code for obvious reasons]. After a very brief introduction to classical repetitive coding, the quantum code is presented in a slightly different manner than usual in order to illustrate the "compact" scheme of using the ancilla qubits for syndrome measurement.

In classical error correction information is represented in bits, a bit is a variable which can only take one of two values – denoted here as $\{0\}$ or $\{1\}$. One possible error that can occur on a bit is called a bit-flip, this is when the value of the bit is exchanged for its counterpart: if the bit is $\{0\}$ before the bit-flip, it is $\{1\}$ after and vice-versa. The bit-flip of $\{0\}$ will be represented as $\{0\} \rightarrowtail \{1\}$ (and similarly the bit-flip $\{1\} \rightarrowtail \{0\}$).

If a bit of information is stored redundantly in three identical copies $\{0\} \rightarrow \{000\}$, or $\{1\} \rightarrow \{111\}$, it is easy to see that a simple majority vote is sufficient to protect a bit of information from a single bit-flip since,

$$\{000\} \rightarrowtail \{100\} \text{ or } \{010\} \text{ or } \{001\}, \tag{B.1}$$

or

$$\{111\} \rightarrowtail \{011\} \text{ or } \{101\} \text{ or } \{110\}. \tag{B.2}$$

In quantum computation an unknown two-level quantum state is the analogy of the classical bit. However, full information about an unknown quantum state cannot be obtained (no-cloning theorem [7]), which means direct redundancy is not possible. The alternative is to "smartly" entangle multiple qubits such that information can be obtained about the evolution of the system without learning about (and thus destroying) the original superposition. In the general theory of QEC this "smart" entanglement is represented as a quantum controlled-gate. A two-qubit controlled-gate performs an single-qubit quantum operation on one of the qubits (target) conditioned on the state of the other qubit (control). For repetitive coding the controlled-NOT (CNOT) gate is used, which conditioned on the state of the control qubit performs a Pauli X-gate on the target qubit only if the control qubit is in state $|1\rangle$. [The Pauli X-gate is defined as the usual Pauli X-matrix acting in the computation basis defined in 1.2.] This operation transforms the two-qubit basis states as

$$|00\rangle \rightarrow |00\rangle,\ |01\rangle \rightarrow |01\rangle,\ |10\rangle \rightarrow |11\rangle,\ |11\rangle \rightarrow |10\rangle. \tag{B.3}$$

This transformation is equivalent to switching the coefficients in front of states $|10\rangle$ and $|11\rangle$, while leaving the other two states unchanged.

Repetitive coding is performed by using a CNOT gate from an unknown qubit state onto individual ancilla qubits in known states. The bit-flip code is performed

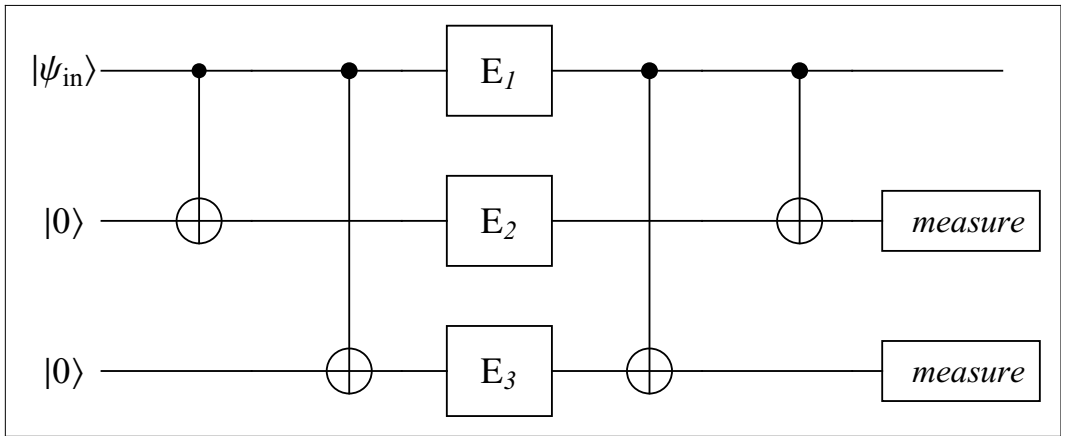

Figure B.1: Quantum circuit diagram for 3-qubit repetitive code (commonly referred to as the bit-flip code in traditional quantum error correction). A qubit initially in state $|\psi_{\text{in}}\rangle = \alpha|0\rangle+\beta|1\rangle$ is encoded into the entangled three-qubit state $|\psi_{\text{en}}\rangle = \alpha|000\rangle+\beta|111\rangle$ using a CNOT gate from the main qubit to the two ancilla qubits (both initially in state $|0\rangle$). After a bit flip of any one of the three qubits, the qubits are decoded using the same CNOT gates (in the reverse sequence) and the ancilla qubits are projectively measured in the computational basis (called syndrome measurement). The main qubit is returned to its initial state $|\psi_{\text{in}}\rangle$ by applying an appropriate correction operation for a given syndrome measurement result. The code can also be used for quantum error detection; in this case the main qubit is kept for the syndromes that require no correction operation, while in other cases it is known that the procedure has failed.

using three qubits (labelled 1, 2, and 3), the main qubit (qubit 1) is initially in the state $|\psi_1\rangle = \alpha|0\rangle + \beta|1\rangle$ and ancillas are in $|\psi_2\rangle = |\psi_3\rangle = |0\rangle$, where the unknown state $|\psi_1\rangle$ is what should be protected. As described in Sec. 1.2 the initial state of the system, in the three-qubit computational basis, can be written as $|\psi_{in}\rangle = \alpha|000\rangle + \beta|100\rangle$.

The quantum circuit diagram for three-qubit repetitive coding is shown in Fig. B.1. First, a CNOT gate is applied with the main qubit as control onto each ancilla qubit, which transforms the state to

$$|\psi_{en}\rangle = \alpha|000\rangle + \beta|111\rangle. \tag{B.4}$$

This primary entangling operation is referred to as encoding. If a bit-flip occurs on one

of the qubits after encoding, then the three-qubit wavefunction becomes

$$|\psi_{en}^{\{1\}}\rangle = \alpha|100\rangle + \beta|011\rangle, \tag{B.5}$$

$$|\psi_{en}^{\{2\}}\rangle = \alpha|010\rangle + \beta|101\rangle, \tag{B.6}$$

$$|\psi_{en}^{\{3\}}\rangle = \alpha|001\rangle + \beta|110\rangle, \tag{B.7}$$

where $|\psi_{en}^{\{n\}}\rangle$ means the nth qubit was bit-flipped.

To decode and detect the errors, the inverse of the encoding procedure is performed, namely CNOT gates with the main qubit as control onto each ancilla. This produces the separable (decoded) states

$$|\psi_{de}^{\{none\}}\rangle = (\alpha|0\rangle + \beta|1\rangle) \otimes |00\rangle, \tag{B.8}$$

$$|\psi_{de}^{\{1\}}\rangle = \alpha|111\rangle + \beta|011\rangle = (\beta|0\rangle + \alpha|1\rangle) \otimes |11\rangle, \tag{B.9}$$

$$|\psi_{de}^{\{2\}}\rangle = \alpha|010\rangle + \beta|110\rangle = |\psi_1\rangle \otimes |10\rangle, \tag{B.10}$$

$$|\psi_{de}^{\{3\}}\rangle = \alpha|001\rangle + \beta|101\rangle = |\psi_1\rangle \otimes |01\rangle, \tag{B.11}$$

where the state of qubit 1 has been separated explicitly from the state of the ancilla qubits for syndrome measurement. [If no bit-flip occurred, the state is returned to $|\psi_{in}\rangle$ since the CNOT gate is its own inverse operation.] To detect an error the ancilla qubits are measured and four results are possible: {00} if no bit-flip occurred or {11}, {10}, or {01} if the bit-flip affected qubit 1, 2, or 3 respectively. Since these measurement results uniquely identify which error has occurred they are referred to as the "syndrome" of each error.

At this stage, the procedure can be continued in three ways: ignore the syndrome measurement and do nothing, apply an appropriate correction for each syndrome, or discard some cases. The last two options are quantum error correction and detection respectively. For QEC, a π-pulse is applied to the main qubit only if syndrome {11} is

measured and nothing is done otherwise. If this approach is taken then $|\psi_1\rangle$ is recovered in all cases. In QED, if we choose to discard cases when syndrome $\{11\}$ is measured, then $|\psi_1\rangle$ will be recovered in all retained cases. The benefit in this selective procedure is that no measurement-conditioned operations are required (which are currently experimentally difficult).

Appendix C

Averaging over the Bloch sphere

This appendix contains some general results for averaging over the Bloch sphere, relevant for both selective and non-selective procedures. In order to represent an arbitrary qubit state $|\psi\rangle$ on the Bloch sphere, Eq. (1.1) is rewritten as

$$\alpha|0\rangle + \beta|1\rangle = \cos[\theta/2]|0\rangle + \sin[\theta/2]\,\mathrm{e}^{\mathrm{i}\phi}|1\rangle \tag{C.1}$$

by defining $\alpha \equiv \cos[\theta/2]$ and $\beta \equiv \sin[\theta/2]\,\mathrm{e}^{\mathrm{i}\phi}$. This representation has a geometric interpretation as a point on a unit sphere (called the Bloch sphere). Integrating over the surface of this sphere is equivalent to integrating over all possible pure states of a two-level system. Averaging any function (let's call it f) of θ and ϕ (or α and β) over the Bloch sphere is thus calculating as

$$\overline{f(\theta,\,\phi)} = \frac{1}{4\pi}\int_{\phi=0}^{2\pi}\int_{\theta=0}^{\pi} f(\theta,\,\phi)\sin[\theta]\,\mathrm{d}\theta\,\mathrm{d}\phi. \tag{C.2}$$

For the purposes of this dissertation the following general results are sufficient

to calculate all necessary averages over the Bloch sphere:

$$\overline{|\alpha|^4} = \overline{|\beta|^4} = \int_0^\pi \frac{(1+\cos\theta)^2}{4}\,\frac{\sin\theta}{2}\,d\theta = \frac{1}{3}, \tag{C.3}$$

$$\overline{|\alpha|^2|\beta|^2} = \int_0^\pi \frac{(1+\cos\theta)(1-\cos\theta)}{4}\,\frac{\sin\theta}{2}\,d\theta = \frac{1}{6}, \tag{C.4}$$

$$\overline{|\alpha|^2} = \overline{|\beta|^2} = \frac{1}{2},\ \ \overline{|\alpha|^6} = \overline{|\beta|^6} = \frac{1}{4}, \tag{C.5}$$

$$\overline{|\alpha|^2|\beta|^4} = \overline{|\alpha|^4|\beta|^2} = \frac{1}{12},\ \ \overline{|\alpha|^4|\beta|^4} = \frac{1}{30}, \tag{C.6}$$

$$\overline{1/(A+B|\beta|^2)} = (1/B)\ln(1+B/A), \tag{C.7}$$

$$\overline{|\beta|^2/(A+B|\beta|^2)} = (1/B) - (A/B^2)\ln(1+B/A), \tag{C.8}$$

$$\overline{|\beta|^4/(A+B|\beta|^2)} = \frac{1}{2B} - \frac{A}{B^2} + \frac{A^2}{B^3}\ln(1+B/A), \tag{C.9}$$

$$\overline{\frac{|\alpha|^4}{A+B|\beta|^2}} = \frac{-3}{2B} - \frac{A}{B^2} + \frac{(A+B)^2}{B^3}\ln(1+B/A), \tag{C.10}$$

$$\overline{\frac{|\alpha|^2|\beta|^2}{A+B|\beta|^2}} = \frac{1}{2B} + \frac{A}{B^2} - \frac{A(A+B)}{B^3}\ln(1+B/A), \tag{C.11}$$

where A and B are constants and $|\alpha|^2 = (1+\cos\theta)/2$ and $|\beta|^2 = (1-\cos\theta)/2$.

Appendix D

Six-point averaging and optimal unitary corrections

In this appendix we prove that no additional unitary operation can improve the fidelity of the protocol discussed in Ch. 3 (for 2-qubit or N-qubit encoding) in the case of "no error" measurement result (0 or $\mathbf{0}$). We also prove that for a measurement result which indicates an error, the optimal correction is either identity or the π-pulse, exchanging $|0\rangle$ and $|1\rangle$. Along the way we also discuss the trick [38, 41] of using only 6 initial states for averaging the state fidelity over the Bloch sphere.

Let us first consider an arbitrary (not necessarily trace-preserving) linear one-qubit quantum operation, which transforms initial states $|1\rangle$, $|0\rangle$, $|\pm\rangle \equiv (|0\rangle \pm |1\rangle)/\sqrt{2}$, $|\pm i\rangle \equiv (|0\rangle \pm i|1\rangle)/\sqrt{2}$ into the density matrices ρ_0, ρ_1, $\rho_\pm$, $\rho_{\pm i}$. The center of the Bloch sphere $(|0\rangle\langle 0| + |1\rangle\langle 1|)/2 = I/2$ is transformed into ρ_c. Because of the linearity, only four linearly independent initial states are sufficient to define the operation. So, for an initial state with the Bloch sphere coordinates $\{x, y, z\}$,

$$\rho_{\rm in} = (I + xX + yY + zZ)/2, \tag{D.1}$$

where $\{X, Y, Z\}$ are the Pauli matrices ($x = 1$ corresponds to $|+\rangle$, $y = 1$ corresponds to $|+i\rangle$, $z = 1$ corresponds to $|0\rangle$), the final state is

$$\rho_{\rm fin} = \rho_c + x(\rho_+ - \rho_c) + y(\rho_{+i} - \rho_c) + z(\rho_0 - \rho_c). \tag{D.2}$$

To compare this operation with a unitary U, we calculate the state fidelity $\mathrm{Tr}(\rho_{\rm fin}\rho_{\rm fin}^U)$ (the superscript U in a notation means that it relates to the unitary U),

$$\begin{aligned} F_{\rm st} = \mathrm{Tr}\{&[\rho_c + x(\rho_+ - \rho_c) + y(\rho_{+i} - \rho_c) + z(\rho_0 - \rho_c)] \\ &\times[\rho_c^U + x(\rho_+^U - \rho_c^U) + y(\rho_{+i}^U - \rho_c^U) + z(\rho_0^U - \rho_c^U)]\}. \end{aligned} \tag{D.3}$$

Note that $\rho_c^U = I/2$, since a unitary operation does not change the Bloch sphere center. In averaging $F_{\rm st}$ over the Bloch sphere we average over the coordinates $\{x, y, z\}$ and use the obvious relations $\overline{x} = \overline{y} = \overline{z} = \overline{xy} = \overline{xz} = \overline{yz} = 0$, $\overline{x^2} = \overline{y^2} = \overline{z^2} = 1/3$, thus obtaining

$$\begin{aligned} \overline{F} = \frac{1}{2}\mathrm{Tr}\rho_c + \frac{1}{3}\mathrm{Tr}[&(\rho_+ - \rho_c)(\rho_+^U - \rho_c^U) \\ &+(\rho_{+i} - \rho_c)(\rho_{+i}^U - \rho_c^U) + (\rho_0 - \rho_c)(\rho_0^U - \rho_c^U)]. \end{aligned} \tag{D.4}$$

Note that in general we deal here with non-normalized density matrices, in contrast to the formalism used in Ch. 3. Therefore, compared with notations of Ch. 3, $\overline{F} = F_{\rm av} = \widetilde{F}_{\rm av}$ only for a trace-preserving operation, while for a non-trace-preserving operation $\overline{F} = \widetilde{F}_{\rm av}\overline{P}$, where $\overline{P}$ is the average probability of selection [see Eq. (1.24)], and there is no direct relation between $\overline{F}$ and $F_{\rm av}$.

Using Eq. (D.4) it is easy to see why averaging over the Bloch sphere is equivalent to averaging over only 6 initial states: $|0\rangle$, $|1\rangle$, $|\pm\rangle$, and $|\pm i\rangle$. The state fidelity F_+ for the initial state $|+\rangle$ is given by Eq. (D.3) with $x = 1$ and $y = z = 0$. The state fidelity F_- for the initial state $|-\rangle$ is similar, but $x = -1$. It is easy to obtain the sum,

$F_+ + F_- = \mathrm{Tr}\rho_c + 2\mathrm{Tr}[(\rho_+ - \rho_c)(\rho_+^U - \rho_+^U)]$, which is similar to the terms in Eq. (D.4). Similarly finding the sums $F_{+i} + F_{-i}$ and $F_0 + F_1$, we obtain [38, 41]

$$\overline{F} = (F_0 + F_1 + F_+ + F_- + F_{+i} + F_{-i})/6. \tag{D.5}$$

Note that this relation remains valid for non-trace-preserving operations, when we are working with a linear operation and non-normalized states. The same six-point-averaging relation is valid for the average probability of selection $\overline{P}$, because $P = \mathrm{Tr}\rho_{\mathrm{fin}}$ and therefore $\overline{P} = \mathrm{Tr}\rho_c$ (even two-point averaging is sufficient for $\overline{P}$, when we choose two opposite points on the Bloch sphere). Therefore the six-point-averaging trick is useful for finding $\widetilde{F}_{\mathrm{av}} = \overline{F}/\overline{P}$.

Now let us discuss why an additional unitary cannot improve the QEC protocols of Ch. 3 when the "no error" measurement result 0 (or **0**) is obtained. The final state in this case is an incoherent mixture of the results of two linear operations:

$$\alpha|0\rangle + \beta|1\rangle \to \alpha|0\rangle + k\beta|1\rangle, \quad \alpha|0\rangle + \beta|1\rangle \to \tilde{k}\beta|0\rangle, \tag{D.6}$$

where the real positive constants k and $\tilde{k}$ should obviously satisfy inequality $k^2 + \tilde{k}^2 \leq 1$. For this operation it is easy to find explicitly

$$\rho_c = (1 + \tilde{k}^2 + k^2)I/4 + (1 + \tilde{k}^2 - k^2)Z/4, \tag{D.7}$$

$$\rho_+ = \rho_c + kX/2, \ \rho_{+i} = \rho_c + kY/2, \ \rho_0 = (Z + I)/2. \tag{D.8}$$

Then using Eq. (D.4) we obtain

$$\begin{aligned}\overline{F} = \frac{1}{4}(1 + k^2 + \tilde{k}^2) + \frac{1}{6}\mathrm{Tr}[kX(\rho_+^U - \rho_c^U) \\ + kY(\rho_{+i}^U - \rho_c^U) + \frac{1 - \tilde{k}^2 + k^2}{2}Z(\rho_0^U - \rho_c^U)].\end{aligned} \tag{D.9}$$

(Note that comparing the operation with U we assume the correction operation $U^\dagger$.) Optimizing each term under the trace over the unitary U separately, we see that the

first term is maximized by unitaries, which transform $|+\rangle \to |+\rangle$; the maximum for the second term is achieved when $|+i\rangle \to |+i\rangle$, and the maximum for the third term is achieved when $|0\rangle \to |0\rangle$ (note that $k \geq 0$ and $1 - \tilde{k}^2 + k^2 \geq 0$). Since the no-evolution operation satisfies all these conditions, it provides the maximum fidelity,

$$U_{\rm best} = I, \;\; \overline{F} = \frac{1 + k + k^2 + \tilde{k}^2/2}{3}. \tag{D.10}$$

Note that the average probability of the process (D.6) is $\overline{P} = (1 + k^2 + \tilde{k}^2)/2$, so $\widetilde{F}_{\rm av} = (2/3)(1 + k + k^2 + \tilde{k}^2)/(1 + k^2 + \tilde{k}^2)$. In particular, this is an alternative way of deriving Eq. (3.11) by using $k = \sqrt{1 - p_1}\sqrt{1 - p_2}$ and $\tilde{k} = \sqrt{p_1 p_2}$.

Now let us discuss what is the optimal unitary correction operation after obtaining the measurement result 1 in 2-qubit encoding or any result except $\mathbf{0}$ in N-qubit encoding. Then the resulting state is an incoherent mixture of two linear operations:

$$\alpha|0\rangle + \beta|1\rangle \to k\beta|1\rangle, \;\; \alpha|0\rangle + \beta|1\rangle \to \tilde{k}\beta|0\rangle. \tag{D.11}$$

Finding explicitly the resulting density matrices

$$\rho_0 = 0, \;\; \rho_c = \rho_+ = \rho_{+i} = \frac{\tilde{k}^2}{2}|0\rangle\langle 0| + \frac{k^2}{2}|1\rangle\langle 1|, \tag{D.12}$$

we obtain from Eq. (D.4)

$$\overline{F} = \frac{k^2 + \tilde{k}^2}{4} + \frac{k^2 - \tilde{k}^2}{12}\,{\rm Tr}[Z(\rho_0^U - \rho_c^U)]. \tag{D.13}$$

Therefore if $k \geq \tilde{k}$, then the maximum fidelity $\overline{F}_{\rm max} = (2k^2 + \tilde{k}^2)/6$ is achieved for any unitary U, which does not change $|0\rangle$ (same for the correcting operation $U^\dagger$). However, if $k \leq \tilde{k}$, then the optimal U transforms $|0\rangle \to |1\rangle$ (same for $U^\dagger$) and $\overline{F}_{\rm max} = (k^2 + 2\tilde{k}^2)/6$.

Appendix E

Explicit error scenarios for N-qubit repetitive code

In this appendix the techniques used to analyze the N-qubit repetitive code (Ch. 3) are discussed. After applying a CNOT from the main qubit in figure 3.1 to each ancilla qubit, the N-qubit wavefunction is $\alpha|0^N\rangle + \beta|1^N\rangle$. If the main qubit relaxes then the decoding will not change the state of any ancilla qubits since relaxation will put the main qubit into state $|0\rangle$ and a CNOT from this state does not change the target qubit. Therefore after decoding, the measurement result 0 for an ancilla qubit indicates that relaxation has occurred. If the main qubit does not relax during the storage period (between encoding and decoding), then relaxation of an ancilla qubit is indicated by measurement result 1. There are 2^N scenarios: No qubits relax, one qubit relaxes, two qubits relax, ..., $N-1$ qubits relax, all N qubits relax. Each of the 2^{N-1} possible syndromes (string of $N-1$ 1's and 0's from measurement of the ancilla qubits) correspond to a set of two scenarios (one when the main qubit relaxes and the other when it does not).

If no qubits relax (all $N-1$ ancilla measurements are 0), the final state will be $\left|\Psi_0^N\right\rangle = \frac{1}{\sqrt{\Delta_j}}(\alpha\left|0\right\rangle^N + \beta(1-p)^{\frac{N}{2}}\left|1\right\rangle^N)$, where $\Delta_N = \left|\alpha\right|^2 + \left|\beta\right|^2(1-p)^N$. The full spectrum of other possibilities is contained in Table E.1. Let us introduce the notation used in Table E.1 by first discussing the case when just two qubits relax. If the main qubit is one of the two which relax then the final state of the system before decoding is one of the following (we label the qubit number for clarity as a subscript): $|0_1 0_2 1_3 1_4 \ldots 1_{N-1} 1_N\rangle$, $|0_1 1_2 0_3 1_4 \ldots 1_{N-1} 1_N\rangle$, $|0_1 1_2 1_3 0_4 \ldots 1_{N-1} 1_N\rangle$, ..., $|0_1 1_2 1_3 1_4 \ldots 0_{N-1} 1_N\rangle$, or $|0_1 1_2 1_3 1_4 \ldots 1_{N-1} 0_N\rangle$. This set of possibilities will be written as $\left|0, \{0^1, 1^{N-1}\}\right\rangle$ and the number of possibilities is found using simple combinatorics (i.e. there are $\binom{N-1}{N-2}$ ways to place the $N-2$ "1's" within the $N-1$ spaces in the curly braces. If the main qubit does not relax, the final state before decoding is one of the following: $|1_1 0_2 0_3 1_4 \ldots 1_{N-1} 1_N\rangle$, $|1_1 0_2 1_3 0_4 \ldots 1_{N-1} 1_N\rangle$, ..., $|1_1 0_2 1_3 1_4 \ldots 1_{N-1} 0_N\rangle$, $|1_1 1_2 0_3 0_4 \ldots 1_{N-1} 1_N\rangle$, ..., $|1_1 1_2 0_3 1_4 \ldots 0_{N-1} 1_N\rangle$, $|1_1 1_2 0_3 1_4 \ldots 1_{N-1} 0_N\rangle$, ... Employing the same notation as before we can summarize all of these possibilities as $\left|1, \{0^2, 1^{N-2}\}\right\rangle$ and record the number of possibilities as $\binom{N-1}{2}$. If we assume identical qubits, then all cases when two errors occur happen with probability $\left|\beta\right|^2 p^2 (1-p)^{N-2}$. Now, it can be seen that Table E.1 contains the whole of possibilities for the $N-1$ ancilla qubit state after storage.

If the syndrome measurement (after decoding) is ignored, then the final state can be partitioned according to whether the main qubit will be in state $\left|\psi_0^N\right\rangle$ (no qubits relaxed), $|0\rangle$ ($N-q$ qubits relax), $|1\rangle$ ($q-N$ qubits relax), or $|0\rangle$ (all N qubits relax).

Table E.1: In this table the N-qubit wavefunctions for all possible relaxation errors after repetitive coding are summarized.

number of errors	$\left\vert\psi_s^N\right\rangle$	number of cases	probability
0	$\left\vert\psi_0^N\right\rangle$	1	Δ_N
1	$\left\vert 0,\{1^{N-1}\}\right\rangle$	$\binom{N-1}{N-1}$	$\vert\beta\vert^2 p^1(1-p)^{N-1}$
1	$\left\vert 1,\{0^1,1^{N-2}\}\right\rangle$	$\binom{N-1}{1}$	$\vert\beta\vert^2 p^1(1-p)^{N-1}$
2	$\left\vert 0,\{0^1,1^{N-2}\}\right\rangle$	$\binom{N-1}{N-2}$	$\vert\beta\vert^2 p^2(1-p)^{N-2}$
2	$\left\vert 1,\{0^2,1^{N-3}\}\right\rangle$	$\binom{N-1}{2}$	$\vert\beta\vert^2 p^2(1-p)^{N-2}$
3	$\left\vert 0,\{0^2,1^{N-3}\}\right\rangle$	$\binom{N-1}{N-3}$	$\vert\beta\vert^2 p^3(1-p)^{N-3}$
3	$\left\vert 1,\{0^3,1^{N-4}\}\right\rangle$	$\binom{N-1}{3}$	$\vert\beta\vert^2 p^3(1-p)^{N-3}$
$\vdots$	$\vdots$	$\vdots$	$\vdots$
$N-2$	$\left\vert 0,\{0^{N-3},1^2\}\right\rangle$	$\binom{N-1}{2}$	$\vert\beta\vert^2 p^{N-2}(1-p)^2$
$N-2$	$\left\vert 1,\{0^{N-2},1^1\}\right\rangle$	$\binom{N-1}{N-2}$	$\vert\beta\vert^2 p^{N-2}(1-p)^2$
$N-1$	$\left\vert 0,\{0^{N-2},1^1\}\right\rangle$	$\binom{N-1}{1}$	$\vert\beta\vert^2 p^{N-1}(1-p)^1$
$N-1$	$\left\vert 1,\{0^{N-1}\}\right\rangle$	$\binom{N-1}{N-1}$	$\vert\beta\vert^2 p^{N-1}(1-p)^1$
N	$\vert 0\rangle^N$	1	$\vert\beta\vert^2 p^N$

After such partitioning the final state is

$$\begin{aligned}\rho_{ign}^N = \Delta_N \left\vert\psi_0^N\right\rangle\left\langle\psi_0^N\right\vert + \sum_{q=1}^{N-1}\binom{N-1}{N-q}\vert\beta\vert^2 p^q(1-p)^{N-q}\vert 0\rangle\langle 0\vert \\ + \sum_{q=1}^{N-1}\binom{N-1}{q}\vert\beta\vert^2 p^q(1-p)^{N-q}\vert 1\rangle\langle 1\vert + \vert\beta\vert^2 p^N\vert 0\rangle\langle 0\vert .\end{aligned} \tag{E.1}$$

Using the following relations

$$\begin{aligned}\sum_{q=1}^{N-1}\binom{N-1}{q}p^q(1-p)^{N-q} = (1-p)-(1-p)^N \\ \sum_{q=1}^{N-1}\binom{N-1}{N-q}p^q(1-p)^{N-q} = p-p^N,\end{aligned} \tag{E.2}$$

the final state can be written without the large sums and averaging becomes simple using the results in Appendix C. The average state fidelity of the main qubit when ancilla measurement results are ignored is thus

$$\overline{F_{st}} = \frac{2}{3}+\frac{1}{3}(1-p)^{\frac{N}{2}}-\frac{1}{6}p. \tag{E.3}$$

The results in Ch. 3 come from similar calculations based on this technique of partitioned combinatorics.